

Chapter 3

**μ -Phenoxo bridged dicopper (II)
complexes of binucleating diimines
derived from 2,6-diacetyl-4-methyl
phenol**

Chapter 3: μ -Phenoxo bridged Cu(II)Cu(II) complexes of compartmental imine ligands derived from 2,6-diacetyl-4-methylphenol

3.1 INTRODUCTION	129
3.2 Experimental Section	131
3.2.1 Reagents and materials	131
3.2.2 Synthesis of binucleating ligands	132
3.2.2.1 Synthesis of 2,6-diacetyl-4-methylphenol (dac)	132
3.2.2.2 Synthesis of 1-(3-(1-((2-(1H-indol-3-yl)ethyl)imino)ethyl)-2-hydroxy-5-methylphenyl)ethan-1-one (L⁸)	132
3.2.3 Synthesis of binuclear copper(II) complexes	133
3.2.3.1 Synthesis of [Cu ₂ (L ₄)(OH)(NO ₃) ₂]2NO ₃ ·2H ₂ O (C4)	133
3.2.3.2 Synthesis of [Cu ₂ (L ₅)(OH)(ClO ₄)]ClO ₄ (C5)	134
3.2.3.3 Synthesis of [Cu ₂ (L ₆)(OH)(ClO ₄)]ClO ₄ (C6)	134
3.2.3.4 Synthesis of [Cu ₂ (L ₇)(OH)(OAc)]OAc (C7)	134
3.2.3.5 Synthesis of [Cu ₂ (L ₈)(ClO ₄) ₂] (C8)	134
3.2.4 SOD mimic activity	135
3.2.5 Ascorbic Acid Oxidase (AAO) activity	135
3.2.6 Catecholase activity	136
3.2.7 Physical Measurements	136
3.2.7.1 Infrared studies	136
3.2.7.2 NMR studies	136
3.2.7.3 Mass studies	136
3.2.7.4 Electronic studies	137
3.2.7.5 Photoluminescence studies	137
3.2.7.6 Elemental Analysis	137
3.2.7.7 ESR studies	137

3.2.7.8 Single Crystal X-ray Diffraction	137
3.2.7.9 Molecular Modelling studies	138
3.3 Results and Discussion	138
3.3.1 Characterization of dac and L ⁸	138
3.3.2 Characterization of complexes	139
3.3.2.1 Elemental analysis	139
3.3.2.2 IR spectra	139
3.3.2.3 Mass spectra	140
3.3.2.4 Electronic spectra	141
3.3.2.5 Photoluminescence spectra	143
3.3.2.6 Crystal structure of complex C4 and C6	143
3.3.2.7 ESR spectra	146
3.3.2.8 Molecular Modelling	148
3.3.3 SOD mimic activity	155
3.3.4 Ascorbic Acid Oxidase (AAO) activity	157
3.3.5 Catecholase activity	162
3.4 CONCLUSION	168
Supplementary Information	169
References	198

3.1 INTRODUCTION

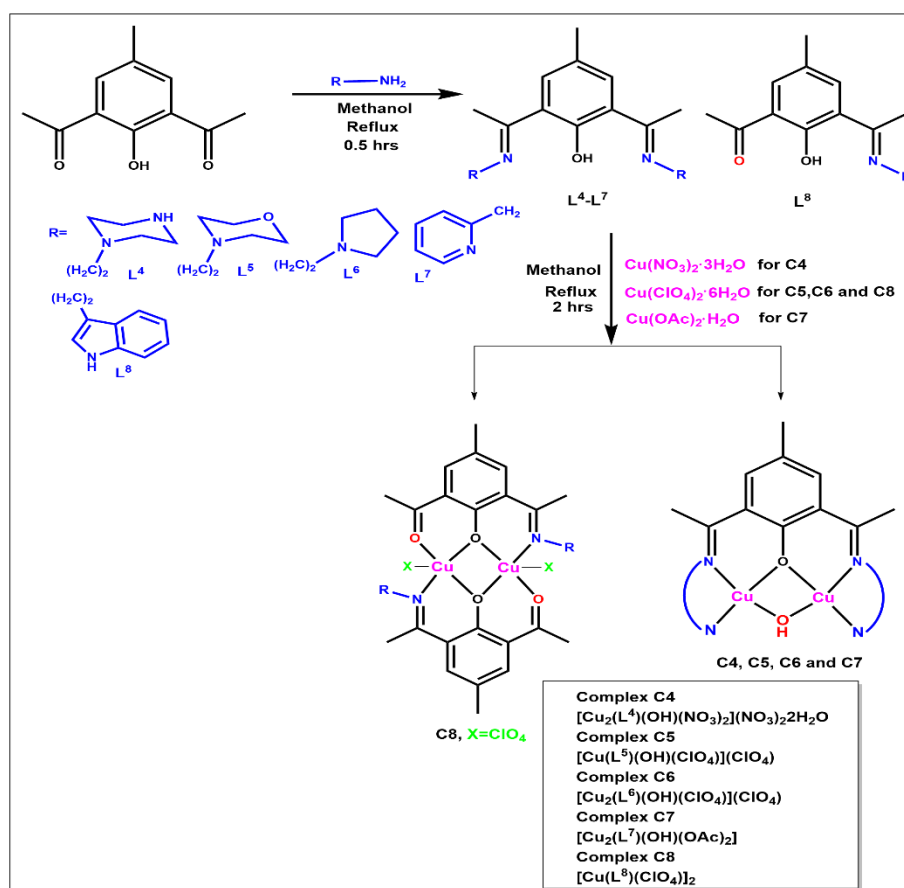
The study of exchange coupled dicopper complexes have been in focus due to their relevance with type 3 active site in copper proteins such as catechol oxidase, tyrosinase etc.¹ The detailed study of their magnetic properties have indicated that the spin exchange between the paramagnetic copper(II) centers is influenced by the nature of the ligand backbone, metal ions and auxiliary part of the ligands i.e. the atoms or groups of atoms which are not directly attached to the co-ordination sphere of the metal ion in the ligand backbone.² The denticity of ligands, steric and electronic factors affect the chemistry of particular metal ions.³⁻⁷

Catechol oxidase (CO), containing antiferromagnetically coupled dinuclear copper(II) centres separated at distance of 2.9Å and linked by hydroxide bridge in the met form,⁴ serves as oxygenase or dioxygen activation protein.^{8,9} Therefore, dinuclear copper complexes, mimicking type 3 copper proteins with all salient features, are considered of interest to elucidate the functional mechanism of the native enzyme and to develop bio-mimetic catalytic systems. They selectively catalyze oxidation of catechols to their corresponding o-benzoquinones.^{1,10-17} The bio-mimicking catechol oxidase dicopper(II) complexes, the most explored till date, include those of Schiff bases ligands.¹⁸⁻²⁴ The activity of the complexes depends on both internal factors such as Cu---Cu bond distance, flexibility of ligands, electronic factor and coordination environment around the metal ions as well as external factors such as solvent, pH of the medium and nature of the substrate. The extensive studies on the synthetic mimics of active site of catechol oxidase in recent years reveal the fact that these mimic systems must possess some structural features similar to the native enzyme, including the presence of hydroxides bridge and two proximal copper(II) ions held at an optimum distance of ~3Å as can be obtained by using End-off compartmental ligands.²⁴⁻⁴⁰ Kitajima *et al*⁴¹⁻⁴⁴ demonstrated that the antiferromagnetic coupling between copper centers was a common feature that was maintained extensively in the synthetic models for dioxygen binding proteins.

Several reports for the synthesis of similar synthetic mimics for SOD mimic activity have appeared in the literature.⁴⁵⁻⁶⁹ Devereux *et al*⁷⁰⁻⁷² assayed the SOD like activity using modified NBT assay with xanthine-xanthine oxidase system as source of superoxide. Potapov *et al*⁷³ assayed the SOD mimic like activity using NADH-PMS-

NBT assay of bipyridyl containing mixed ligand complexes. They all have demonstrated high SOD-like activity and hence considered as promising class of SOD mimetics with therapeutic potential.

It was thought of interest to vary the auxiliary part of the ligands in a systematic manner and examine its effect on the activity of the dicopper complexes. With this intention, dicopper(II) complexes, $[\text{Cu}_2(\text{L}^4)(\text{OH})(\text{NO}_3)_2](\text{NO}_3)_2 \cdot 2\text{H}_2\text{O}$, $[\text{Cu}_2\text{L}^5(\text{OH})(\text{ClO}_4)]\text{ClO}_4$, $[\text{Cu}_2\text{L}^6(\text{OH})(\text{ClO}_4)]\text{ClO}_4$, $[\text{Cu}_2\text{L}^7(\text{OH})(\text{OAc})]\text{OAc}$ and $[\text{Cu}_2(\text{L}^8)_2](\text{ClO}_4)_2$ of compartmental Schiff base ligands, $\text{L}^4\text{-L}^7$, formed by condensation between 2,6-diacetyl-4-methylphenol and nitrogen rich amines viz. N-aminoethyl piperazine, N-aminoethyl morpholine, N-aminoethyl pyrrolidine, 2-picoyl amine and tryptamine have been synthesized as depicted in **Scheme 3.1.1**.



Scheme 3.1.1 Diagrammatic representation of synthesis of ligands and its copper(II) complexes

The architecture of these newly synthesized complexes was largely influenced by the R group present in the ligand backbone which is actually the “auxillary part” of the ligand. Piperazine, morpholine and pyrrolidine are related cyclic aliphatic

moieties with a variation in the presence of distal N, O or C atoms affecting the overall electron density. Similarly, picolyl amine and tryptamine provide pyridyl and indole as aromatic auxiliary groups. The complexes have an endogenous phenoxo- and another exogenous bridging group.

Catecholase activity of all the complexes was studied using 3,5-di-tert-butyl catechol (3,5-DTBC), 4-methyl catechol, dopamine, pyrocatechol and 2,3-dihydroxynaphthalene as model substrate. Ascorbate oxidase activity of all complexes was studied using ascorbic acid as substrate in acetate buffer (pH 5.5). Superoxide dismutase activity of all complexes were studied by NBT-NADH-PMS assay using phosphate buffer (pH 7.8). Solution phase magnetic behaviour of the complexes has been investigated by ESR studies. All these observations have been mentioned herein. (**Figure 3.1.1**)

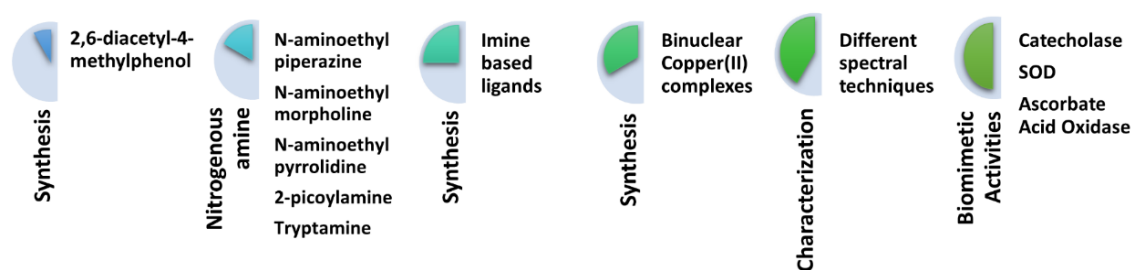


Figure 3.1.1 Diagrammatic representation of synthesis and activities of binuclear complexes

3.2 Experimental Section

3.2.1 Reagents and materials

p-Cresol, acetyl chloride, nitrobenzene, sodium acetate and copper nitrate trihydrate were procured from Merck. Anhydrous AlCl_3 , methanol and dimethyl sulfoxide were procured from Spectrochem. N-aminoethyl piperazine was procured from Alfa Aesar. N-aminoethyl morpholine and N-aminoethyl pyrrolidine were procured from TCI chemicals. Tryptamine, 2-picoyl amine, copper perchlorate hexahydrate, 3,5-DTBC, 4-methyl catechol, Dopamine, pyrocatechol, 2,3-dihydroxy naphthalene were purchased from Sigma Aldrich. Potassium iodide and ammonium molybdate were purchased from Loba Chem. β -NADH, phenazine methosulphate (PMS), nitroblue tetrazolium (NBT), acetic acid, sodium dihydrogen phosphate monohydrate and dibasic sodium phosphate (anhydrous) were purchased from SRL

chemicals. All other chemicals used were of AR grade and were used as received. For spectroscopic studies, spectroscopic grade solvents were used. The solvents were distilled prior to use and dried according to standard procedure wherever necessary.

3.2.2 Synthesis of binucleating ligands

3.2.2.1 Synthesis of 2,6-diacetyl-4-methylphenol (dac)

2,6-Diacetyl-4-methylphenol (dac) was synthesized starting from p-cresol and following a literature procedure⁷⁴: In a 500 ml two-necked flask fitted with a reflux condenser and a pressure equalizing addition funnel, anhyd. AlCl_3 (200 g, 1.5 mol) was dissolved in dry nitrobenzene (300 ml) by stirring. To the resulting solution was added freshly distilled p-cresol (27 g, 0.25 mol). The reaction vessel was then placed in an ice-water bath to adjust the temperature to ca. 15 °C and acetyl chloride (60 g, 0.75 mol) was added dropwise over a period of 1.5 h. After the addition of acetyl chloride, the bath temperature was slowly raised to 60 °C, over 3h, and the reaction was continued at 60 °C for a further 3 h period. The reaction container was then cooled by surrounding it with crushed ice and ice-cooled HCl (400 ml, 6 mol dm^{-3}) was slowly added (CAUTION: brisk evolution of HCl gas occurred at this stage). When about 100 ml of the acid was added the reaction mixture became highly viscous due to the separation of an aluminum complex. The speed of the stirrer was increased, and with the addition of more acid a thin slurry resulted. After the complete addition of the acid solution the contents of the flask were transferred to a separating funnel and allowed to stand overnight. The organic layer thus separated was collected and steam distilled to remove nitrobenzene and some 2-hydroxy-5-methylacetophenone which formed. The brown solid which remained was extracted with chloroform and dried over Na_2SO_4 . The chloroform solution, after treatment with activated charcoal, was allowed to crystallize at ambient temperature by slow evaporation. The needle-shaped crystals which separated were collected by filtration and recrystallized from light petroleum (b.p. 60-80 °C). Yield= 20 g; m.p. 82 °C.

3.2.2.2 Synthesis of 1-(3-(1-((2-(1H-indol-3-yl)ethyl)imino)ethyl)-2-hydroxy-5-methylphenyl)ethan-1-one (L^8)

4-Methyl-2,6-diacetylphenol (0.192 g, 1 mmol) was dissolved in methanol (10 ml) and tryptamine (0.320g, 2 mmol) dissolved in methanol (5 ml) was added to it. The mixture was allowed to reflux for 1 h. The reaction was monitored by TLC. At the

end of 1 h, a single spot for the product appeared on TLC. The reaction mixture was concentrated to about 10 ml and cooled to obtain yellow colour microcrystalline solid. The product was filtered and washed with cold methanol to remove the traces of any soluble impurities. No purification method was employed as single spot was obtained on TLC plate. Yield: 0.180g (53.89%). Solubility: Chloroform, DMSO, DMF. M.P.: 156-158°C.

3.2.3 Synthesis of binuclear copper(II) complexes

Caution: In general, perchlorate salts of metal complexes in organic liquids are potentially explosive. While none of the present perchlorate complexes has been proved to be shock sensitive, care is recommended while working with perchlorate salts.

The following general template synthetic route was adopted for preparing the complex. A methanolic solution of copper(II) nitrate trihydrate or copper(II) perchlorate hexahydrate or copper(II) acetate monohydrate was added to the ligand solution formed *in situ* via condensation between 4-methyl-2,6-diacetyl phenol and various amines such as N-aminoethyl piperazine, N-aminoethyl morpholine, N-aminoethyl pyrrolidine, 2-picoyl amine and tryptamine maintaining the appropriate molar ratio. The preparation, composition, and other physicochemical characteristics of the complex are given below.

3.2.3.1 Synthesis of $[Cu_2(L_4)(OH)(NO_3)_2]2NO_3 \cdot 2H_2O$ (C4)

A methanolic solution (5ml) of N-aminoethyl piperazine (0.258g, 2mmol) was added dropwise to a hot methanolic solution (10ml) of 2,6-diacetyl-4-methyl phenol (0.192g, 1mmol) and the resulting mixture was allowed to reflux for half an hour. A methanolic solution (15ml) of $Cu(NO_3)_2 \cdot 3H_2O$ (0.604g, 2.5mmol) was added to ligand solution and the resulting solution was allowed to reflux for 2 hrs. A green coloured microcrystalline solid precipitated after 1 hrs of stirring. The product was collected by filtration. It was washed several times with cold methanol to remove the traces of amines and dac precursor. Suitable crystal for X-ray diffraction was obtained by recrystallization from methanolic solution of complex after 10-12 days. Yield: 0.270g (30.04 %). Solubility: Methanol, DMSO, DMF.

3.2.3.2 Synthesis of $[Cu_2(L_5)(OH)(ClO_4)]ClO_4$ (C5)

Complex **C5** was prepared by adopting the same procedure as used for **C4** by using dac (0.162g, 0.84mmol) and N-aminoethyl morpholine (0.2192g, 1.68mmol) instead of N-aminoethyl piperazine. After half an hour, a methanolic solution (15ml) of $Cu(ClO_4)_2 \cdot 6H_2O$ (0.780g, 2.1mmol) was added to ligand solution and the resulting solution was stirred for 3 hrs. A dark olive-green coloured microcrystalline solid precipitated after 1 hrs of stirring. The product was collected by filtration. It was washed several times with cold methanol to remove any traces of amines and dac precursor remaining unreacted. Yield: 0.277g (36.54 %). Solubility: Methanol, DMSO, DMF.

3.2.3.3 Synthesis of $[Cu_2(L_6)(OH)(ClO_4)]ClO_4$ (C6)

Complex **C6** was prepared by adopting the same procedure as used for **C4** by using dac (0.192g, 1mmol) and N-aminoethyl pyrrolidine (0.228g, 2mmol) instead of N-aminoethyl piperazine. After half an hour, a methanolic solution (15ml) of $Cu(ClO_4)_2 \cdot 6H_2O$ (0.926g, 2.5mmol) was added to ligand solution and the resulting solution was allowed to stir for 3 hrs. The resultant green coloured solution was filtered and kept for crystallization. Dark green coloured crystals suitable for X-ray diffraction were obtained after a week. Yield: 0.2550g (35.12%). Solubility: Methanol, DMSO, DMF.

3.2.3.4 Synthesis of $[Cu_2(L_7)(OH)(OAc)]OAc$ (C7)

Complex **C7** was prepared by adopting the same procedure as used for **C4** by using dac and 2-picoyl amine (0.21628g, 2mmol) instead of N-aminoethyl piperazine. After half an hour, a methanolic solution (15ml) of $Cu(OAc)_2 \cdot H_2O$ (0.499g, 2.5mmol) was added to ligand solution and the resulting solution was allowed to reflux for 3 hrs. A dark green coloured microcrystalline solid precipitated after 1 hrs of stirring. The product was collected by filtration. It was washed several times with cold methanol to remove the traces of any impurities or unreacted materials. Yield: 0.2994g (47.30 %). Solubility: DMSO, DMF.

3.2.3.5 Synthesis of $[Cu_2(L_8)(ClO_4)_2]$ (C8)

A methanolic solution (5ml) of tryptamine (0.3204g, 2mmol) was added dropwise to a hot methanolic solution (10ml) of 2,6-diacetyl-4-methyl phenol (0.192g, 1mmol) and the resulting mixture was refluxed for one hour. Yellow coloured

microcrystalline solid precipitated out. A methanolic solution (15ml) of $\text{Cu}(\text{ClO}_4)_2 \cdot 6\text{H}_2\text{O}$ (0.741g, 2mmol) was added to the ligand solution and the resulting solution was allowed to reflux for 3 hrs. Addition of triethylamine (0.202, 2mmol) led to color change from green to olive green. A green coloured microcrystalline solid precipitated out after 1 hrs of stirring. The product was collected by filtration. It was washed several times with cold methanol to remove the traces of amines and dac precursor. Yield: 0.580g (58.53 %). Solubility: Chloroform, Dichloromethane, DMSO, DMF.

3.2.4 SOD mimic activity

The superoxide dismutase (SOD) activity was measured by using non-enzymatic method (NADH-PMS-NBT assay) (**Scheme 2.2.4.1**)^{62,68,69,73} as explained in **section 2.2.4** of chapter 2.

3.2.5 Ascorbic Acid Oxidase (AAO) activity

Ascorbic Acid Oxidase (AAO) activity of all synthesized complexes has been evaluated by kinetic studies with ascorbic acid as substrate wherein three different parameters such as substrate concentration, catalyst concentration and temperature have been varied. The ascorbate oxidase activity of all five complexes was studied by treating 1×10^{-6} M complex solution with 1×10^{-4} M ascorbic acid solution under aerobic conditions at 30°C. For variation in the substrate concentration, solutions of ascorbic acid of concentration ranging from 0.2-1.8 $\times 10^{-4}$ M were prepared from a 5×10^{-2} M stock solution. The dependence of the initial rate on the concentration of the ascorbic acid was monitored by UV-Vis spectroscopy by maintaining the catalyst concentration (0.002mM for C4 and C6, 0.004mM for C7 & 0.001mM for C5 and C8) for each set. The catalyst concentration was varied for different complexes by maintaining constant substrate concentration 1×10^{-4} M. The time dependent wavelength scan was recorded in acetate buffer medium (pH 5.5) to understand the potential of all complexes as catalyst towards the oxidation of ascorbic acid. The initial rate method was used for determining the rates. The reaction rates, activation energy and order of reaction were calculated as explained in **section 2.2.5** of chapter 2.

3.2.6 Catecholase activity

Catecholase activity of all synthesized complexes has been evaluated by kinetic studies wherein three different parameters such as substrate concentration, catalyst concentration and temperature have been varied. The catecholase activity of all five complexes was studied by treating 1×10^{-4} M complex solution with 1×10^{-2} M of 3,5-di-*tert*-butylcatechol (3,5-DTBC) and 1×10^{-2} M of 4-methyl catechol solution under aerobic conditions at 30°C. The time dependent wavelength scan was recorded in methanol to understand the potential of all complexes as catalyst towards the oxidation of catechol derivatives.

The initial rate method was used to calculate the kinetic parameters. Substrate solutions of concentrations ranging from 0.1×10^{-2} M to 1×10^{-2} M were prepared from a 5×10^{-2} M solution. The dependence of the initial rate on the concentration of the ascorbic was monitored by UV-Vis spectroscopy by maintaining the catalyst concentration (1×10^{-4} M) for each set. The catalyst concentration ranging from 20×10^{-6} to 100×10^{-6} M was varied for different complexes by maintaining constant substrate concentration 1×10^{-2} M. The reaction rates, activation energy and order of reaction were calculated as explained in **section 2.2.6** of chapter 2.

3.2.7 Physical Measurements

3.2.7.1 Infrared studies

Infrared Spectra ($4000 - 400 \text{ cm}^{-1}$) were recorded in the form of KBr pellets at 27°C using Bruker Alpha Transmission FT-IR spectrometer. The solid sample was ground together with anhydrous KBr using mortar pestle and the pellet so formed was subjected to FT-IR analysis.

3.2.7.2 NMR studies

The ^1H spectra of synthesized ligand were recorded on Bruker Avance (400 MHz) NMR spectrometer in CDCl_3 .

3.2.7.3 Mass studies

ESI-Mass of all complexes were recorded using XEVO G2-XS QTOF mass spectrometer from IIT Ropar.

3.2.7.4 Electronic studies

Electronic spectra (200–900 nm) were recorded in methanolic and aqueous solutions using PerkinElmer UV-Vis spectrophotometer Model Lambda 35.

3.2.4.5 Photoluminescence studies

The emission spectra of all synthesized ligands and complexes were recorded on FP-6300 spectrofluorophotometer.

3.2.7.6 Elemental Analysis

Elemental analysis of synthesized complexes was recorded using EuroVector EA 300 from SAIF CDRI Lucknow.

3.2.7.7 ESR studies

ESR spectra of all complexes were recorded using ESR JEOL model: JES - FA200 ESR Spectrometer in solid at RT and solution phase at LNT using X- band frequency with 9.45 GHz.

3.2.7.8 Single Crystal X-ray Diffraction

Single crystal diffraction data for complex **C4** was collected on an Xcalibur, EOS, Gemini four circle diffractometer with CCD plate detector using graphite monochromatic Cu K α radiation (1.54184 Å). Absorption correction of multiscan type was applied and the data was processed using CrysAlisPro, Agilent Technologies, Version 1.171.37.33. Empirical absorption corrections were applied to the complex using spherical harmonics, implemented in SCALE3 ABSPACK scaling algorithm. The crystal was kept at 293(2) K during data collection. The cell refinement, data collection and reduction were computed by CrysAlisPro, Agilent Technologies, Version 1.171.37.33.

Single crystal diffraction data for complex **C6** was collected on Bruker APEX-II CCD diffractometer (CIF IISER Bhopal).

Using Olex2⁷⁵, the structure was solved by Direct Methods with SHELXS^{76,77} structure solution program and refined by full matrix least squares method based on F2 with all observed reflections with the SHELXL^{76,77} refinement package. Graphics were generated using MERCURY (version 4.3.1). All non-hydrogen atoms were refined with anisotropic thermal parameters. The hydrogen atoms attached to carbon were constrained to 'ride' on the atom attached to it. In all the cases, non-hydrogen

atoms were treated anisotropically. Whenever possible, the hydrogen atoms were refined by locating on a difference Fourier map. In other cases, hydrogen atoms were geometrically fixed.

3.2.7.9 Molecular Modelling studies

The complexes have been theoretically modelled by using GAUSSIAN 16 software program⁷⁸. Molecular geometries of the ground state of the complexes were optimized by using B3LYP method⁷⁹ with 6-31G and LANL2DZ basis set^{80,81}. Frontier molecular orbitals HOMO (highest occupied molecular orbital) and LUMO (lowest unoccupied molecular orbital) in the optimized structures of the molecule are visualized in Gauss View Gauss View 6⁸² and their energy has been calculated.

3.3 Results and Discussion

3.3.1 Characterization of *dac* and **L⁸**

2,6-Diacetyl-4-methylphenol (dac): The chemical shift values, splitting and integration of signals observed in the ¹H NMR of the molecule are consistent with its structure. They are as follows: (δ ppm in CDCl₃): 2.351 (s, 3H, -CH₃), 2.697 (s, 6H, -COCH₃), 7.804 (s, 2H, aromatic H), 13.153 (s, 1H, -OH) (see SI†: **Fig. S3.1**).

The ligands (**L⁴-L⁷**) were synthesized and used *in situ* for the synthesis of the complexes, they were not isolated. Only **L⁸** was isolated and spectroscopically characterized.

Characterization of L₈:

In the ¹H NMR spectrum of **L⁸**, all observed chemical shift values, their splitting and integration is in agreement with the structure of the molecule intended to be synthesized as shown in **Scheme 3.1.1**. These values are as follows: (δ ppm in CDCl₃): 8.155 (s, 1H, NH of indole ring), 7.721 (d, 1H, indole ring), 7.660 (s, 1H, aromatic ring near C=O), 7.395 (s, 1H, aromatic ring near C=N), 7.45(d, 1H, indole ring), 7.120 (d, 1H, indole ring), 7.256 (dt, 1H, indole ring), 7.160 (dt, 1H, indole ring), 3.933 (t, 2H, methylene protons attached to C=N), 3.282 (m, 2H, methylene protons attached to indole ring), 2.761 (s, 3H, CH₃-C=O), 2.278 (s, 3H, CH₃-C=N), 2.213 (s, 3H, CH₃) (see SI†: **Fig. S3.2**).

The IR spectrum of ligand **L⁸** consist of all important bands as expected for the molecule. The νC=N stretching frequency of ligand **L⁸** appears at 1644 cm⁻¹. The N-H stretching frequency of indole in the free ligand appears at 3315.78 cm⁻¹. A band

appears at around 1726.58 cm^{-1} corresponding to -C=O of acetyl group which confirms that imine condensation (1:1) has occurred at one acetyl position and other acetyl group was free. The medium/strong band due to =C-H bending vibrations of indole ring have been observed at approx. 682 cm^{-1} for the ligand L_8 (see SI† **Fig. S3.3**).

In the mass spectrum of ligand L_8 , a peak is observed at $m/z = 345$, corresponding to $[\text{M}+\text{H}]^+$ where M = molecular weight of $\text{L}_8 = 334$. (See SI† **Fig. 3.4**)

The electronic absorption spectrum of ligand L_8 , Both $\pi\text{-}\pi^*$ and $\text{n-}\pi^*$ transitions are observed around 233nm, 264nm and 367nm, 423nm, respectively (**Figure 3.3.2.4.1**). The ligand is fluorescent. When a solution of ligand L_8 was excited at 425nm, an emission band was observed in the emission spectra at $\lambda_{\text{max}} = 512\text{nm}$ (**Figure 3.3.2.5.1**).

3.3.2 Characterization of complexes

3.3.2.1 Elemental analysis

The complexes, **C4-C8**, were characterized by elemental analysis as recorded in **table 3.3.2.1.1** (Values in parenthesis are calculated values)

Table 3.3.2.1.1 Elemental analysis of complexes(**C4-C8**)

Complex	Empirical Formula (M.W.)	%C	%H	%N
C4	$\text{Cu}_2\text{C}_{23}\text{H}_{40}\text{O}_{14}\text{N}_{10}\cdot 2\text{H}_2\text{O}$ (M.W.= 843)	32.279 (32.74)	5.201 (5.22)	16.878 (16.61)
C5	$\text{Cu}_2\text{C}_{23}\text{H}_{36}\text{O}_{12}\text{N}_4\text{Cl}_2$ (M.W.=758)	36.354 (36.412)	4.924 (4.749)	7.538 (7.388)
C6	$\text{Cu}_2\text{C}_{23}\text{H}_{36}\text{O}_{10}\text{N}_4\text{Cl}_2$ (M.W.=726)	38.403 (38.016)	4.880 (4.958)	7.526 (7.713)
C7	$\text{Cu}_2\text{C}_{27}\text{H}_{30}\text{O}_6\text{N}_4$ (M.W.=633)	51.185 (51.185)	4.540 (4.739)	8.626 (8.847)
C8	$\text{Cu}_2\text{C}_{42}\text{H}_{42}\text{O}_{12}\text{N}_4\text{Cl}_2$ (M.W.=991)	50.593 (50.857)	4.380 (4.238)	5.426 (5.650)

* Values in parenthesis are calculated from the empirical formula given in column 2 of the table.

3.3.2.2 IR spectra

In the IR spectra of the complexes **C4-C8**, $\nu\text{C=N}$ appears at $\sim 1610\text{-}1665\text{ cm}^{-1}$ (see SI†: **Fig S3.5-3.9**) (**Table 3.3.2.2.1**). The $\nu\text{C=N}$ stretching in **complex C8** has shifted to a lower frequency as compared to that in the free **ligand L⁸** clearly indicating the participation of imine N in coordination with copper ion. The N-H stretching frequency of indole in the free ligand appears at 3315.78 cm^{-1} while that

in the **complex C8** appears at 3374.32 cm^{-1} . A band appears at $\sim 1726.58\text{ cm}^{-1}$ corresponding to -C=O of acetyl group in free **ligand L⁸** while that in **complex C8** appears at 1727.21 cm^{-1} . The peak at $3400\text{-}3530\text{ cm}^{-1}$ corresponds to the $\nu\text{O-H}$ of coordinated or uncoordinated water in complexes (**C4-C6**). In the IR spectrum of **complex C4**, two strong bands at 1384.10 and 1357.24 cm^{-1} due to the asymmetric stretching vibrations in nitrate are observed, indicating that nitrate is coordinated to copper(II) ion. In the IR spectra of complexes **C5**, **C6** and **C8**, two strong bands at $1110\text{-}1060\text{ cm}^{-1}$ due to the symmetric stretching frequency of perchlorate while two strong bands at $1285\text{-}1250\text{ cm}^{-1}$ due to the perchlorate asymmetric stretching vibrations have been observed. This observation suggests monodentate coordination of perchlorate anion to the metal ion.

Table 3.3.2.2.1 IR frequencies of ligand (L⁸) and complexes (C4-C8)

Complex	$\nu\text{ C=N}$ (cm^{-1})	$\nu\text{ C=O}$ (cm^{-1})	$\nu\text{ N-H}$ (cm^{-1})	$\nu\text{ O-H}$ of water (cm^{-1})	$\nu\text{ ClO}_4$ (cm^{-1}) or $\nu\text{ NO}_3$ (cm^{-1})
C4	1612.58	-	-	3444.33	1384.10, 1357.24 ($\nu_{\text{asym}}\text{NO}_3$)
C5	1617.46	-	-	3520.99	1086.89, 1060.63 ($\nu_{\text{sym}}\text{ClO}_4$) 1281.32, 1257.52 ($\nu_{\text{asym}}\text{ClO}_4$)
C6	1620.48	-	-	3506.14	1108.63, 1090.09 ($\nu_{\text{sym}}\text{ClO}_4$) 1280.92, 1258.16 ($\nu_{\text{asym}}\text{ClO}_4$)
C7	1661.22	-	-	-	-
L⁸	1644.69	1726.58	3315.78	-	-
C8	1617.59	1727.21	3374.32	-	1108.09, 1106 ($\nu_{\text{sym}}\text{ClO}_4$) 1270.58, 1255.65 ($\nu_{\text{asym}}\text{ClO}_4$)

3.3.2.3 Mass spectra

The mass spectra of complexes **C4-C8**, are (see **SI† Fig. 3.10-3.14**). In the mass spectrum of **complex C4**, a peak is observed at $m/z = 619.1371$ and 621.1356 corresponding to $[\text{Cu}_2\text{L}^4(\text{OH})(\text{NO}_3)]^+$. The peak observed at $m/z = 415.3238$ corresponds to $[\text{L}^4]^{2+}$. The peak observed at $m/z = 638.1259$ and 701.5038 corresponds to $[\text{Cu}_2\text{L}^4(\text{OH})(\text{NO}_3)(\text{H}_2\text{O})]^+$ and $[\text{Cu}_2\text{L}^4(\text{OH})(\text{NO}_3)_2(\text{H}_2\text{O})+\text{H}^+]^+$, respectively (see **SI† Fig. 3.10**).

In the mass spectrum of **complex C5**, a peak is observed at $m/z = 279.0700$ corresponds to the molecular ion $[\text{Cu}_2\text{L}^5(\text{OH})]^{2+}$. Another peak is observed at $m/z =$

578.1654 corresponding to $[\text{CuL}^5(\text{ClO}_4)+\text{H}^+]^+$ and $[\text{Cu}_2\text{L}^5(\text{OH})_2]^+$. The fragment $[\text{CuL}^5+\text{H}^+]^{2+}$ appears to be the most stable fragment and appears at $m/z=239.6086$ with highest abundance (see **SI† Fig. 3.11**).

In the mass spectrum of **complex C6**, peaks observed at $m/z = 750.4188$ and 752.4186 754.4713 can be assigned to the isotopic masses of $[[\text{Cu}_2\text{L}^6(\text{OH})(\text{ClO}_4)_2]1.5\text{H}_2\text{O}+\text{H}^+]^+$ (M.W.= 751) (A water molecule shared between two molecules). A peak is observed at 273.2004 corresponds to $[\text{Cu}_2\text{L}^6(\text{OH})(\text{H}_2\text{O})]^{2+}$ (M.W.=272). A peak observed at 193.0892 corresponds to $[\text{L}^6+2\text{H}^+]^{+2}$. Some more fragments of the complex observed in the mass spectrum correspond to $[\text{CuL}^6]^+$ (FW = 446) at 446.0857 , $[\text{CuL}^6(\text{ClO}_4)+\text{H}^+]$ (FW = 546) at 546.1749 and $[\text{CuL}^6+\text{H}^+]^{2+}$ (223.5) at $223, 224, 225$ (see **SI† Fig. 3.12**).

In the mass spectrum of **complex C7**, the peaks observed at $m/z= 347.0637$, 346.0615 and 344.0627 correspond to the isotopic masses of two complex ions formed by capturing H^+ ions under electrospray mass ionization conditions, $[\text{Cu}_2\text{L}^7(\text{CH}_3\text{COO})_3(\text{H}_2\text{O})+2\text{H}^+]^{2+}$ (FW = 347) or $[\text{Cu}_2\text{L}^7(\text{CH}_3\text{COO})_2(\text{H}_2\text{O})_4+\text{H}^+]^{2+}$ (FW = 344). Another group of intense peaks observed at $m/z= 422.0729$, 424.0764 and 425.0794 can be assigned to a stable fragment formed by association of CuO with the earlier molecular ion under mass ionization conditions (see **SI† Fig. 3.13**).

In the mass spectrum of **complex C8**, peaks corresponding to the most stable fragments, $[\text{Cu}_2\text{L}^8(\text{H}_2\text{O})]^+$ (477) and $[\text{L}^8+\text{H}^+]^+$ (335) are observed at $m/z= 477.2727$ and 335.1816 , respectively (see **SI† Fig. 3.14**).

3.3.2.4 Electronic spectra

The electronic absorption spectra of all complexes have a charge transfer band appearing at $\lambda_{\text{max}} = 360 - 400$ nm which may be assigned to MLCT transition. All complexes have a weak ligand field band in the range of $600-700$ nm in the visible region which is characteristic of axially distorted geometry around copper centers. The intra-ligand transitions for all complexes appear between $200-300$ nm.

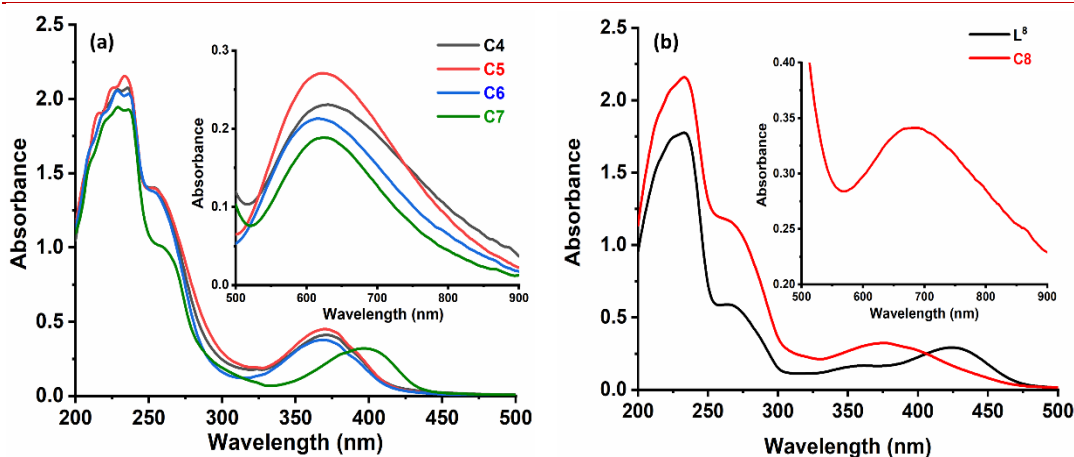


Figure 3.3.2.4.1 Electronic spectra of (a) C4-C7 and (b) L⁸ & C8

The intense higher energy band in the range of 200-300 nm is due to intra ligand π - π^* and in case of ligands in the range of 300-460nm is due to n - π^* transitions (Figure 3.3.2.4.1).

Table 3.3.2.4.1 Electronic spectra of ligand (L⁸) and complexes (C4-C8)

Complexes	λ_{\max}/nm ($\epsilon_{\max}/\text{dm}^3\text{mol}^{-1}\text{cm}^{-1}$)		
	Intra-ligand transitions	Charge transfer	d-d transitions
C4	235(51675), 252(34750)	370(10275)	629 (230)
C5	234(53475), 252(34750)	370(11400)	625(270)
C6	229(51250), 253(34345)	369(9375)	618 (213)
C7	230(48525), 257(25350)	395 (8258)	623 (189)
L ⁸	231(44278), 262(14775), 364(3975), 424(7350)	-	-
C8	233(54000), 262(29625)	375(8025)	684(342)

The transition ${}^2T_{2g} \leftarrow {}^2E_g$ in a d^9 system in octahedral geometry, usually takes place between 600 and 800 nm. On distortion to distorted octahedral or square pyramidal or trigonal bipyramidal or square planar structure, this band undergoes a significant shift and broadening due to splitting of the spectral states and multiple transitions merging to form a broad band.⁸³ Electronic spectra of all synthesized ligands and complexes have been tabulated in tabular form (Table 3.3.2.4.1).

3.3.2.5 Photoluminescence spectra

The complexes **C4-C7** are not fluorescent. However, the ligand **L⁸** and complex **C8**, both emit fluorescent radiation when excited. The emission band was observed at 512nm when a solution of ligand **L⁸** was excited at $\lambda_{\text{max}} = 425\text{nm}$. In a solution of the complex **C8**, the emission band was observed at 510 nm when it was excited at $\lambda_{\text{max}} = 375\text{nm}$ with lower fluorescence intensity (**Figure 3.3.2.5.1**). Thus different excited states are involved in the luminescence phenomenon in **L⁸** and **C8**.

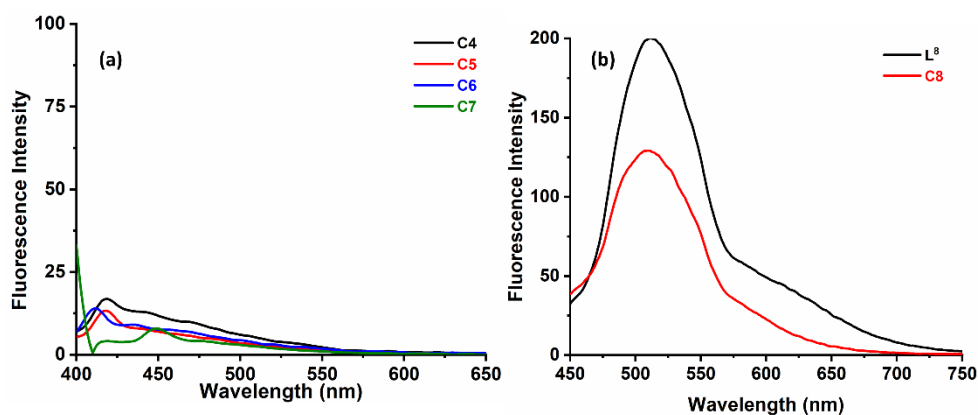


Figure 3.3.2.5.1 Emission spectra of (a) **C4-C7** (b) **L⁸** and **C8**

3.3.2.6 Crystal structure of complex **C4** and **C6**

Green plate like crystals were obtained by slow evaporation of the methanolic solution of **complex C4** for few days. The crystal structure of **complex C4** was determined and is shown in **figure 3.3.2.6.1**. The crystal data and structure refinement parameters of **complex C4** are given in **table 3.3.2.6.1**. Bond distances and bond angles relevant to metal coordination sphere of **complex C4** are given in **Table 3.3.2.6.2**. The stereochemistry around each copper(II) center is best described as distorted octahedral and distorted square pyramidal geometry in **complex C4**. In **complex C6**, each copper atom has a distorted square pyramidal geometry.

The ligands **L⁴** and **L⁶** are coordinated to the metal ions through imine- and amino-nitrogen donors of piperazine and pyrrolidine rings in **C4** and **C6**, respectively. The bridging phenoxido and hydroxide oxygen atoms occupy the equatorial positions along with these coordinated N atoms of the ligands. The Cu-O (phenoxo) distances Cu1-O1 and Cu2-O1 are 1.948(10) and 1.917(9) Å, respectively, in **complex C4** whereas in **complex C6**, the Cu-O (phenoxo) distances Cu1-O1 and Cu2-O1 are

1.944(3) and 1.952(4) Å, respectively, which shows that the bridging by phenolic oxygens is almost symmetrical.

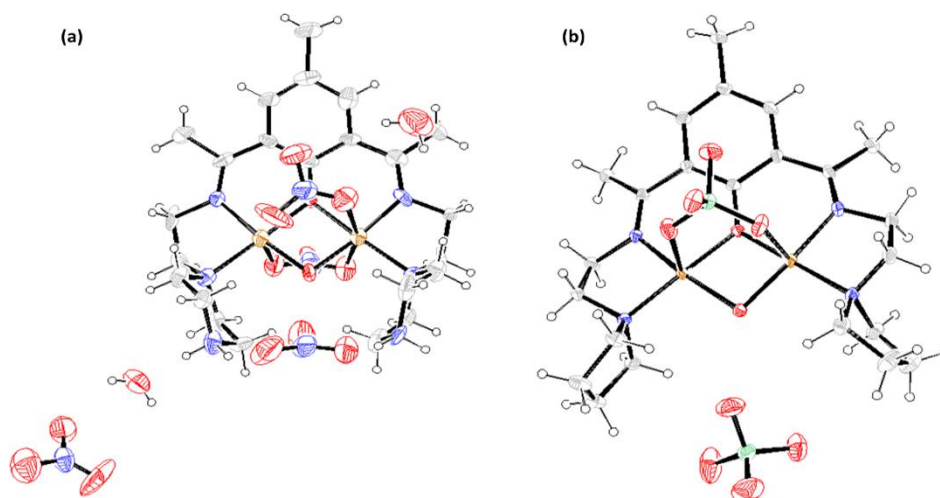


Figure 3.3.2.6.1 ORTEP representation (30% ellipsoid probability) of (a) complex **C4** and (b) complex **C6**

The basal Cu-O distances are comparable in lengths, showing shorter value for the hydroxido oxygen (Cu1-O2=1.902(3) and Cu2-O2=1.906(3)). On the other hand, the Cu-N(imino) bond distance is significantly shorter than that involving the amino nitrogen of the heterocyclic ring indicating the involvement of imine N in π -bonding with the metal ion. (**Table 3.3.2.6.2**). The apical coordination positions in **C4** are occupied by oxygen of nitrate O3 at Cu1 and oxygen of nitrate O4 & O5 at Cu2. One nitrate is bridged between the two copper ions whereas one nitrate is coordinated to one copper ion in monodentate fashion. In complex **C6**, the apical position is occupied by oxygen of perchlorate on both copper atoms, i.e. one perchlorate is forming a bridge between the two metal ion and one is occupying the lattice position for affecting charge neutrality. The Cu1-O1-Cu-O2 bond angle is 96.49(12) whereas that of Cu1-O2-Cu2 bridged by hydroxide group is slightly larger (99.52(12)) leading to a Cu1...Cu2 non-bonding distance between the two metal ions of 2.906(3) Å in **C4**. Piperazine moieties attain a more stable chair conformation and the uncoordinated amine nitrogen are protonated to attain electrical charge neutrality of the system.

Table 3.3.2.6.1 Crystal data and structure refinement for complex **C4** and **C6**

Identification code	C4	C6
Empirical formula	C ₂₃ H ₄₇ Cu ₂ N ₁₀ O ₁₆	Cu ₂ C ₂₃ H ₃₆ N ₄ O ₁₀ Cl ₂
Formula weight	846.78	726.54
Temperature/K	293(2)	293(2)
Crystal system	triclinic	triclinic
Space group	<i>P</i> -1	<i>P</i> -1
a/Å	9.049(3)	8.823(14)
b/Å	9.346(3)	10.664(14)
c/Å	20.281(5)	15.34(2)
α/°	88.41(2)	87.23(4)
β/°	83.32(2)	76.11(6)
γ/°	81.41(2)	88.09(5)
Volume/Å ³	1684.3(8)	1399(4)
Z	1	28
ρ _{calc} /cm ³	0.835	24.150
μ/mm ⁻¹	0.675	24.834
F(000)	441.0	10472.0
Crystal size/mm ³	0.3 × 0.2 × 0.02	0.3 × 0.2 × 0.02
Radiation	MoK _α (λ = 0.71073)	MoK _α (λ = 0.71073)
2θ range for data collection/°	6.014 to 57.948	3.824 to 56.172
Index ranges	-12 ≤ h ≤ 12, -12 ≤ k ≤ 12, -25 ≤ l ≤ 27	-11 ≤ h ≤ 11, -14 ≤ k ≤ 14, -20 ≤ l ≤ 20
Reflections collected	36295	82953
Independent reflections	8122 [R _{int} = 0.7479, R _{sigma} = 0.9815]	6754 [R _{int} = 0.1309, R _{sigma} = 0.0539]
Data/restraints/parameters	8122/0/469	6754/0/373
Goodness-of-fit on F ²	0.842	1.097
Final R indexes [I ≥ 2σ (I)]	R ₁ = 0.1304, wR ₂ = 0.2361	R ₁ = 0.0435, wR ₂ = 0.1045
Final R indexes [all data]	R ₁ = 0.4900, wR ₂ = 0.4001	R ₁ = 0.0644, wR ₂ = 0.1278
Largest diff. peak/hole / e Å ⁻³	0.58/-0.66	0.85/-0.68

The values in the table clearly show that the copper nuclei are coordinated by two nitrogen containing groups. Cu1 and Cu2 are coordinated by one imine nitrogen (N1 for Cu1 and N3 for Cu2) and one piperazine nitrogen (**C4**) / pyrrolidine nitrogen (**C6**) (N2 for Cu1 and N4 for Cu2). It should be noted that all the Cu–N distances fall in the range 1.916–2.055 Å. The N1-Cu1-N3 angle and N2-Cu2-N5 are 85.3(5) (for **C4**) & 85.1(6) (for **C6**) and 87.18(13) (for **C4**) & 86.95(14) (for **C6**). The Cu–O distances for coordinated anions, nitrate and perchlorate in **C4** and **C6**, respectively, are all longer than 2.4 Å. This is indicative of the fact that these anions are very weakly coordinated and can be readily replaced by a substrate during the catalytic reactions.

Table 3.3.2.6.2 Bond Lengths and Angles related to metal coordination in complex **C4** and**C6**

Atom	C4	C6
Cu1-Cu2	2.868(3)	2.906(3)
Cu1-O1	1.947(10)	1.944(3)
Cu1-N1	1.947(12)	1.916(4)
Cu1-N2	2.057(14)	1.996(3)
Cu1-O2	1.898(9)	1.902(3)
Cu1-O3	2.456(15)	2.495(4)
Cu2-O1	1.917(9)	1.952(4)
Cu2-N3	1.920(13)	1.931(4)
Cu2-N4	2.035(12)	2.005(4)
Cu2-O2	1.908(11)	1.906(3)
Cu2-O4	2.585(18)	2.432(4)
Cu2-O5	2.679(14)	-
O1-Cu1-N1	91.2(5)	91.01(13)
N1-Cu1-N2	85.3(5)	87.18(13)
N2-Cu1-O2	100.9(5)	101.35(13)
O2-Cu1-O1	82.8(4)	79.42(12)
O1-Cu2-N3	91.3(5)	90.85(13)
N3-Cu2-N4	85.1(6)	86.95(14)
N4-Cu2-O2	100.3(5)	101.82(13)
O2-Cu2-O1	83.3(4)	79.13(11)
O3-Cu1-O1	87.4(5)	89.98(14)
O4-Cu2-O1	85.3(5)	94.95(12)
O5-Cu2-O1	80.9(5)	-
Cu1-O1-Cu2	95.8(5)	96.49(12)
Cu1-O2-Cu2	97.8(5)	99.52(12)

3.3.2.7 ESR spectra

The ESR spectra of all complexes were recorded both in powdered at RT and solution state at liquid nitrogen temperature (LNT) (**Table 3.3.2.7.1**).

Table 3.3.2.7.1 g_{\parallel} , g_{\perp} and A_{\parallel} or A_{\perp} values of all complexes

Complex	g_{\parallel}	g_{\perp}	A_{\parallel} or $A_{\perp} \times 10^{-4} \text{ cm}^{-1}$
C4	$g_z = 2.25$	$g_x = 2.07, g_y = 2.08$	$A_{\parallel} = 189, A_{\perp} = 67.8$
C5	3.39 (RT)	2.18 (RT)	-
C6	2.15	2.03	171
C7	2.23	2.05	187
C8	2.18 (RT)	2.11 (RT)	-

The ESR spectra of all five complexes typically have axial pattern. The parallel and perpendicular components are well resolve. Well resolved hyperfine splitting is observed in the ESR spectra of **C4**, **C6** and **C7** recorded in the form of frozen solutions at 77K. Four discernible lines are observed corresponding to the coupling with copper nucleus with $I=3/2$ in the g_{\parallel} region (**Figure 3.3.2.7.1**). The A_{\parallel} values

are between $170\text{-}190 \times 10^{-4} \text{ cm}^{-1}$ corresponding to normal copper ion with strong equatorial field with N_2O_2 environment.

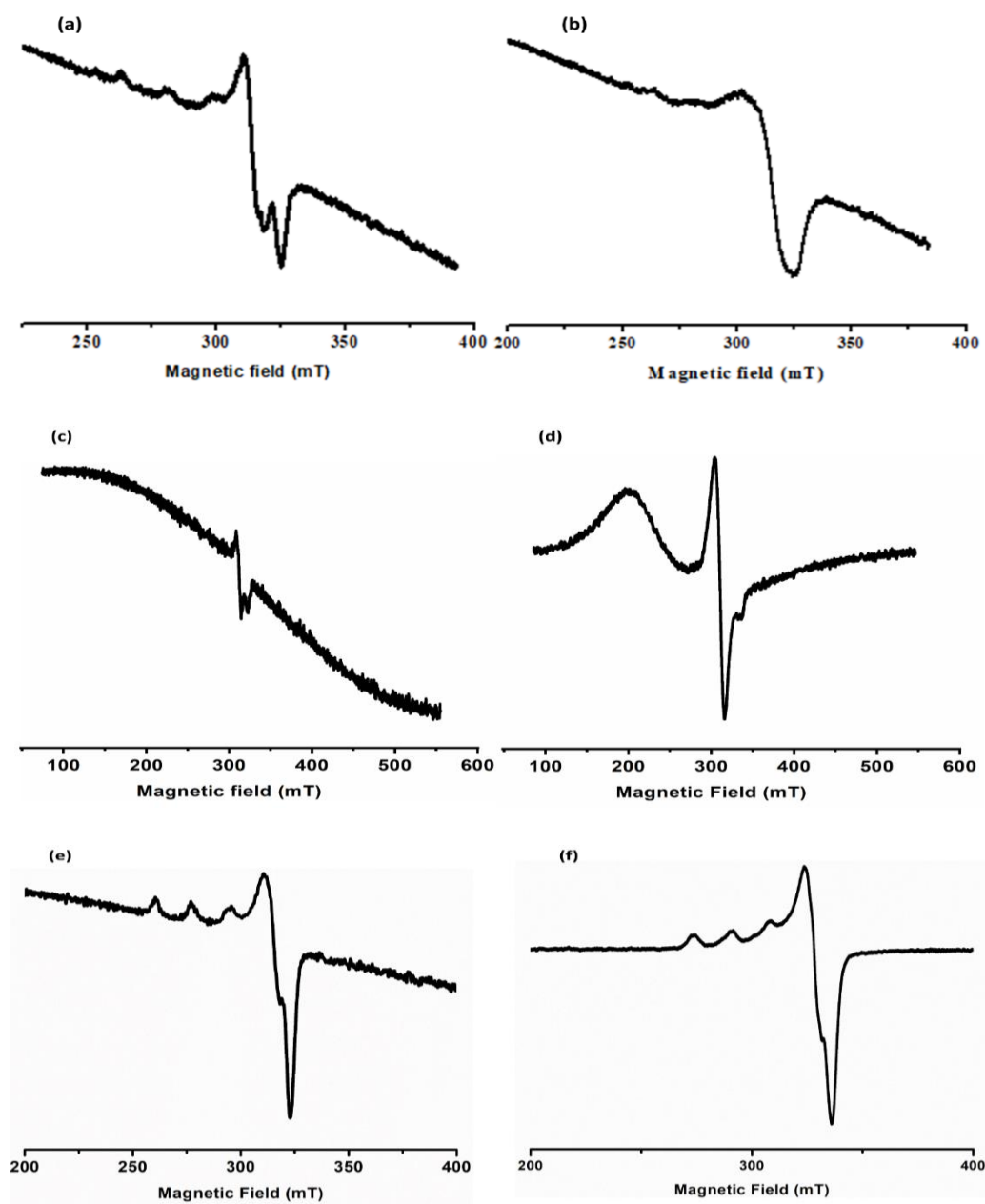


Figure 3.3.2.7.1 ESR spectra of complexes at LNT (a) C4(DMSO) (b) C4 (powder)(RT) (c) C5 (DMSO) (d) C5 (powder)(RT) (e) C6 (DMSO) (f) C6 (powder)(RT) Contd....

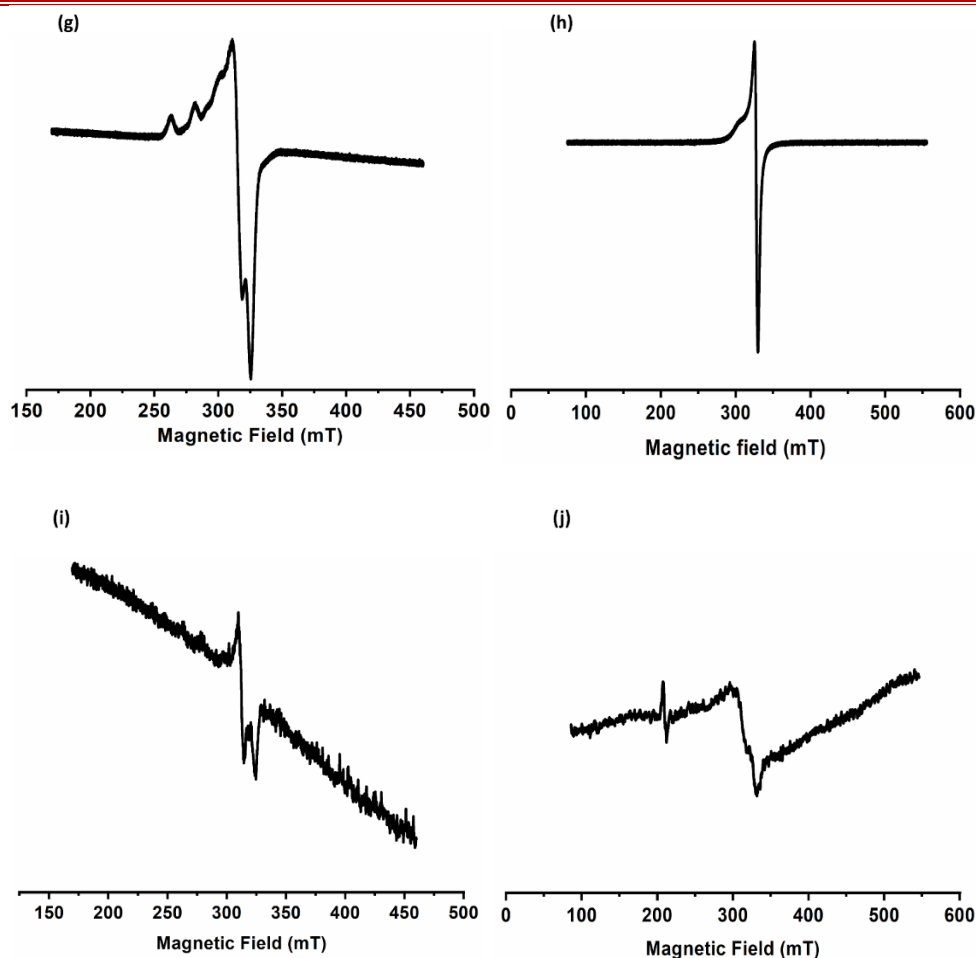


Figure 3.3.2.7.1 (Contd....) ESR spectra of complexes at LNT (g) C7 (DMSO) (h) C7 (powder)(RT) (i) C8 (DMSO) (j) C8 (powder)(RT)

3.3.2.8 Molecular Modelling

Computational studies for understanding the electronic structure of **complexes C1-C3** were performed by optimizing the theoretical geometrical parameters to get ground state structures in the gas phase using GAUSSIAN 16 program^{78,80–82}. The calculated bond parameters are summarized (see SI in **Table. S3.1**). The geometries of the complexes were optimized by B3LYP and LANL2DZ basis set (**figure 3.3.2.7.1**). Contour plots of HOMO and LUMO and their energy gap ΔE_g is shown in **figure 3.3.2.7.2**. These energy gap ΔE_g plays an essential role in deciding their enzyme mimic and other biological activity⁸⁴. This energy gap gives an idea about the chemical interaction of a molecule with other species. The frontier molecular orbitals, LUMO and HOMO acts as electron acceptor and electron donor⁸⁵, respectively. Theoretical transition energy between HOMO and LUMO frontier molecular orbitals were calculated by B3LYP and LANL2DZ methods in

complexes **C4-C8** and are listed in **table 3.3.2.7.1**). This ΔE_g value reflects upon its catalytic activity^{86,87}. The ΔE_g value for complex **C7** is the lowest which reflects the relationship with its SOD mimic activity which is very low as compared to other for SOD mimics reported so far^{86,87}. The energy gap (ΔE_g) in the complexes follows the order: **C7** < **C8** < **C5** < **C4** < **C6**. The graphical representations of ESP in **complexes C4-C8** are shown in **Figure 3.3.2.7.3**. The energy gap (ΔE_g), E_{HOMO} and E_{LUMO} values are important for the prediction of global reactivity descriptors, which in details explains the internal charge transfer, stability and reactivity of the molecule⁸⁷. Global reactivity descriptors such as electronegativity (χ), global hardness (η), global electrophilicity (ω) and global softness (σ) are calculated using the formulas based on Koopmans theorem⁸⁸ (**equations 2.3 to 2.7** in chapter 2 **section 2.3.2.9**) (**Table 3.3.2.7.1**).

Table 3.3.2.7.10 Global reactivity descriptors of complexes in eV calculated by DFT/B3LYP/LANL2DZ basis set

Molecular Properties	Mathematical Description	C4	C5	C6	C7	C8
E_{HOMO}	Energy of HOMO	-11.0508	-5.6409	-5.5081	-7.5286	-5.5661
E_{LUMO}	Energy of LUMO	-9.4919	-4.1810	-3.8942	-6.2992	-4.3190
Energy gap	$\Delta E_g = E_{LUMO} - E_{HOMO}$	1.5589	1.4599	1.6139	1.2294	1.2471
Ionization potential (IP)	$IP = -E_{HOMO}$	11.0508	5.6409	5.5081	7.5286	5.5661
Electron Affinity (EA)	$EA = -E_{LUMO}$	9.4919	4.1810	3.8942	6.2992	4.3190
Electronegativity (χ)	$\chi = -\frac{1}{2}(E_{HOMO} + E_{LUMO})$	10.2714	4.9110	4.7012	6.9139	4.9426
Chemical Potential (μ)	$\mu = \frac{1}{2}(E_{HOMO} + E_{LUMO})$	-10.2714	-4.9110	-4.7012	-6.9139	-4.9426
Global Hardness (η)	$\eta = \frac{1}{2}(E_{HOMO} - E_{LUMO})$	0.7795	0.7300	0.8070	0.6147	0.6236
Softness (S)	$S = 1/2\eta$	0.6414	0.6849	0.6196	0.8134	0.8018
Electrophilicity index (ω)	$\omega = \mu^2/2\eta$	67.6726	16.5191	13.6935	38.9111	19.5873

The optimized structures of all synthesized complexes (**C4-C8**) are depicted in **figure 3.3.2.7.1**. Each copper(II) ions are four and five coordinated in complexes **C4**, five coordinated in complex **C5**, **C6** and **C7**, six coordinated in complex **C8**. Both copper ions are coordinated by oxygen of nitrate and one copper ion with oxygen

of other nitrate anion in **C4** and both copper ions are coordinated by oxygen of perchlorate anion in **C6**.

In complex **C5**, both copper ions are coordinated by phenolic oxygen, imine nitrogen, amino nitrogen of morpholine, two oxygen of each of two perchlorate anions. In **complex C7**, both copper ions are coordinated by phenolic oxygen, imine nitrogen, nitrogen of pyridine and two oxygen of each of two acetate anions. The **complex C8** is formed by two unsymmetrical tridentate ligands chelating the metal ions and forming a phenoxide bridged copper(II) dimer. Both copper ions are coordinated by two phenolic oxygen, two imine nitrogen, two carbonyl oxygen and two oxygen of each of two perchlorate anions in antiperiplanar conformation. Besides these, some important geometrical parameters such as bond angles, bond lengths, torsion angle related to the complexes are listed in **Table S3.1**.

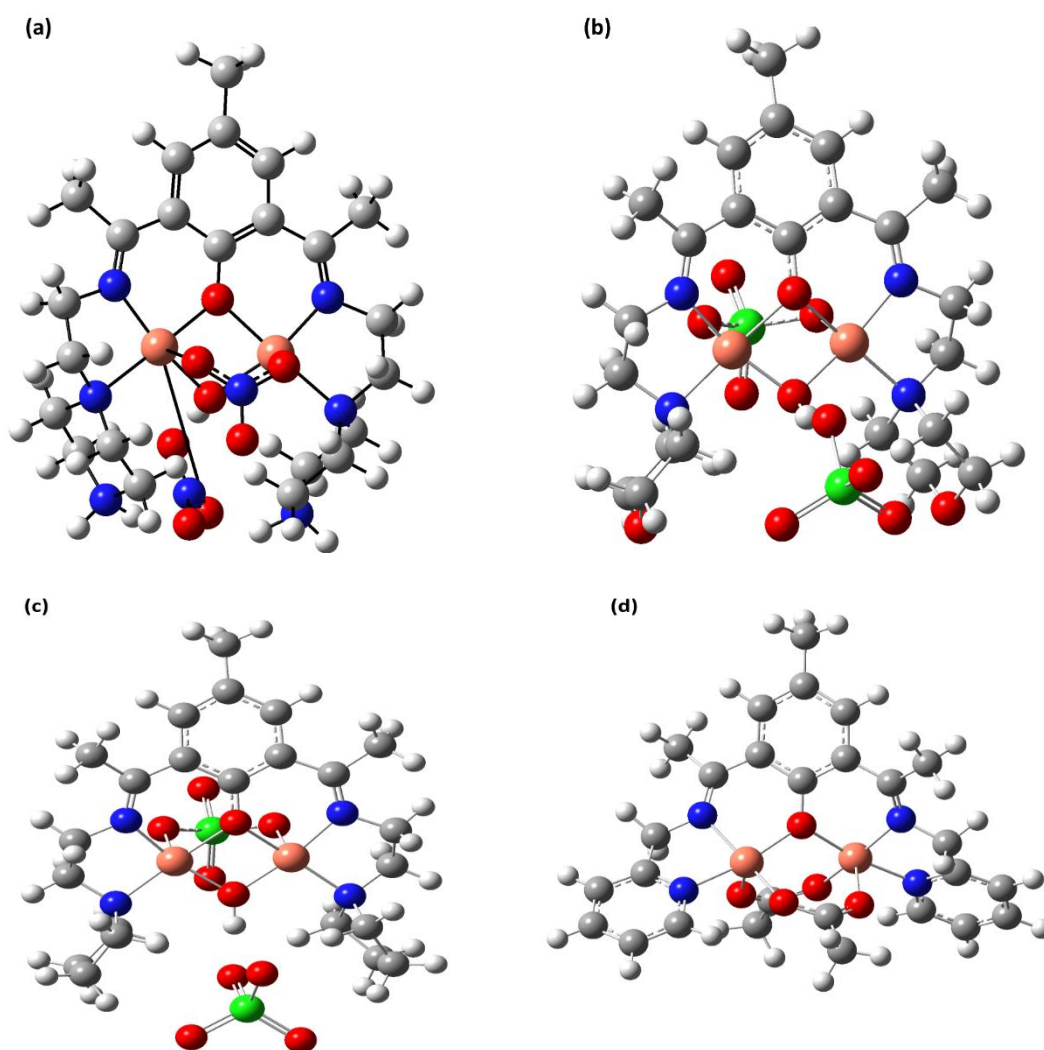


Figure 3.3.2.7.1 DFT optimized structure of complexes (a)**C4** (b) **C5** (c) **C6** (d) **C7**

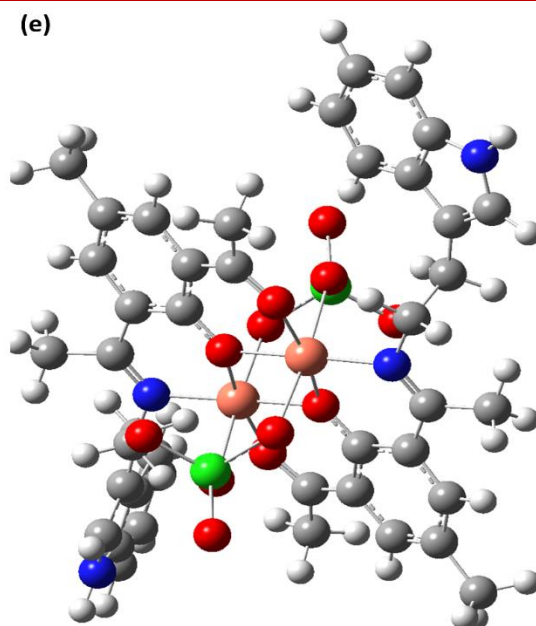


Figure 3.3.2.7.1 (Contd...) (e) DFT optimized structure of complex C8

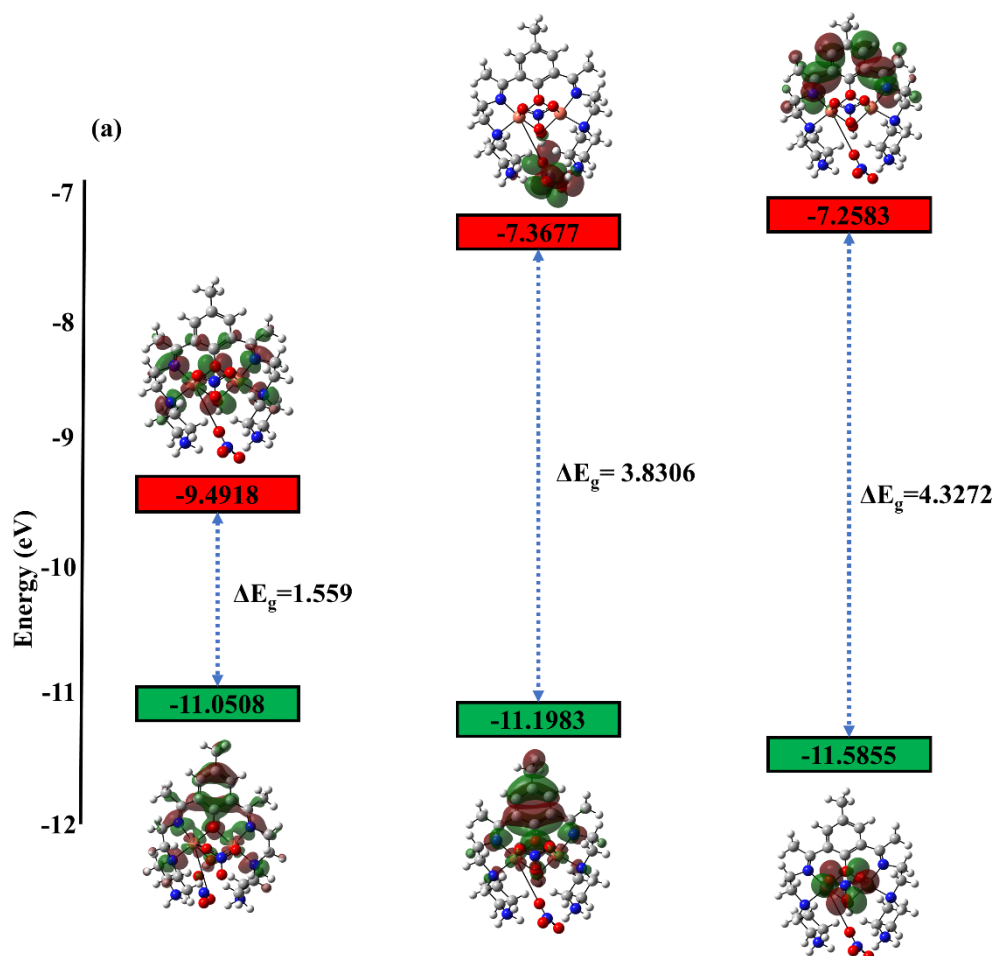


Figure 3.3.2.7.2 (a) Frontier molecular orbitals of complex C4

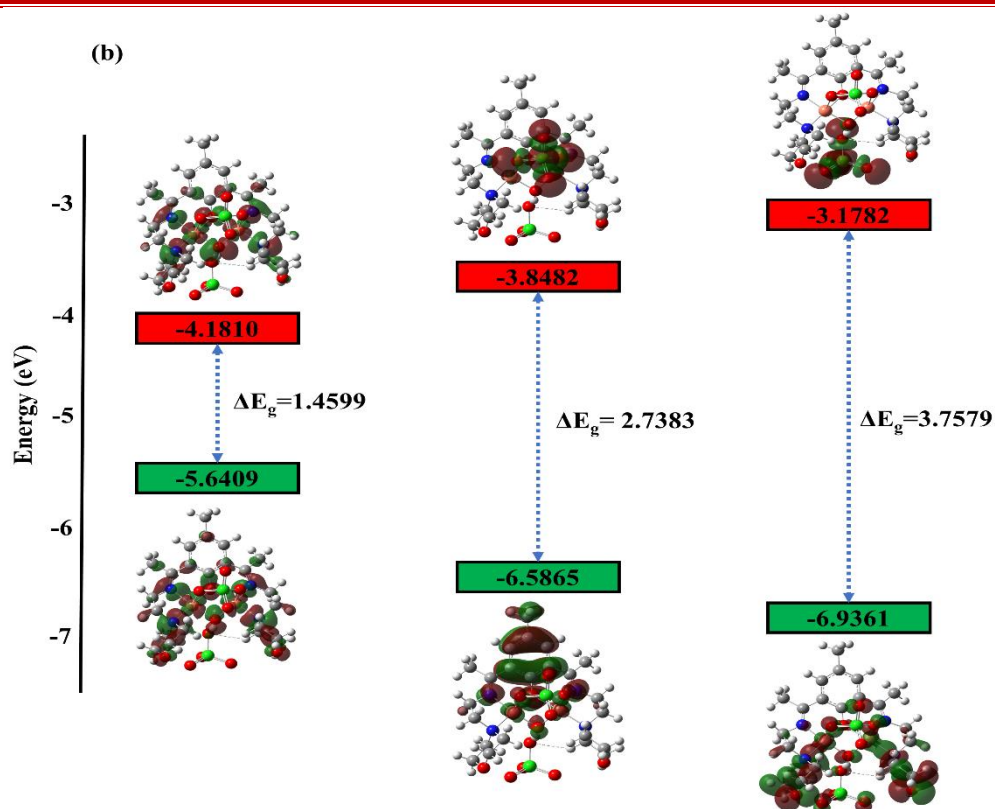


Figure 3.3.2.7.2 (Contd...) (b) Frontier molecular orbitals of complex C5

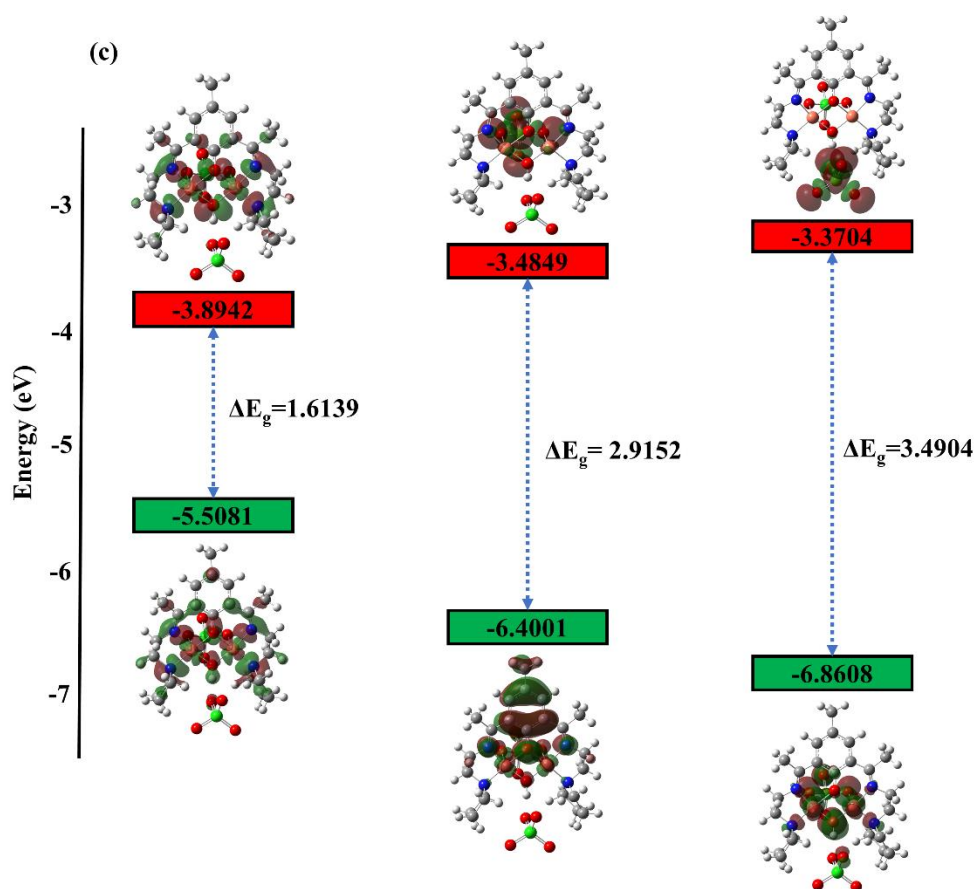


Figure 3.3.2.7.2 (Contd...) (c) Frontier molecular orbitals of complex C6

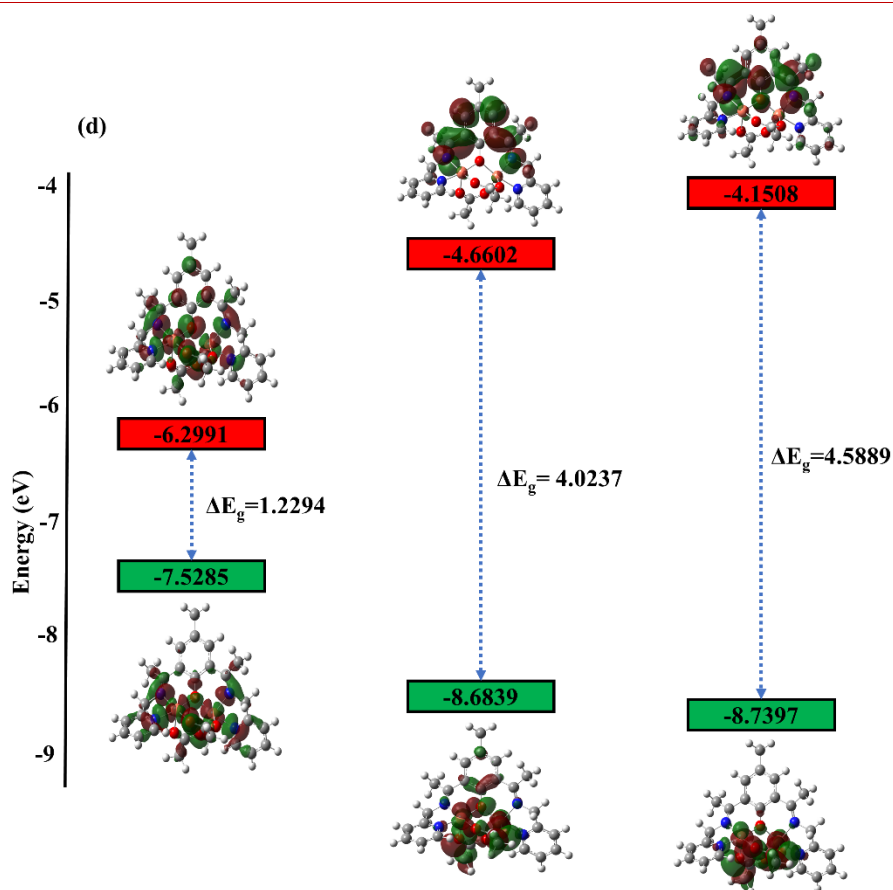


Figure 3.3.2.7.2 (Contd...) (d) Frontier molecular orbitals of complex C7

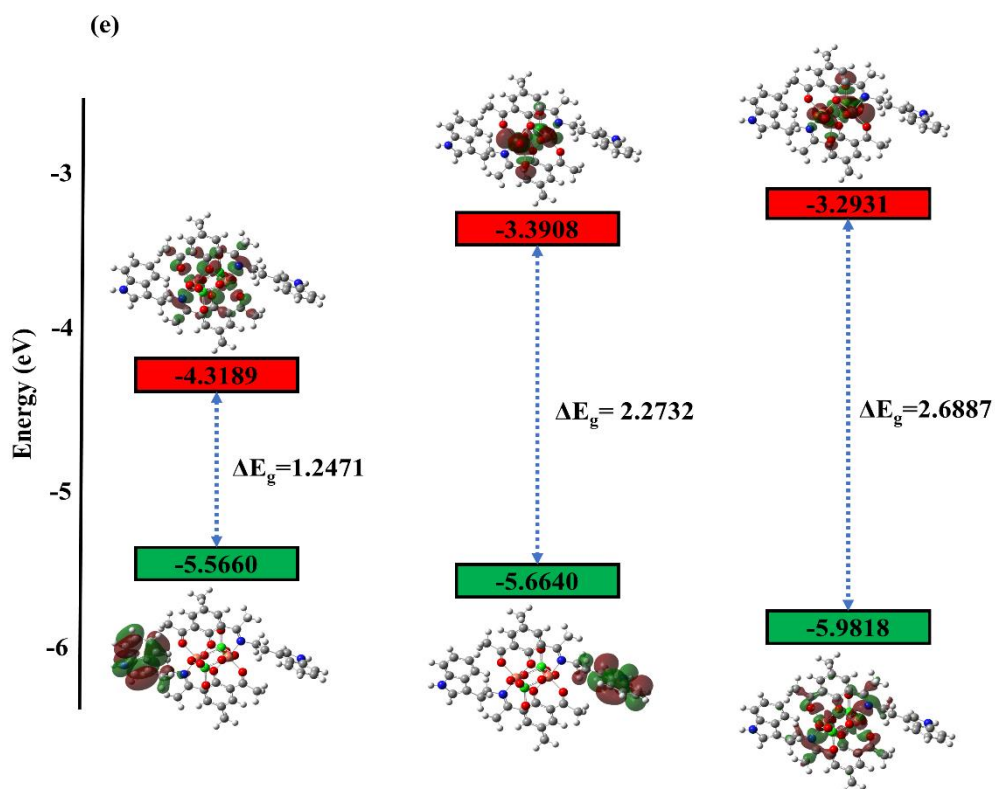


Figure 3.3.2.7.2 (Contd...) (e) Frontier molecular orbitals of complex C8

The calculated bond lengths of Cu-N and Cu-O of these complexes are comparable to those obtained from single crystal X-ray data. This validates the models. In all the complexes, HOMO and LUMO along with their two upper and two lower orbitals exhibits different localization indicating intramolecular electron charge transfer within the molecule. The energy gap (ΔE_g) value is directly associated with the stability and hardness and inversely related with the reactivity and softness of the molecule. The very small energy gap values shows that there is an easy charge transfer within the molecule, which may further increase the biological activity of the complex.

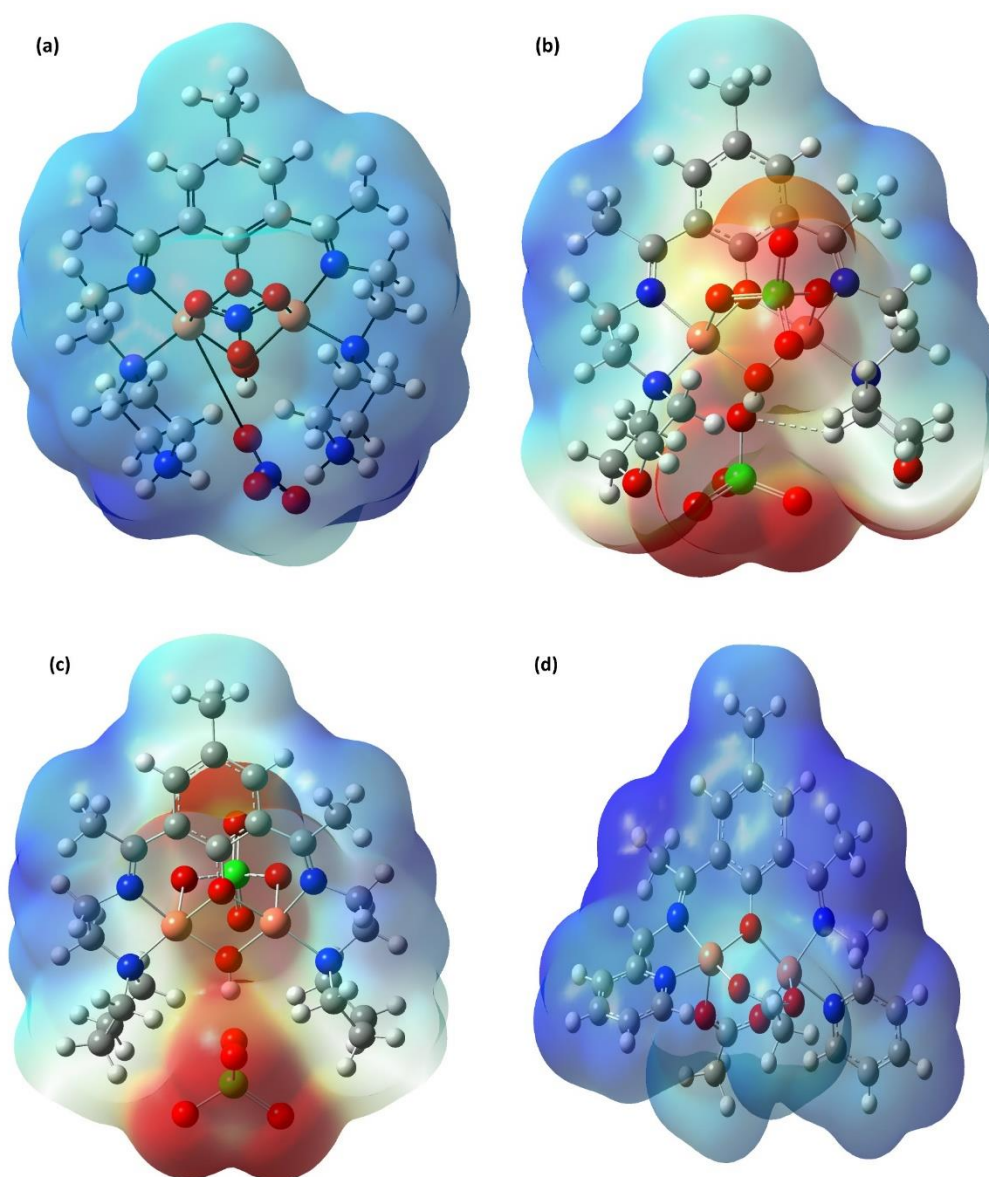


Figure 3.3.2.7.3 Electrostatic potential of complexes (a) C4 (b) C5 (c) C6 (d) C7

(e)

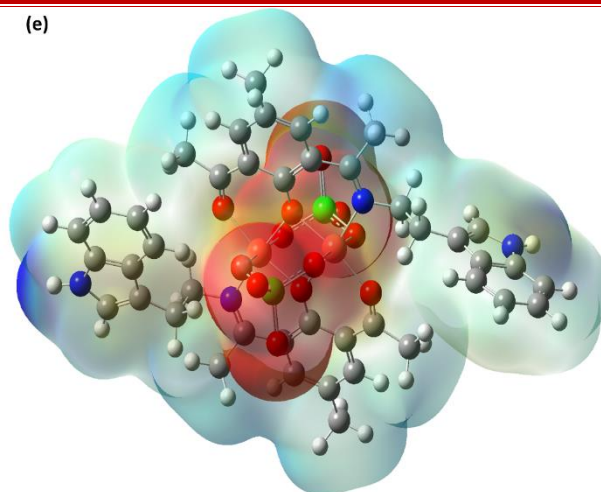


Figure 3.3.2.7.3 (Contd...) (e) Electrostatic potential of complex C8

3.3.3 SOD mimic activity

Generation of superoxide anion ($O_2^{\cdot-}$) is responsible for the conversion of NBT to monoformazan complex and its scavenging from the system by the copper(II) complexes (**scheme 2.2.4.1** in chapter 2 **section 2.2.4**). The hydrogen donor NADH reduces PMS. This reduced PMS generates $O_2^{\cdot-}$ from dissolved O_2 . NBT gets reduced by $O_2^{\cdot-}$, which results in a linear accumulation of blue formazan with increase in the absorbance at 560nm (**Scheme 2.3.3.1** in chapter 2 **section 2.3.3**).

In the reaction medium, SOD or SOD mimic compounds scavenge $O_2^{\cdot-}$ which results in decrease in the formation of formazan. The % inhibition of NBT reduction at various concentrations of complexes as a function of time was measured by measuring the absorbance at 560nm. **Figure 3.3.3.1** represents the plot of absorbance (A_{560}) against time (t) with varying concentration of complexes required to yield % inhibition of the NBT reduction. The ligands show very low % inhibition at 100 μ M concentration of ligand. E.g. the % inhibition of NBT reduction was found to be 15.11 % for **L⁸** at 100 μ M concentration. This confirms that ligand, **L₈** does not show good SOD mimic activity. (**Figure 3.3.3.1 (f)**)

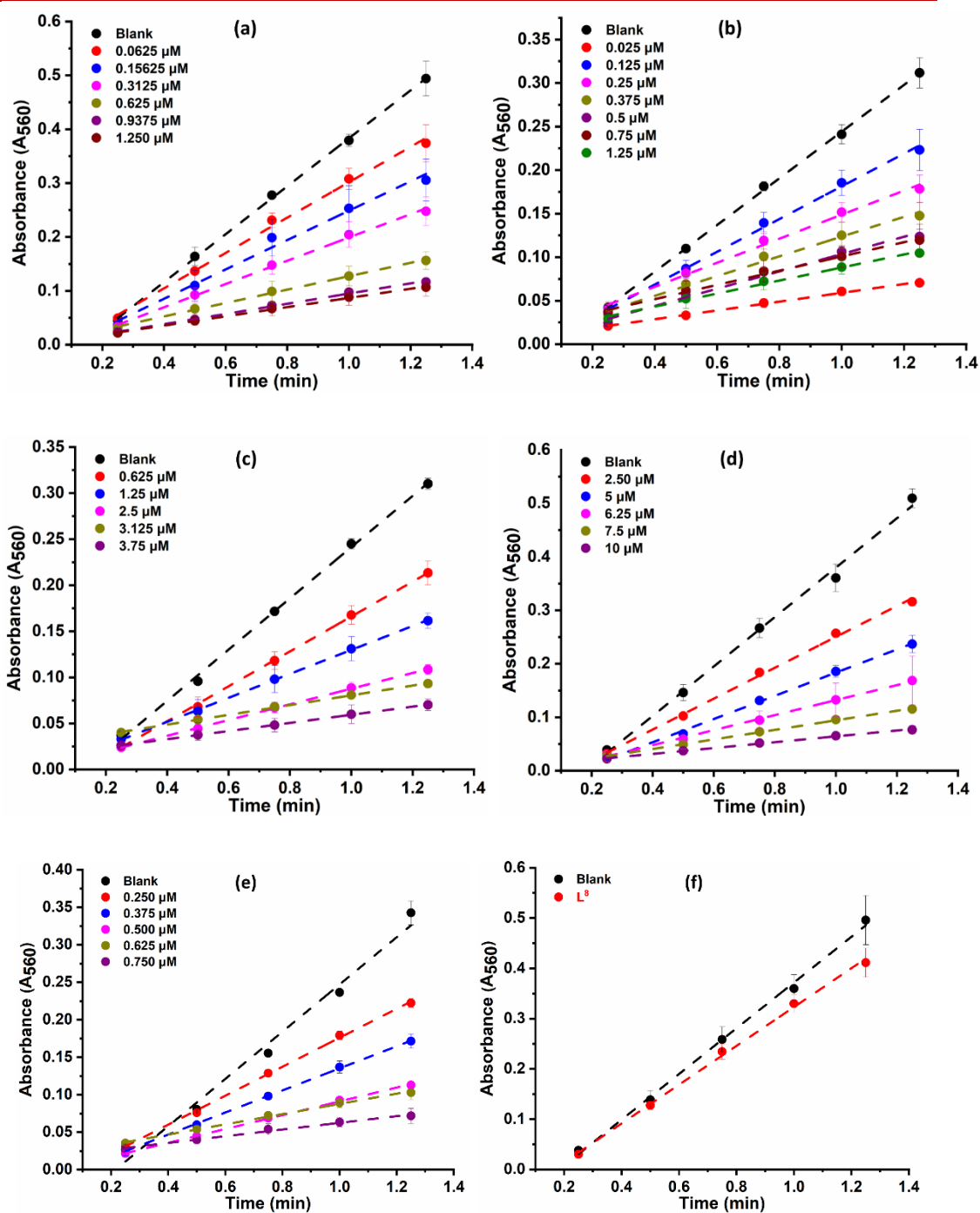


Figure 3.3.3.1 Plot of Absorbance (A_{560}) as function of time (min) (a) C4 (b) C5 (c) C6 (d) C7 (e) C8 and (f) L^8

Figure 3.3.3.2 represents % inhibition of NBT reduction as a function of increasing concentrations of complexes. These plots are further used to determine the IC_{50} value i.e. the scavenger concentration causing 50% inhibition of reduction of NBT where the scavenger is each complex.

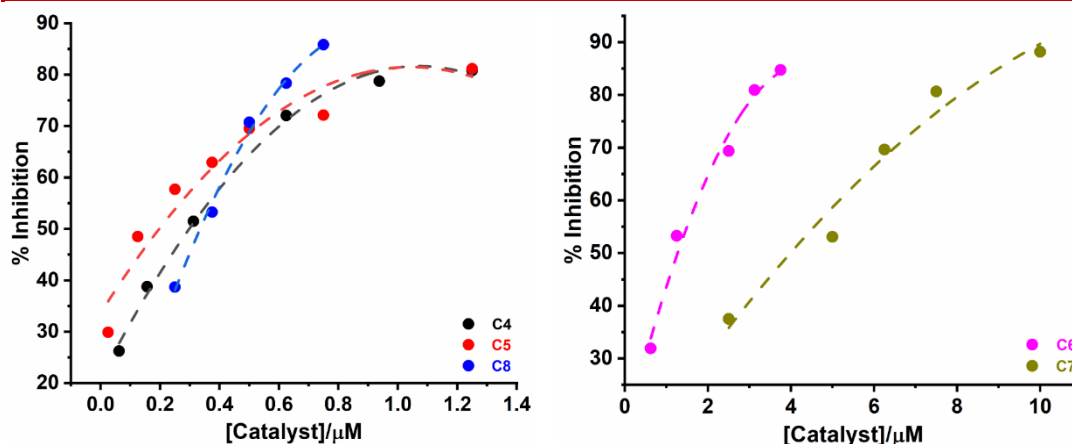


Figure 3.3.3.2 Plot of % inhibition of NBT reduction vs. concentration of complexes

The dicopper(II) complexes, **C4-C8**, exhibit SOD-like activity at the biological pH with lower IC_{50} values ranging from 0.128-4.05 μM . The complexes show better SOD mimic activity than those reported in the literature.^{45,46,62,68,73,89} The results have been summarized in **Table 3.3.3.1**.

Table 3.3.3.1 IC_{50} values of complexes(**C4-C8**) and ligand **L⁸** and native enzyme

Complexes	$IC_{50}/\mu\text{M}$
C4	0.242
C5	0.128
C6	1.157
C7	4.05
L⁸	>100
C8	0.329
Native enzyme (SOD)	0.04

3.3.4 Ascorbic Acid Oxidase (AAO) activity

The oxidation of AA as catalyzed by complexes by dissolved O_2 as oxidant in acetate buffer (pH 5.5) was monitored by measuring absorbance at $\lambda_{\text{max}} = 265\text{nm}$ using UV-Vis spectroscopy. A distinct absorption maximum at $\lambda_{\text{max}} = 265\text{nm}$ (marked as 'a') was observed for ascorbic acid (AA) in **figure 3.3.4.1 (a)**. However, when complexes were incubated in presence of AA under aerobic conditions, a significant decrease in absorbance (marked as 'b') was noted which demonstrated the fact that AA was consumed in a reaction (**figure 3.3.4.1 (a)**). But when the same experiment was carried out under nitrogen atmosphere, there was no significant decrease in the absorbance at $\lambda_{\text{max}} = 265\text{nm}$ (marked as 'c') which confirms the involvement of O_2 in the reaction (**figure 3.3.4.1(a)**).

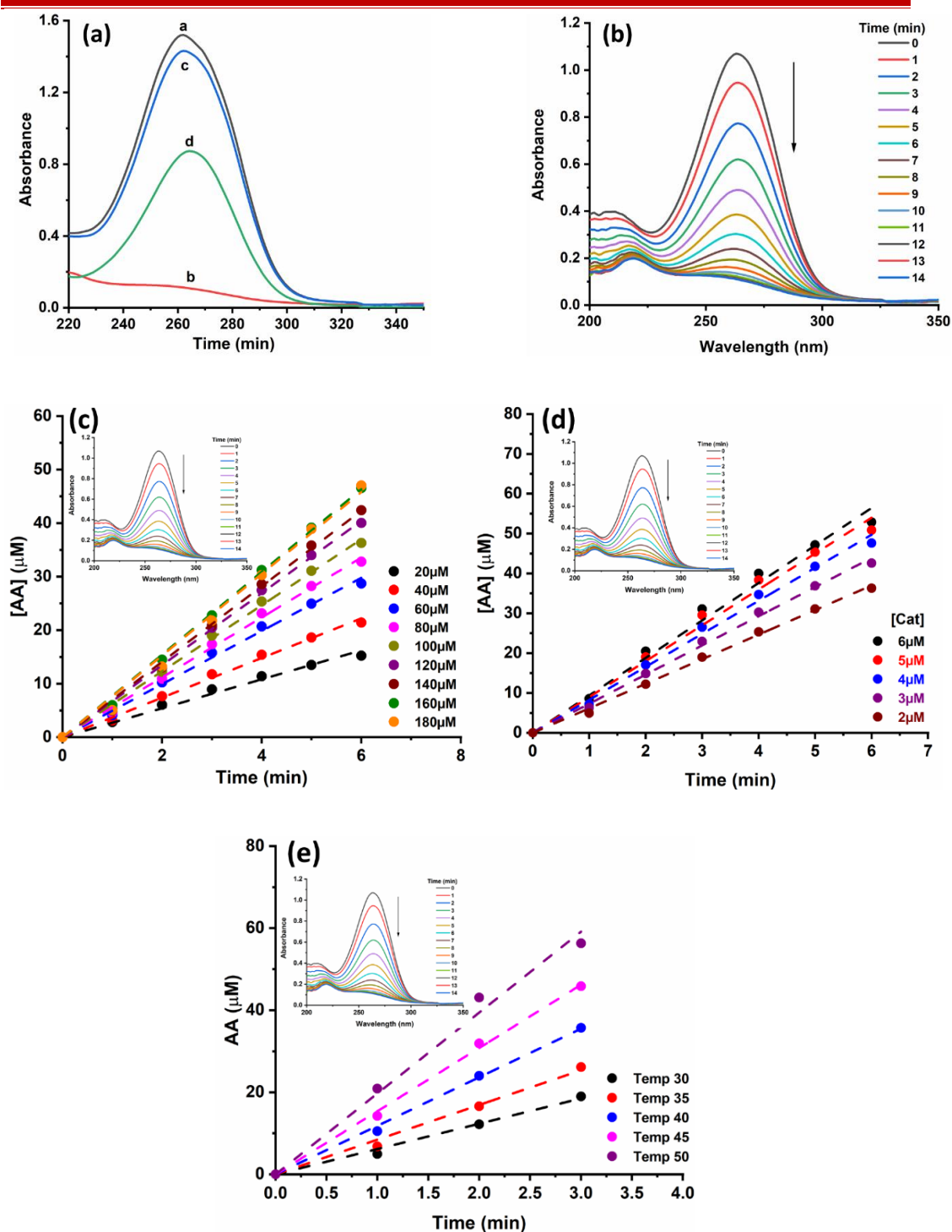


Figure 3.3.4.1 (a) Uv-Vis spectra of a: AA, b: AA+C4 under aerobic conditions, c: AA+C4 under N_2 atm. for 20 mins and d: AA+Cu(OAc)₂ under aerobic conditions for 20 mins, (b) Time dependent spectral changes from 0 to 14 mins for C4 catalyzed oxidation of AA and (c)-(e) Plots of [AA] as function of time with varying concentrations of substrate (c), catalyst (d) and temperature (e) (Inset: Plot of absorbance vs wavelength at different time interval)

With various concentrations of ascorbic acid (AA), Michaelis-Menten constant (K_m) can be obtained from Michaelis-Menten equation (equation 2.8 in section 2.3.4 in chapter 2). The Michaelis-Menten constant (K_m) and maximum rate (V_{max}) were calculated from Lineweaver-Burk plot. These parameters, K_m and catalytic rate (k_{cat}), help in understanding the kinetic of the enzymatic / enzyme mimetic reactions.

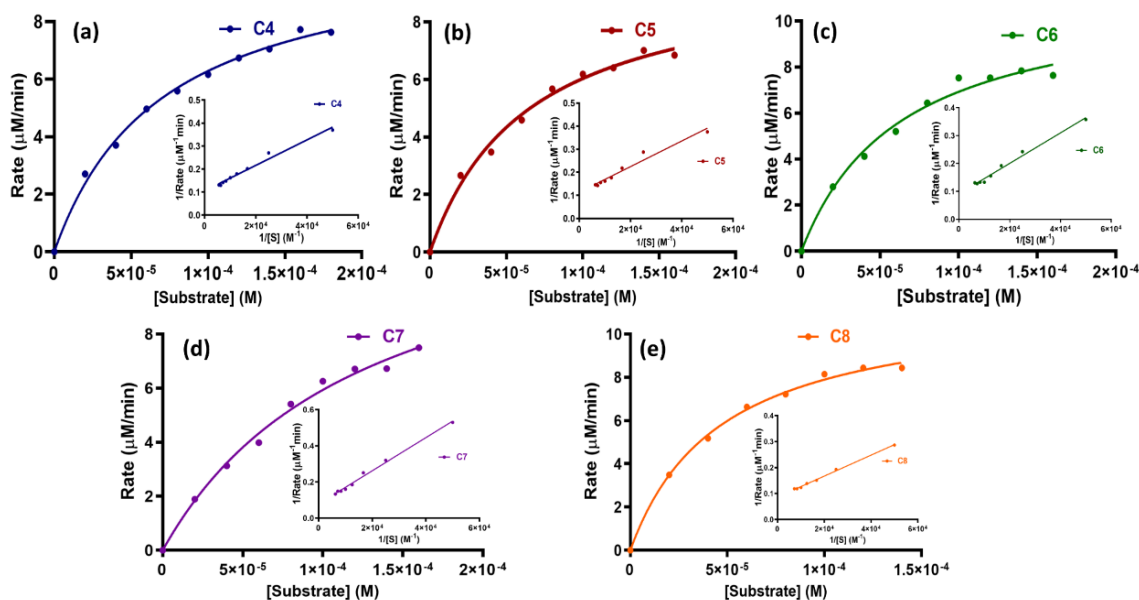


Figure 3.3.4.2 Rate vs [substrate] plot of Michaelis-Menten model for complexes (a) C4 (b) C5 (c) C6 (d) C7 and (e) C8 (Inset: Lineweaver-Burk plot of respective complexes)

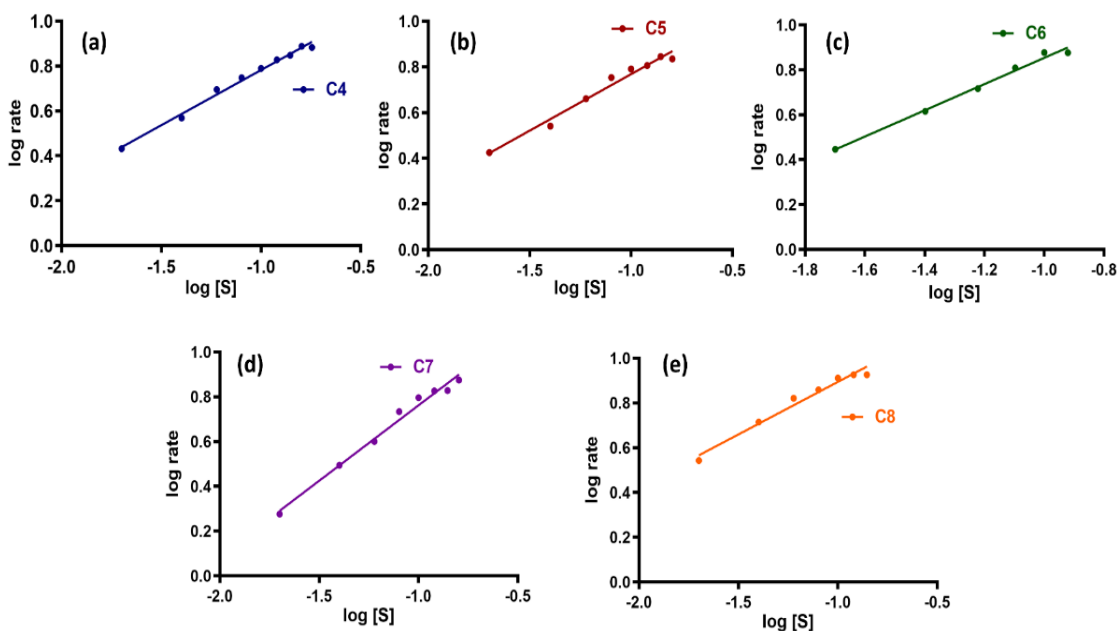


Figure 3.3.4.3 Plot of $\log(\text{rate})$ vs $\log[\text{S}]$ for complexes (a) C4 (b) C5 (c) C6 (d) C7 and (e) C8

The order of reaction with respect to substrate was obtained from slope of the plot of $\log(\text{rate})$ as function of $\log[\text{substrate}]$ (**Figure 3.3.4.3**). While order with respect to catalyst was obtained from slope of the plot of $\log(\text{rate})$ as function of $\log[\text{catalyst}]$ (**figure 3.3.4.4**). It was found to be half order with respect to substrate as well as catalyst.

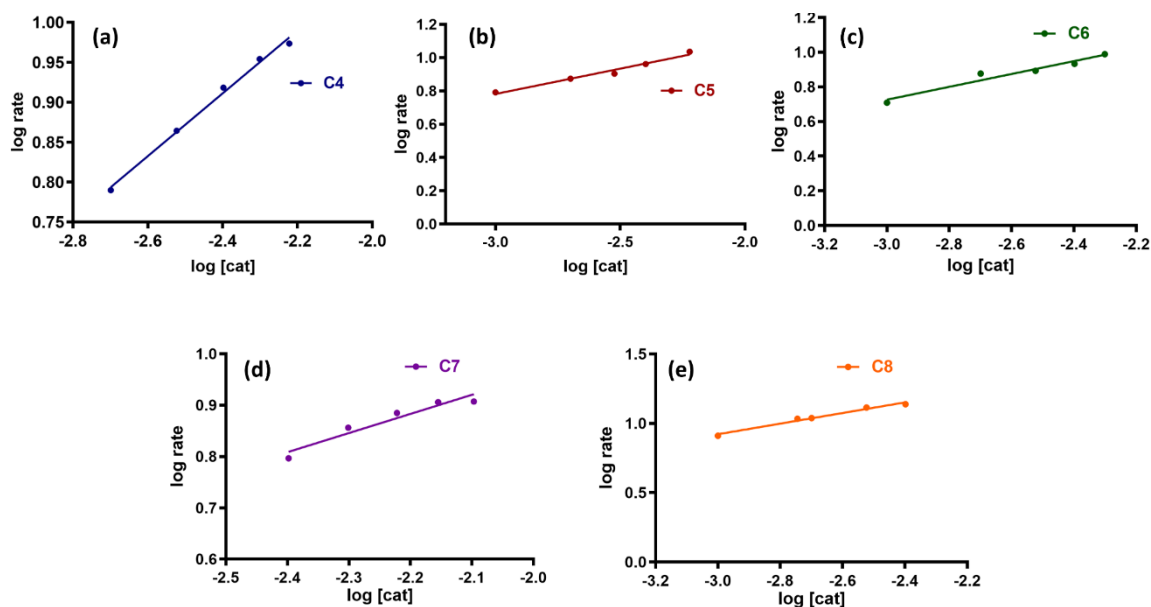


Figure 3.3.4.4 Plot of $\log(\text{rate})$ vs $\log [\text{Cat}]$ for complexes (a) C4 (b) C5 (c) C6 (d) C7 and (e) C8

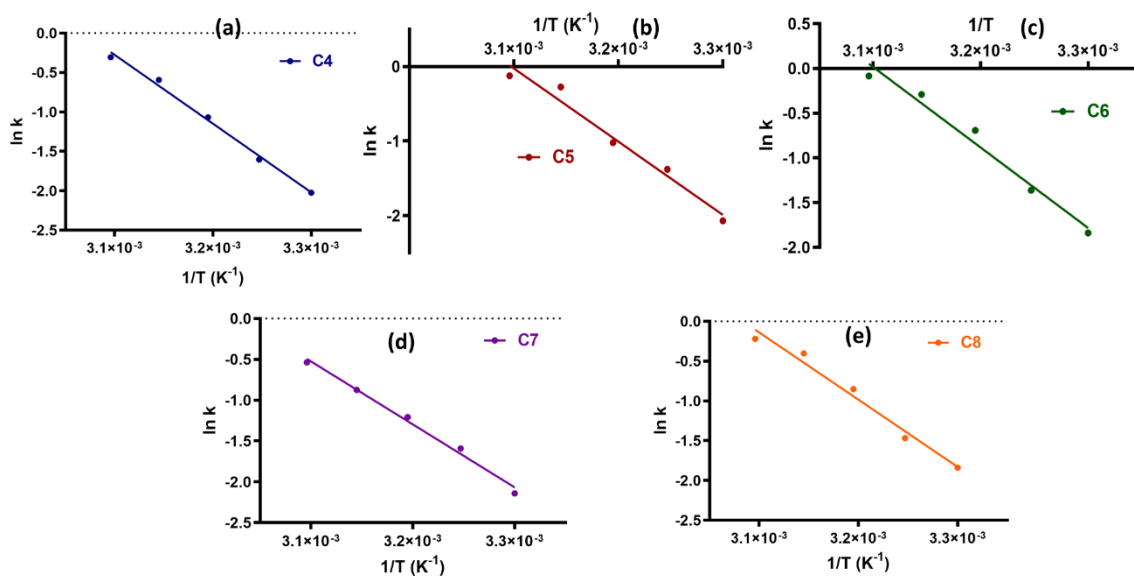


Figure 3.3.4.5 Arrhenius plot of all complexes (a) C4 (b) C5 (c) C6 (d) C7 and (e) C8

Activation energy of the reaction was found from the Arrhenius plot (**figure 3.3.4.5**). The Activation energy required for the conversion of AA to DHAA is in the range of 70-79.03 kJ/mole for the complexes, **C4-C8**.

The kinetic parameters of AA in the presence of complexes, order and activation energy have been summarized in **Table 3.3.4.1**.

Table 3.3.4.1 Kinetic parameters of AA in presence of complexes

Complex	K _m (M)	V _{max} (μM/min)	[E] (M)	k _{cat} /h ⁻¹	Order		E _a (kJ/mole)
					Cat	Sub	
C4	10.70	7.02 x 10 ⁻⁵	2 x 10 ⁻⁶	3.21 x 10 ²	0.39	0.49	77.44
C5	9.913	6.435 x 10 ⁻⁵	4 x 10 ⁻⁶	5.95 x 10 ²	0.30	0.495	71.48
C6	11.32	6.35 x 10 ⁻⁵	2 x 10 ⁻⁶	3.40 x 10 ²	0.37	0.58	74.65
C7	13.43	1.26 x 10 ⁻⁵	2 x 10 ⁻⁶	2.02 x 10 ²	0.45	0.674	79.03
C8	12.08	5.1 x 10 ⁻⁵	4 x 10 ⁻⁶	7.25 x 10 ²	0.425	0.469	70.16
AAO⁹⁰	0.08 (mM)	6.5 (10 ⁴ mM/s)	0.179 x 10 ⁻⁸	9.7 x 10 ⁴	-	-	-
Copper Salt	-	-	-	-	-	-	89.085
No complex	-	-	-	-	-	-	138.99

The presence of any superoxide formed during the reaction was checked spectroscopically and it was found to be absent. Mechanism as explained in section 2.3.4 in chapter 2 (**Figure 2.3.4.6**).

The presence of any superoxide formed during the reaction was checked spectroscopically and it was found to be absent. The presence of peroxide has also been analyzed spectrophotometrically, using a literature procedure⁹¹⁻⁹³ as described in chapter 2 section 2.3.4.⁹¹⁻⁹³. The formation of H₂O₂ during the catalytic reaction was detected by following the development of the characteristic band of I₃⁻ spectrophotometrically ((See SI†: **Fig. S.3.25**) (λ_{max}= 353 nm; ε= 26000 M⁻¹cm⁻¹), upon reaction with I₂).

Based on the observations the same mechanism as proposed in chapter 2 is applicable for the reactions in presence of complexes **C4-C8** as catalysts.

3.3.5 Catecholase activity

In the present study, five substrates, 3,5-DTBC, 4-methyl catechol, dopamine, pyrocatechol and 2,3-dihydroxy naphthalene have been employed to study the catecholase activity of all **C4-C8** complexes. The reaction with pyrocatechol, dopamine and 2,3-dihydroxy naphthalene was found to be very slow. The corresponding quinone band in dopamine, pyro- catechol and 2,3-dihydroxy naphthalene had negligible appearance even after 24 hrs of reaction time indicating negligible catalytic activity of the complex for these three substrates. All complexes were found to be active for 3,5-DTBC and 4-methyl catechol substrates. Hence, detailed kinetic studies have been carried out with 3,5-DTBC and 4-methylcatechol as explained in **section 2.3.5** in Chapter 2. The course of a typical reaction with **complex C5** as catalyst (**Figure 3.3.5.1 (a)**) for 3,5-DTBC and for other complexes for both substrates has been represented in **SI† Fig 3.16(a), 3.17A-B(a), 3.18A-B(a), 3.19A-B(a) and 3.20A-B(a)** inset graph. The substrate 3,5-DTBC / 4-methyl catechol was added at once to the solution of the complex and the spectra were recorded. The MLCT band in the complex disappeared and a new band corresponding to 3,5-DTBQ / 4-methyl quinone started appearing at 380–410 nm. A linear increase in the absorption of this band was observed. The kinetics of oxidation of 3,5-DTBC and 4-methyl catechol was determined by the method of initial rates as a function of time (**figure 3.3.5.1 (b-d)** for **C5** (3,5-DTBC) and **SI† Fig. 3.16-3.20(b-d)** for other complexes for both substrates).

The analysis of the data based on the Michaelis- Menten model, originally developed for enzyme kinetics, was applied. In **figure 3.3.5.2 (a-e)**, the solid circles are experimental data and the solid curves are the fits to the Michaelis-Menten model for all complexes with 3,5-DTBC (for 4-MC see **SI† Fig S3.20**). With various concentrations of substrates, Michaelis-Menten constant (K_m) can be obtained from the Michaelis Menten equation. The Lineweaver-Burk plot for all complexes with 3,5-DTBC are depicted in inset of **Figure 3.3.5.2 (a-e)** while for 4-MC (See **SI† Fig. S3.21 Inset**).

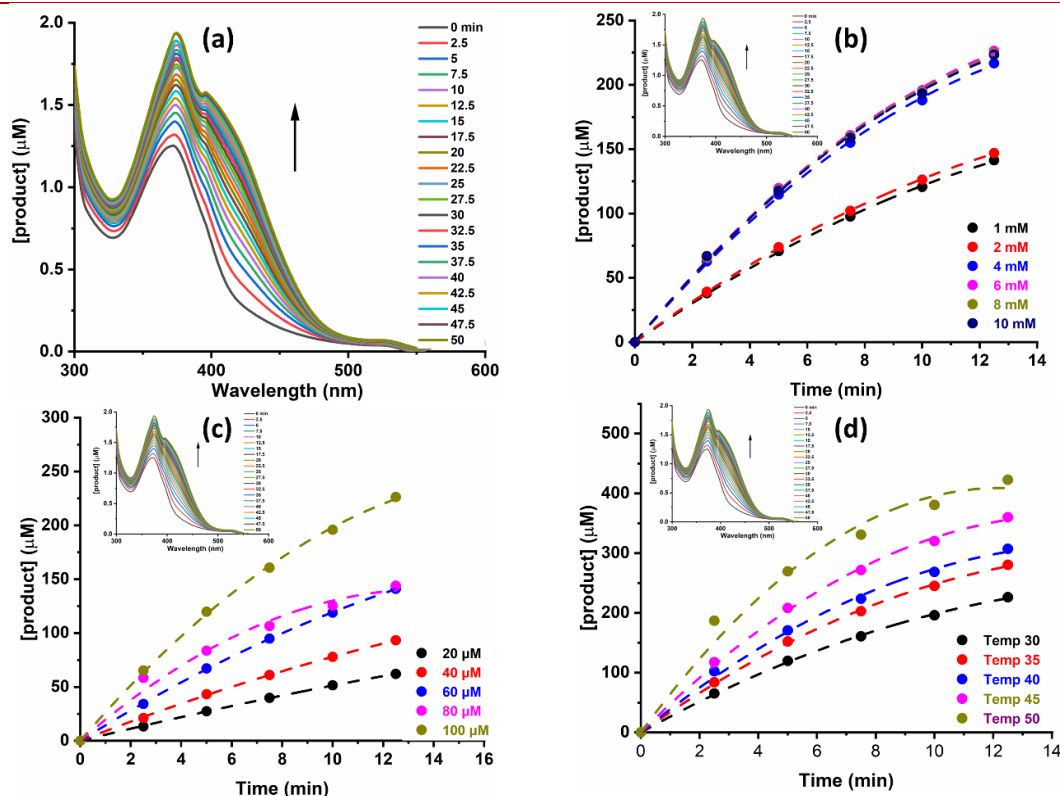


Figure 3.3.5.1 (a) Time dependent spectral changes over a time period of 0-15 min for C5 catalyzed oxidation of 3,5-DTBC. (b-d) Plot of [product] as function of time with respect to (b) substrate, (c) catalyst (c) and (d) temperature (Inset: Plot of absorbance vs wavelength at different time interval) for complex C5 with 3,5-DTBC

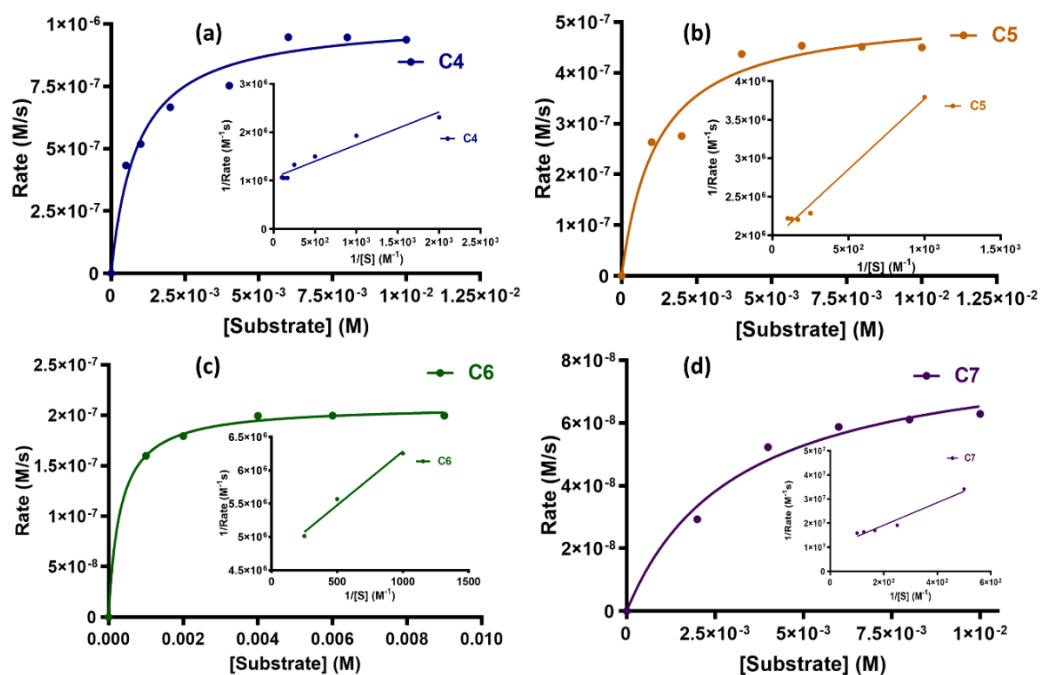


Figure 3.3.5.2 Plot of Rate vs [Substrate] of Michaelis Menten model for complexes (a) C4 (b) C5 (c) C6 (d) C7 (Inset: Lineweaver Burk plot) for 3,5-DTBC

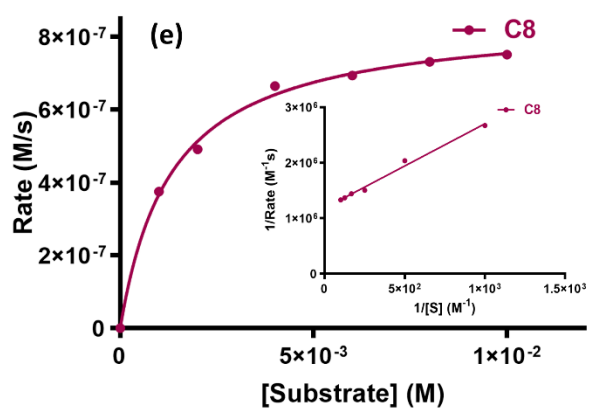


Figure 3.3.5.2 (Contd..) (e) Plot of Rate vs [Substrate] of Michaelis-Menten model for complex C8 (Inset: Lineweaver Burk plot) for 3,5-DTBC

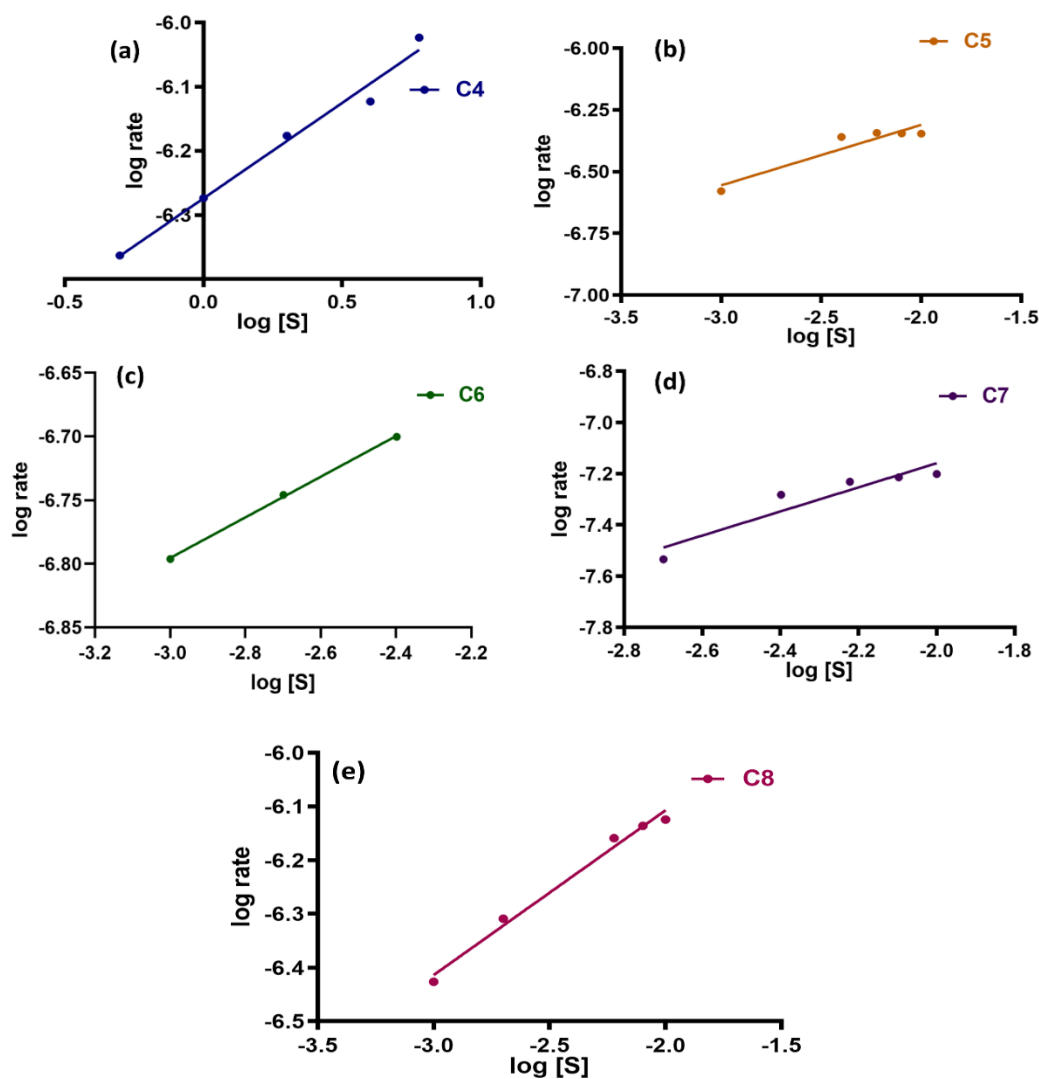


Figure 3.3.5.3 Plot of log rate vs log [Sub] for complexes (a) C4 (b) C5 (c) C6 (d) C7 and (e) C8 for 3,5-DTBC

The plots of $\log(\text{rate})$ versus $\log[\text{substrate}]$ (**Figure 3.3.5.3 (a-e)**) and $\log(\text{rate})$ versus $\log[\text{catalyst}]$ (**Figure 3.3.5.4 (a-e)**) for 3,5-DTBC of all complexes and that for 4-MC (**SI† Fig. 3.22 and 3.23**) indicate that the complex catalysed oxidation of both diphenols to the corresponding quinones follow first order kinetics with respect to the substrate and also with respect to the dicopper(II) monomer of the complexes.

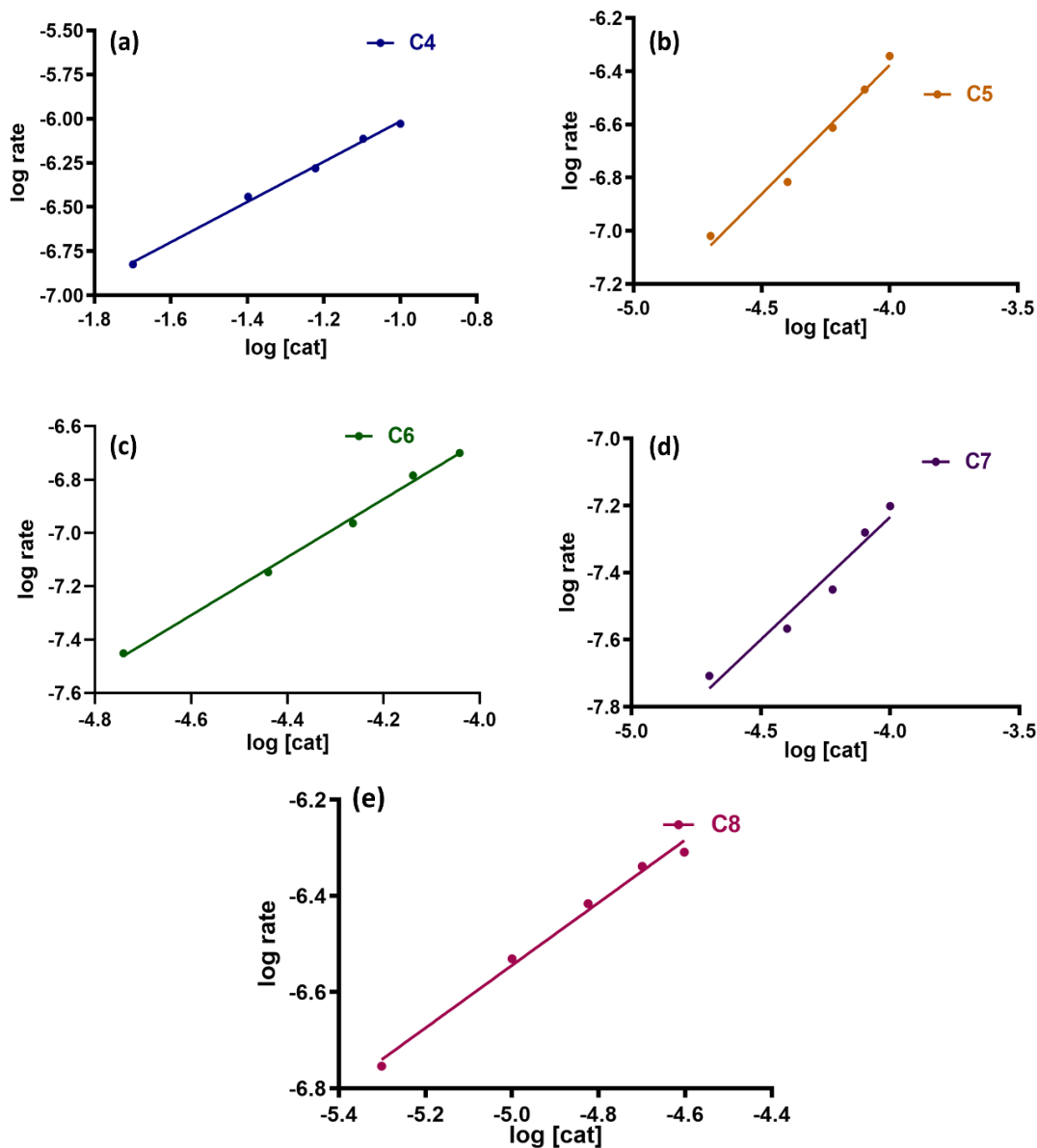


Figure 3.3.5.4 Plot of $\log(\text{rate})$ vs $\log[\text{Cat}]$ for complexes (a) C4 (b) C5 (c) C6 (d) C7 and (e) C8 for 3,5-DTBC

The activation energy values (16-30 kJ/mole) for the oxidation of 3,5-DTBC and 4-methyl catechol (35-40 kJ/mole) in presence of complexes, C4-C8, as catalysts have

been calculated from Arrhenius plot (Figure 3.3.5.5 (a-e)). Those for 4-MC as substrate are included in SI† Fig. S3.24.

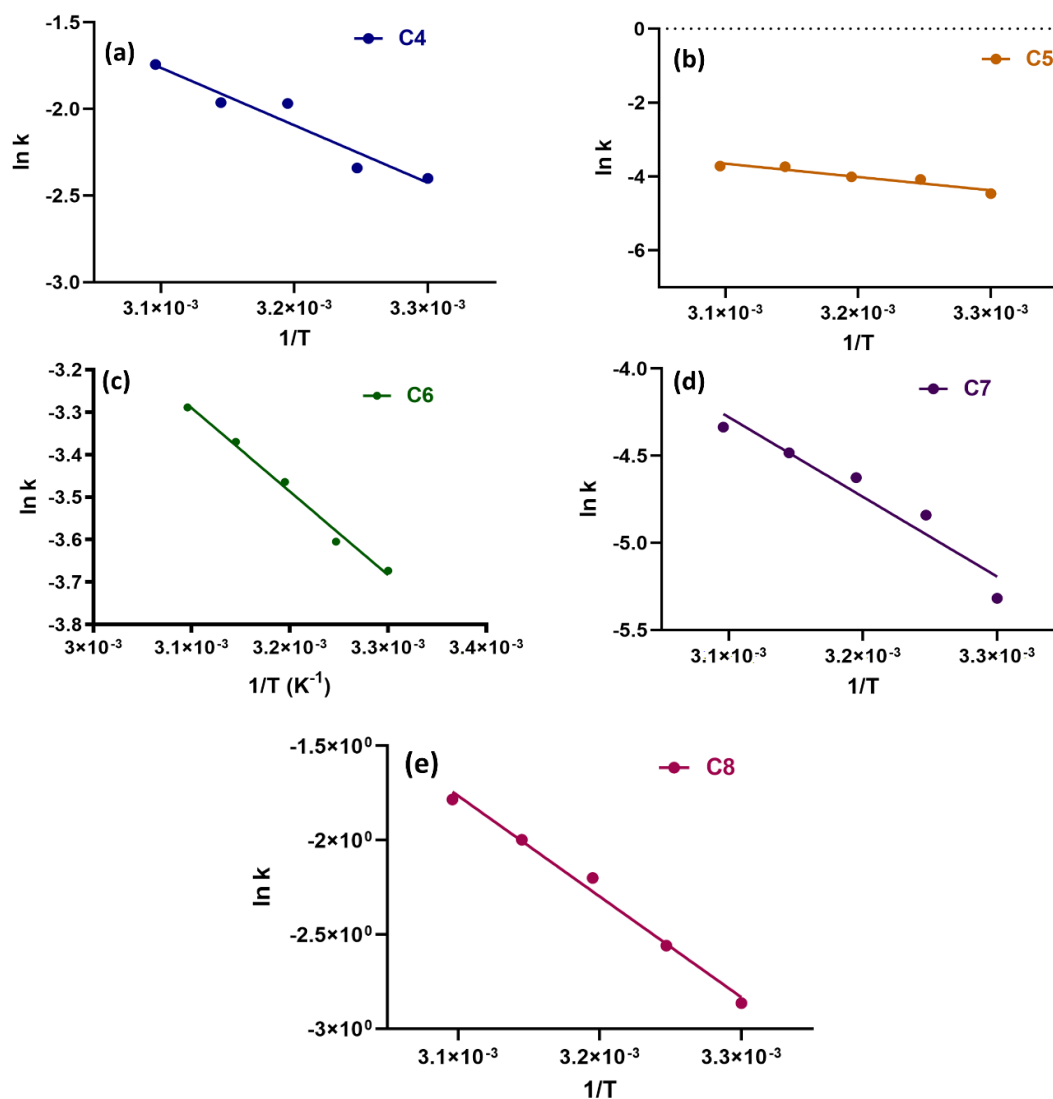


Figure 3.3.5.5 Arrhenius plot of all complexes (a) C4 (b) C5 (c) C6 (d) C7 and (e) C8 for 3,5-DTBC

The kinetic parameters with both substrates in presence of complex catalysts, C4-C8, order with respect to the catalyst and substrate and activation energy are summarized in Table 3.3.5.1.

Table 3.3.5.1 Kinetic parameters of Michaelis Menten model, Order, Activation energy of substrates with different complexes

Complexes	Substrate	V_{max} (M/s)	K_m (M)	k_{cat} (h^{-1})	Order		E_a (kJ/mole)
					Cat	Sub	
C4	3,5-DTBC	1.021×10^{-6}	8.893×10^{-4}	36.8	1.139	0.2978	27.59
	4-MC	4.566×10^{-7}	5.842×10^{-4}	16.4	0.811	0.1253	26.69
C5	3,5-DTBC	5.255×10^{-7}	1.181×10^{-5}	18.9	0.9693	0.2454	30.01
	4-MC	2.475×10^{-7}	7.94×10^{-3}	8.91	0.8241	0.6412	17.68
C6	3,5-DTBC	2.098×10^{-7}	3.12×10^{-4}	232	1.088	0.1595	16.36
	4-MC	8.318×10^{-8}	5.03×10^{-4}	6.61	0.9693	0.2767	39.16
C7	3,5-DTBC	8.865×10^{-8}	8.198×10^{-4}	3.19	0.7304	0.4700	38.05
	4-MC	6.782×10^{-8}	3.112×10^{-4}	2.44	0.8080	0.7313	18.31
C8	3,5-DTBC	8.545×10^{-7}	1.332×10^{-4}	133	0.6508	0.3070	19.77
	4-MC	3.896×10^{-7}	5.220×10^{-4}	14.0	0.2811	1.696	60.09

The presence of any superoxide formed during the reaction was checked spectroscopically and it was found to be absent. The mechanistic pathways of o-diphenol oxidation can involve production of water and/or hydrogen peroxide. The formation of hydrogen peroxide was confirmed using a literature procedure (See **SI†: Fig. S.3.25**) as explained in Chapter 2 **section 2.3.4**.⁹¹⁻⁹³

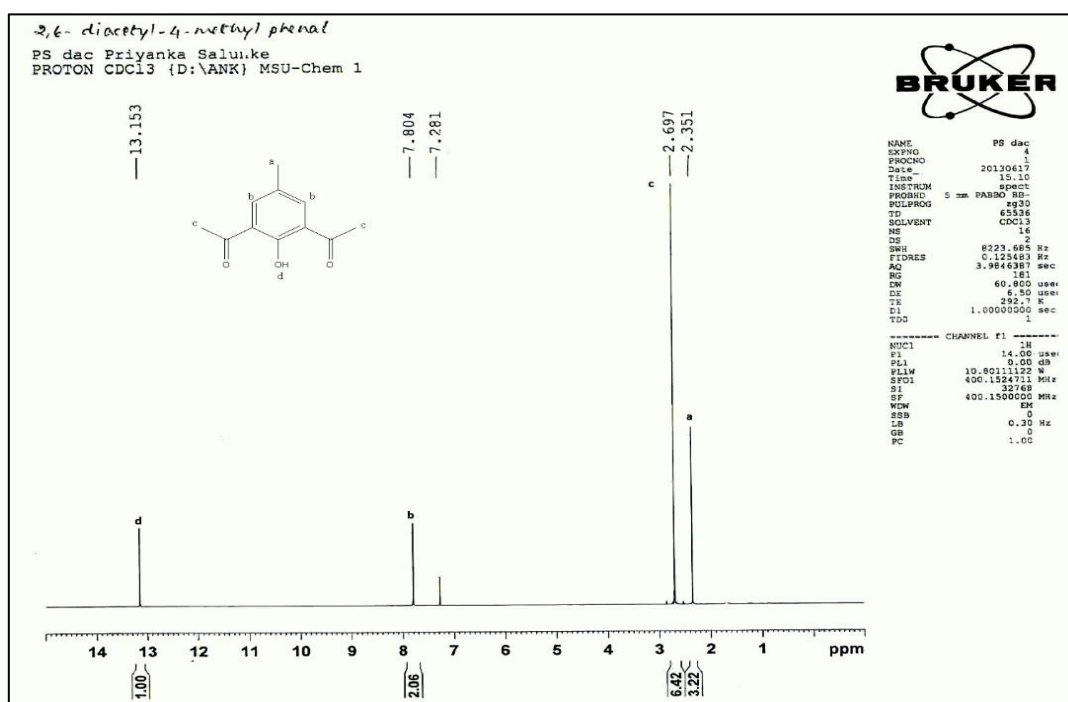
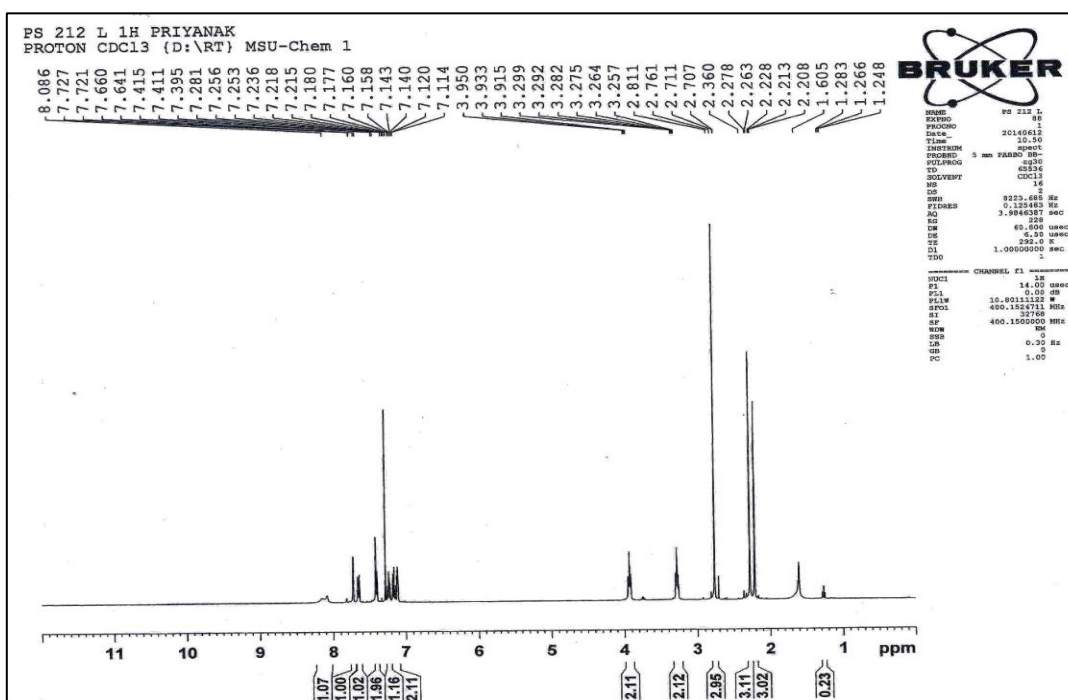
Mechanism explained in **section 2.3.5** in chapter 2 (**Figure 2.3.5**).

It can be seen from the table that the values of activation energy for the oxidation of 4-MC by **C5** and **C7** as catalysts are the lowest and they are lower than those for the oxidation of 3,5-DTBC. While **C6**, **C8**, having more hydrophobic groups have the lowest activation energy for the oxidation of 3,5-DTBC. This indicates that the selectivity of each complex towards a substrate changes with change in the structure of the complex.

3.4 CONCLUSION

- Synthesis and characterization of five new dicopper(II) complexes (**C4-C8**) has been carried out.
- Complex **C4** and **C6** crystallize in *P-1* point group.
- The kinetics of catecholase and ascorbate acid oxidase type activity of these dicopper(II) complexes with 3,5-DTBC & 4-methyl catechol and Ascorbic acid has been studied by varying parameters like concentration of substrate and catalyst and temperature.
- Complex **C8** has significantly high ascorbic acid oxidase activity over other complexes. Ascorbic acid oxidase activity follows the order: **C8 > C5 > C6 > C4 > C7**.
- Complex **C6** has better catecholase type activity over other complexes with 3,5-DTBC as a substrate. The activity of the complexes for oxidation of 3,5-DTBC follows the order: **C6 > C8 > C4 > C5 > C7**. However, the activity of complexes for the oxidation of 4-methyl catechol follows the order: **C5 > C7 > C4 > C6 > C8** with **C5** being the most active. This points towards the selectivity of complexes towards substrates.
- SOD mimic activity of dicopper complexes has been studied. Complex **C5** has significantly high SOD mimic activity over other complexes. The SOD mimic activity, as indicated by IC_{50} values, follows the order: **C5 > C4 > C8 > C6 > C7**.

Supplementary Information

Fig. S3.1 ¹H NMR spectrum of dacFig. S3.2 ¹H NMR spectrum of L⁸

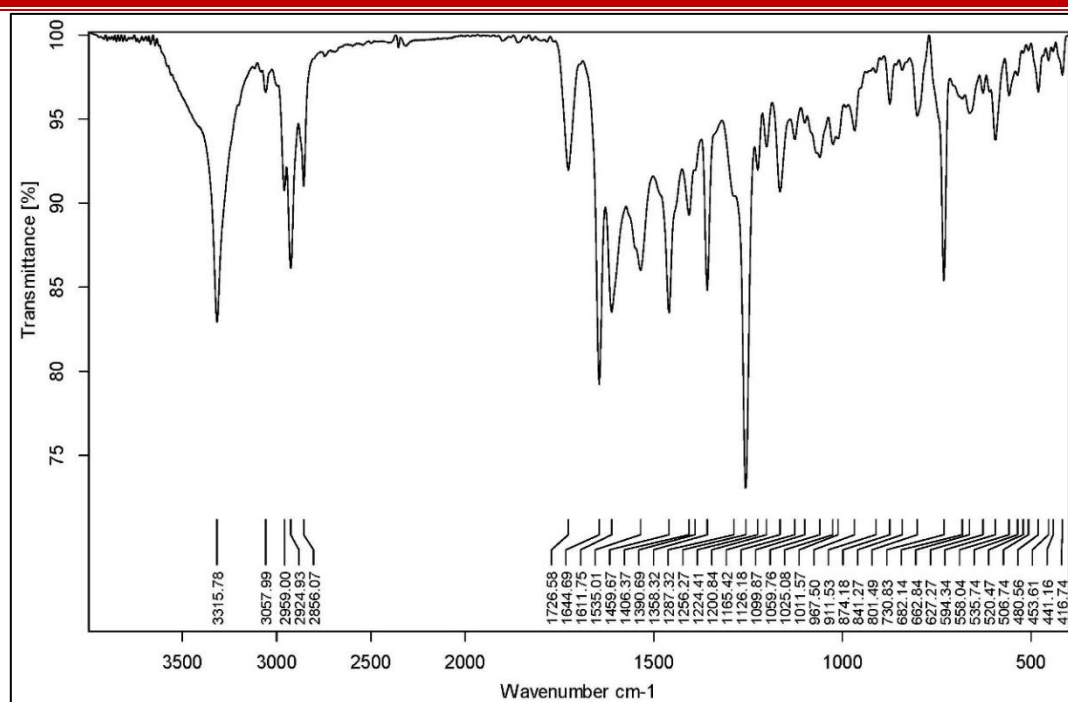


Fig. S3.3 IR spectrum of L^8

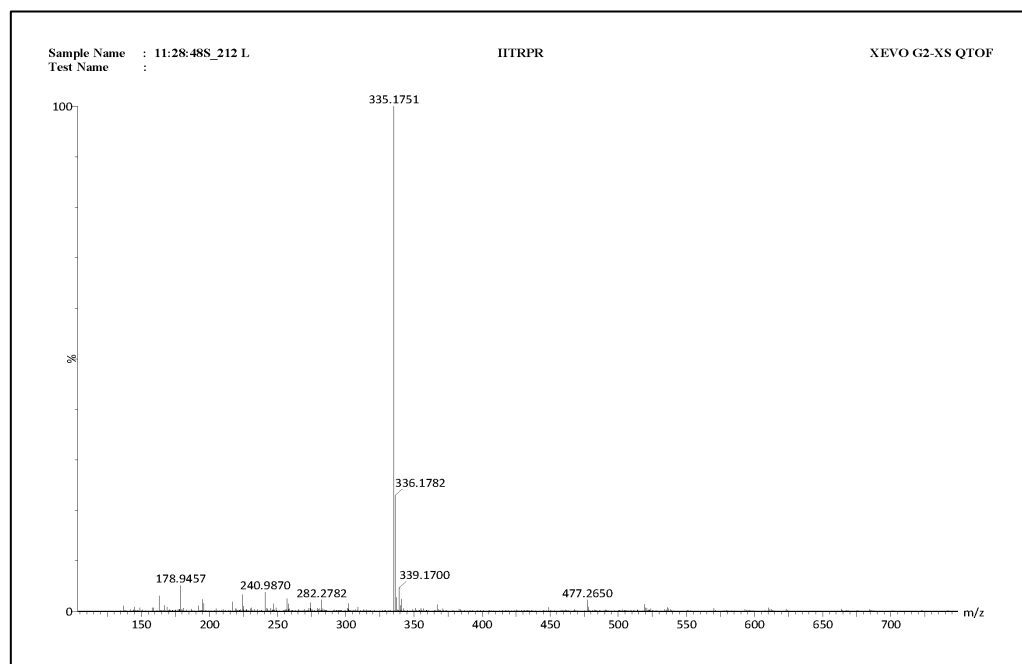


Fig. S3.4 Mass spectrum of L^8

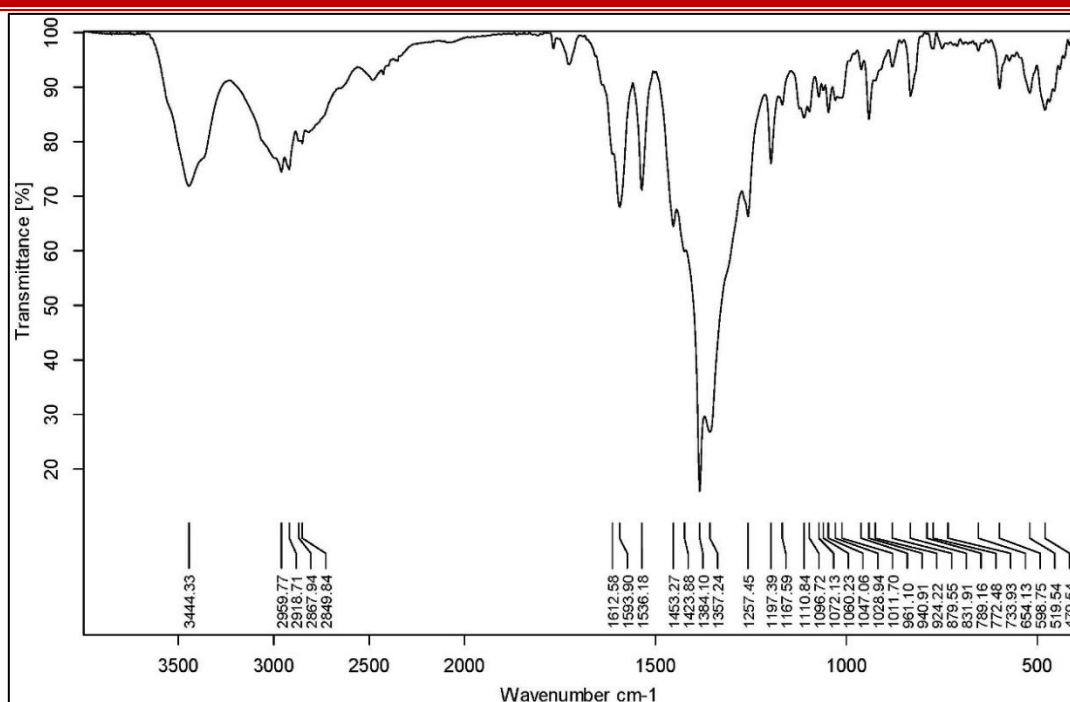


Fig. S3.5: IR spectrum of C4

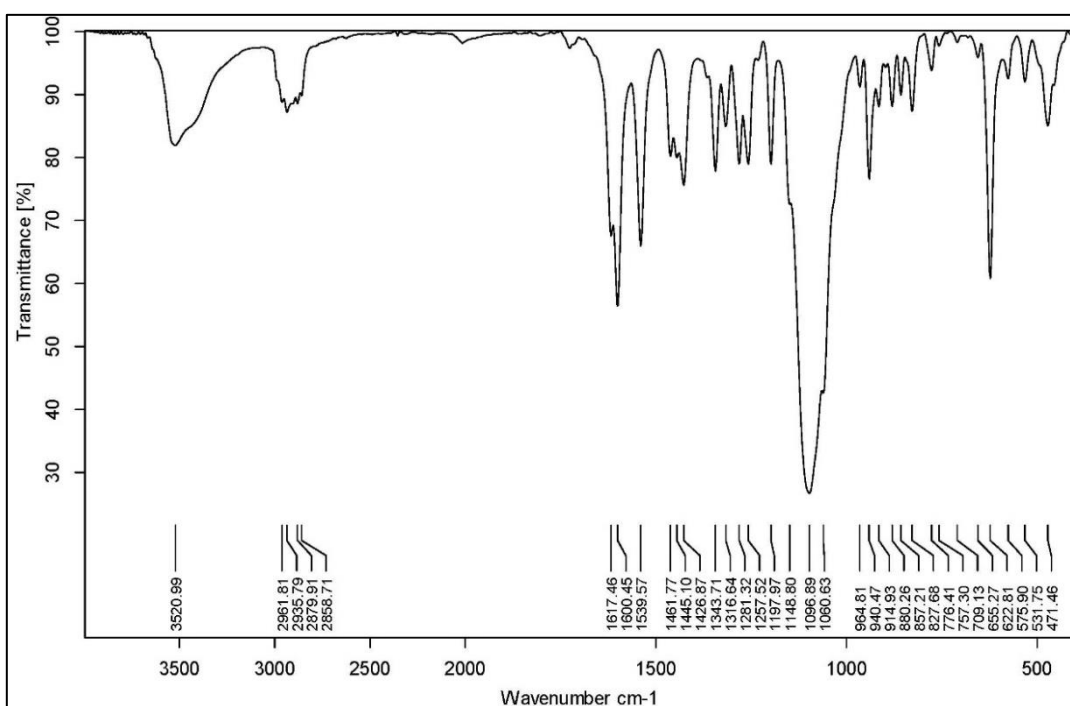


Fig. S3.6 IR spectrum of C5

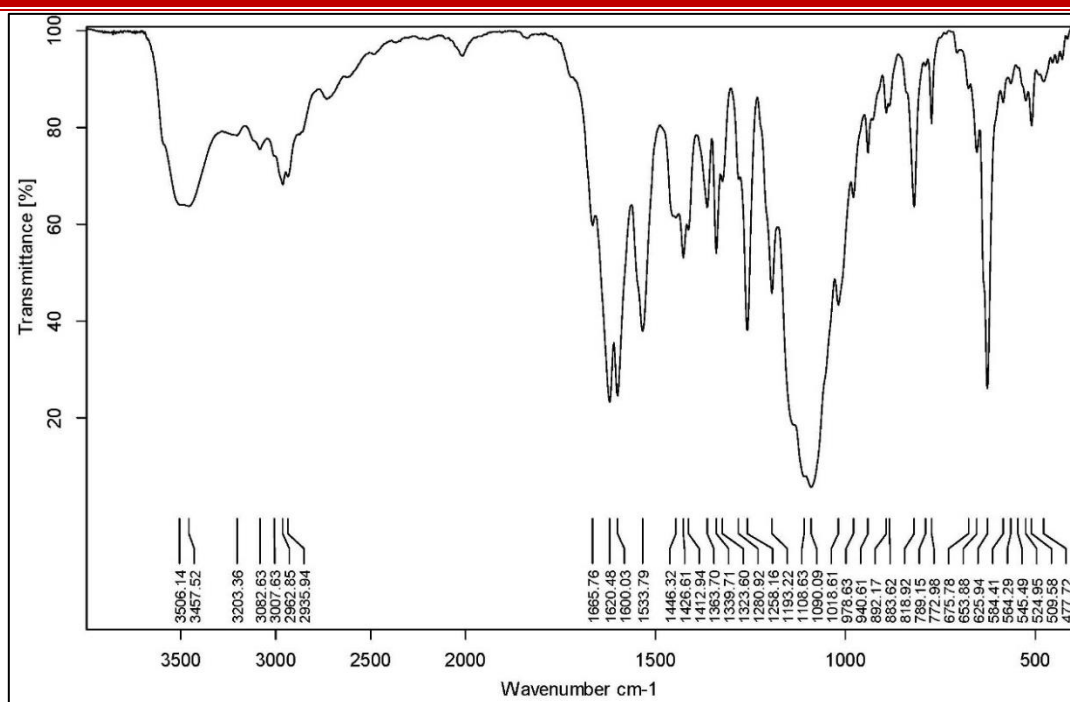


Fig. S3.7 IR spectrum of C6

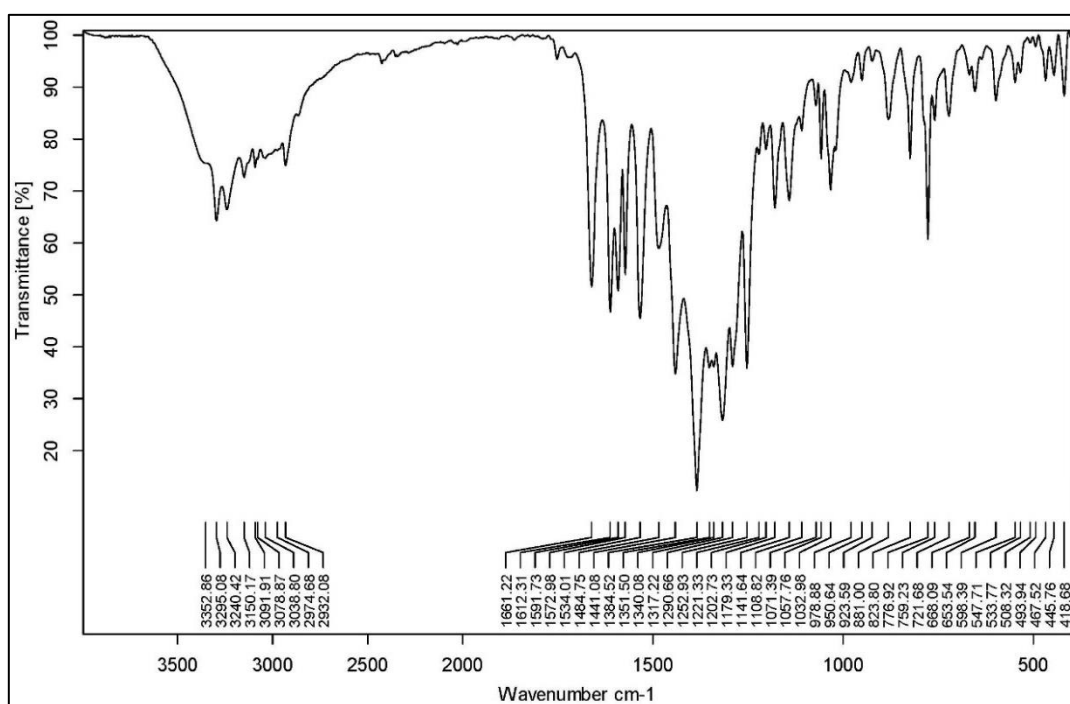


Fig. S3.8 IR spectrum of C7

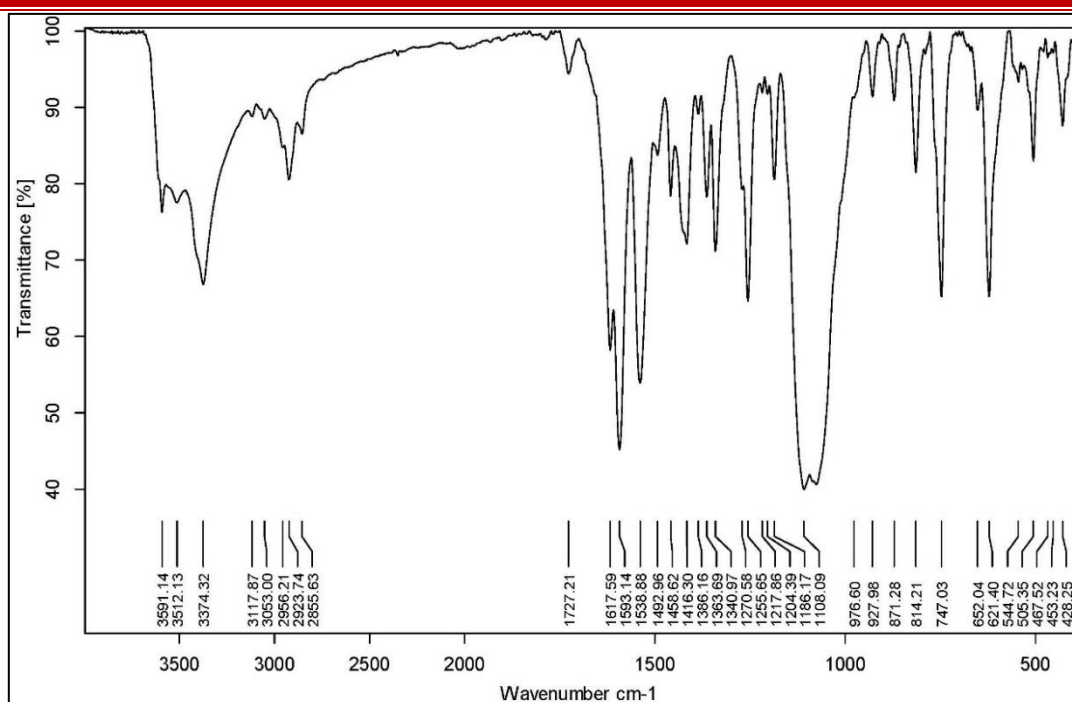


Fig. S3.9 IR spectrum of C8

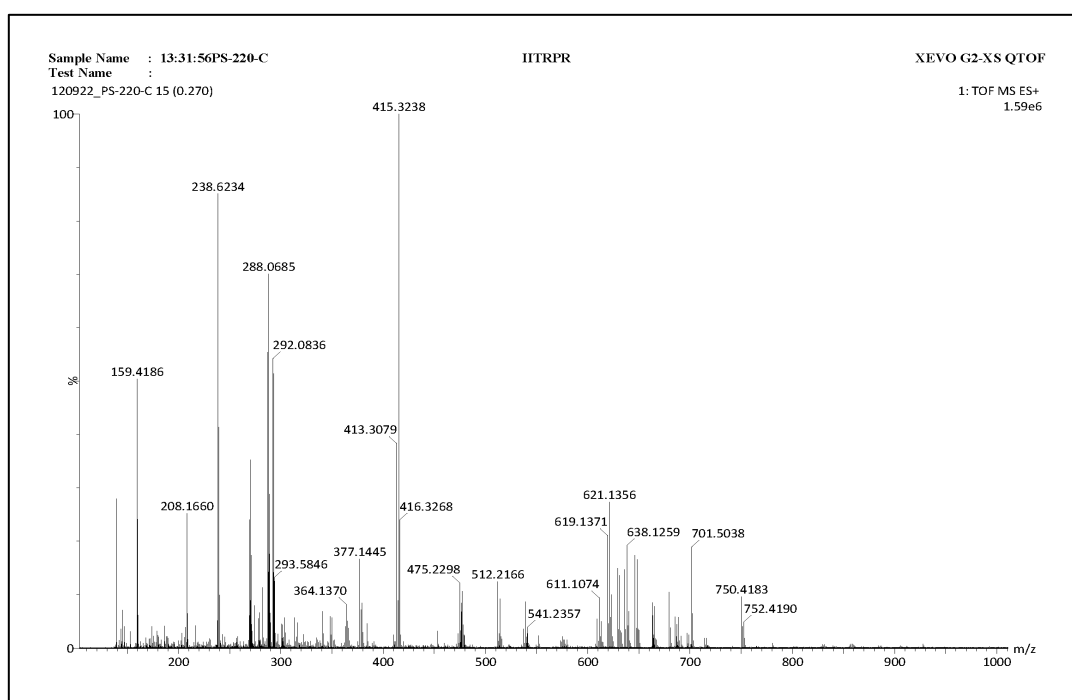


Fig. S3.10 Mass spectrum of C4

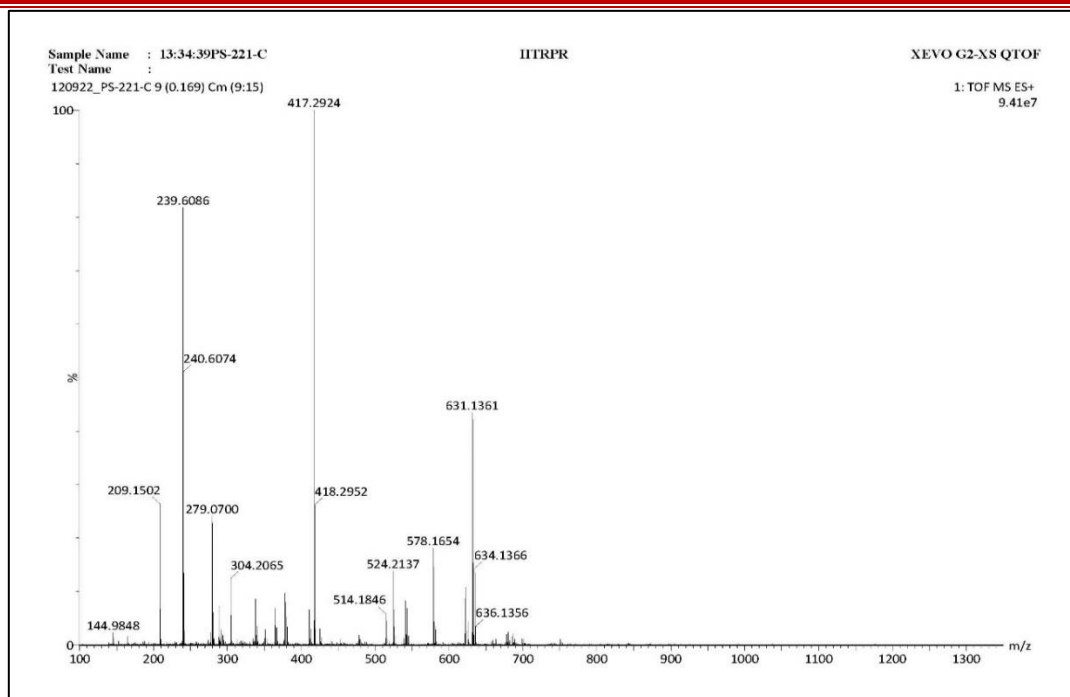


Fig. S3.11 Mass spectrum of C5

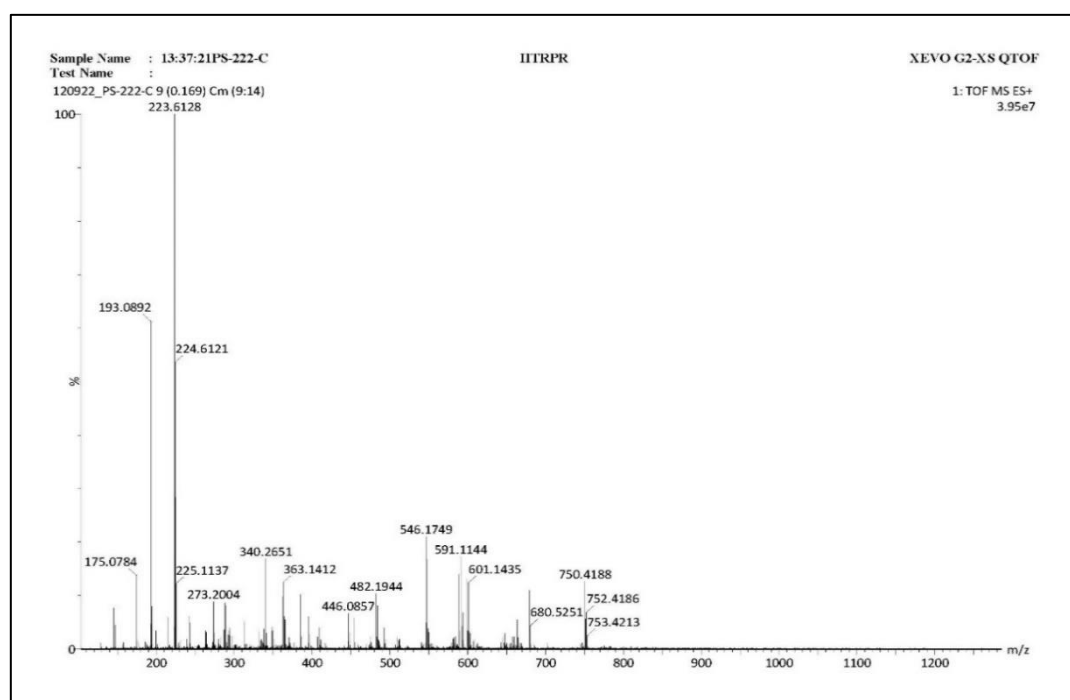


Fig. S3.12 Mass spectrum of C6

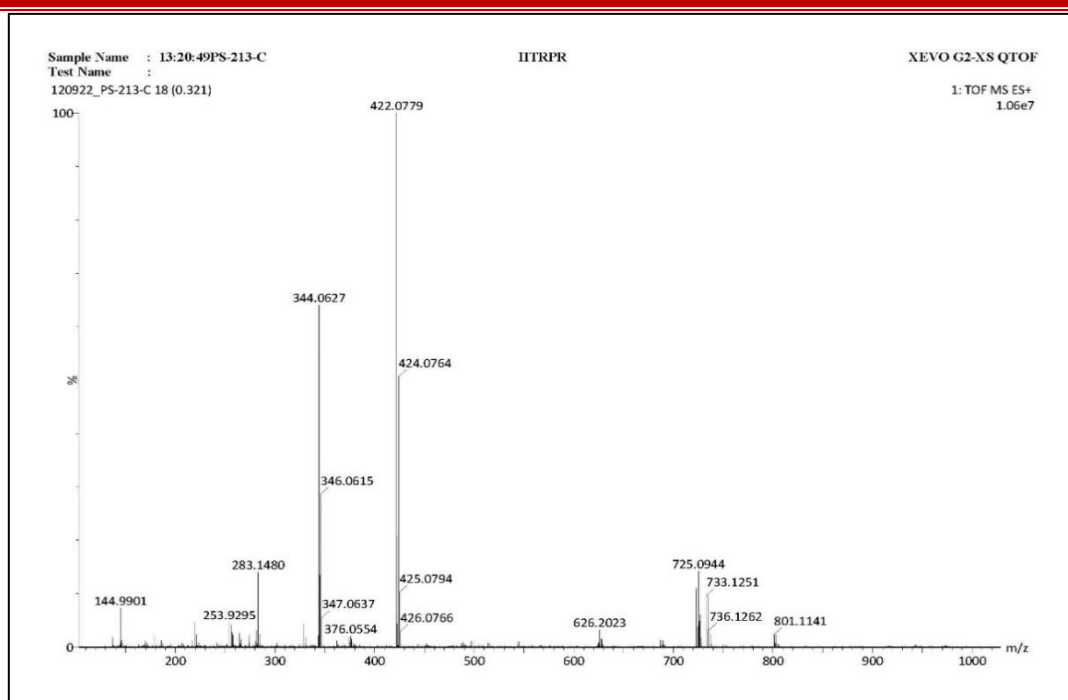


Fig. S3.13 Mass spectrum of C7

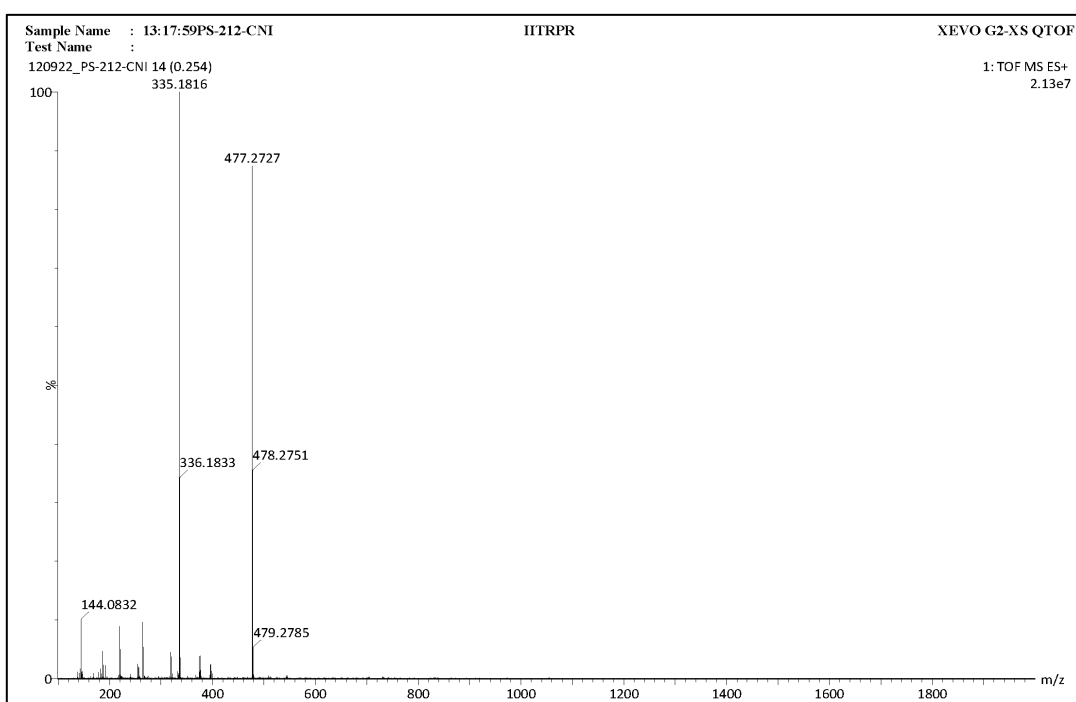


Fig. S3.14 Mass spectrum of C8

Table S3.1 Bond lengths, Bond angles and Torsional angles of C4

C4		
Cu-N Distances (Å°)		
R(4,1)	N4-Cu1	1.9631
R(11,1)	N11-Cu1	2.1821
R(6,2)	N6-Cu2	1.9598
R(5,2)	N5-Cu2	2.1646
Cu-O Distances (Å°)		
R(3,1)	O3-Cu1	2.0173
R(3,2)	O3-Cu2	2.006
R(74,1)	O74-Cu1	2.302
R(73,2)	O73-Cu2	2.3041
R(75,1)	O75-Cu1	1.9887
R(75,2)	O75-Cu2	1.9861
Bond angles		
A(4,1,11)	N4-Cu1-N11	87.6297
A(11,1,75)	N11-Cu1-O75	105.5313
A(4,1,3)	N4-Cu1-O3	90.6442
A(3,1,75)	O3-Cu1-O75	76.3258
A(3,2,75)	O3-Cu2-O75	76.6408
A(6,2,5)	N6-Cu2-O5	87.7188
A(5,52,75)	N5-Cu2-O75	104.644
A(6,2,3)	N6-Cu2-O3	90.9465
A(4,1,74)	N4-Cu1-O74	102.1256
A(6,2,73)	N6-Cu2-O73	101.3856
A(74,1,75)	O74-Cu1-O75	90.2505
A(73,2,3)	O73-Cu2-O3	94.7844
A(73,2,75)	O73-Cu2-O75	90.244
A(1,3,2)	Cu1-O3-Cu2	99.0578
A(1,75,2)	Cu1-O75-Cu2	100.7099
Torsional angles		
L(3,1,11,4,-1)	O3-Cu1-N11-N4 (-1)	178.2739
L(3,2,5,6,-1)	O3-Cu2-N5-N6 (-1)	178.6653
L(3,1,11,4,-2)	O3-Cu1-N11-N4 (-2)	179.165
L(3,2,5,6,-2)	O3-Cu2-N5-N6 (-2)	179.8551

Table S3.1 (Contd..) Bond lengths, Bond angles of C5

C5		
Cu-N Distances (Å^o)		
R(4,1)	N4-Cu1	1.9602
R(8,1)	N8-Cu1	2.0505
R(5,2)	N5-Cu2	2.0511
R(6,2)	N6-Cu2	1.9608
Cu-O Distances (Å^o)		
R(3,1)	O3-Cu1	2.0312
R(69,1)	O69-Cu1	2.2595
R(70,1)	O70-Cu1	1.9241
R(3,2)	O3-Cu2	2.0325
R(68,2)	O68-Cu2	2.2576
R(70,2)	O70-Cu2	1.9243
Bond angles		
A(3,1,4)	O3-Cu1-N4	89.6447
A(3,1,69)	O3-Cu1-O69	91.2921
A(3,1,70)	O3-Cu1-O70	79.0502
A(4,1,8)	N4-Cu1-N8	90.4578
A(4,1,69)	N5-Cu1-O69	86.9725
A(8,1,69)	N8-Cu1-O69	95.56
A(8,1,70)	N8-Cu1-O70	99.7693
A(3,2,6)	O3-Cu2-N6	89.574
A(3,2,68)	O3-Cu2-O68	91.3315
A(3,2,70)	O3-Cu2-O70	79.0137
A(5,2,6)	N5-Cu2-N6	90.4206
A(5,2,68)	N5-Cu2-O68	95.6206
A(5,2,70)	N5-Cu2-O70	99.8779
A(6,2,68)	N6-Cu2-O68	87.1215

Table S3.1 (Contd..) Bond lengths, Bond angles of C6

C6		
Cu-N Distances (Å°)		
R(9,1)	N9-Cu1	2.0363
R(11,1)	N11-Cu1	1.9663
R(8,2)	N8-Cu2	1.9665
R(12,2)	N12-Cu2	2.0378
Cu-O Distances (Å°)		
R(4,1)	O4-Cu1	2.0431
R(5,1)	O5-Cu1	1.8897
R(10,1)	O10-Cu1	2.2665
R(4,2)	O4-Cu2	2.0454
R(5,2)	O5-Cu2	1.8903
R(7,2)	O7-Cu2	2.2606
Bond angles		
A(4,1,5)	O4-Cu1-O5	77.8108
A(4,1,10)	O4-Cu1-O10	90.9535
A(4,1,11)	O4-Cu1-N11	89.2216
A(5,1,9)	O5-Cu1-N9	101.7069
A(5,1,10)	O5-Cu1-O10	98.9021
A(9,1,10)	N9-Cu1-O10	99.5017
A(9,1,11)	N9-Cu1-N11	89.9458
A(10,1,11)	O10-Cu1-N11	87.0906
A(4,2,5)	O4-Cu2-O5	77.7398
A(4,2,7)	O4-Cu2-O7	91.1593
A(4,2,8)	O4-Cu2-N8	89.1847
A(4,2,75)	O4-Cu2-O75	120.5638
A(5,2,7)	O5-Cu2-O7	99.1115
A(5,2,12)	O5-Cu2-N12	101.64
A(5,2,75)	O5-Cu2-O75	54.6605
A(7,2,8)	O7-Cu2-N8	87.8194
A(7,2,12)	O7-Cu2-N12	99.4506
A(7,2,75)	O7-Cu2-O75	126.31
A(8,2,12)	N8-Cu2-N12	89.9322
A(8,2,75)	N8-Cu2-O75	130.1601
A(12,2,75)	N12-Cu2-O75	53.3492

Table S3.1 (Contd..) Bond lengths, Bond angles and Torsional angles of C7

<i>C7</i>		
Cu-N Distances (Å°)		
R(27,52)	N27-Cu52	2.0435
R(37,53)	N37-Cu53	2.0437
R(46,52)	N46-Cu52	1.9988
R(47,53)	N47-Cu53	1.9995
Cu-O Distances (Å°)		
R(45,52)	O45-Cu52	1.9973
R(45,53)	O45-Cu53	1.9979
R(55,52)	O55-Cu52	1.96
R(67,52)	O67-Cu52	2.2408
R(56,53)	O56-Cu53	2.2407
R(61,53)	O61-Cu53	1.9603
Bond angles		
A(27,52,46)	N27-Cu52-N46	82.5497
A(27,52,55)	N27-Cu52-O55	91.1569
A(27,52,67)	N27-Cu52-O67	91.7251
A(45,52,46)	O45-Cu52-N46	88.181
A(45,52,55)	O45-Cu52-O55	97.2361
A(45,52,67)	O45-Cu52-O67	90.2662
A(46,52,67)	N46-Cu52-O67	87.2647
A(55,52,67)	O55-Cu52-O67	106.8873
A(37,53,47)	N37-Cu53-N47	82.5497
A(37,53,56)	N37-Cu53-O56	91.7973
A(37,53,61)	N37-Cu53-O61	91.1503
A(45,53,47)	O45-Cu53-N47	88.1264
A(45,53,56)	O45-Cu53-O56	90.1463
A(45,53,61)	O45-Cu53-O61	97.3027
A(47,53,56)	N47-Cu53-O56	87.2893
A(56,53,61)	O56-Cu53-O61	106.9306
Torsional angles		
L(37,53,45,47,-1)	N37-Cu53-O45-N47 (-1)	170.6761
L(37,53,45,47,-2)	N37-Cu53-O45-N47(-2)	177.5952

Table S3.1 (Contd..) Bond lengths, Bond angles and Torsional angles of C8

C8		
Cu-N Distances (Å°)		
R(39,51)	N39-Cu51	1.971
R(12,52)	N12-Cu52	1.9754
Cu-O Distances (Å°)		
R(14,51)	O14-Cu51	1.9757
R(9,51)	O9-Cu51	2.0107
R(42,51)	O42-Cu51	1.9829
R(96,51)	O96-Cu51	2.3806
R(103,51)	O103-Cu51	2.2717
R(37,52)	O37-Cu51	1.9794
R(9,52)	O9-Cu52	1.9864
R(42,52)	O42-Cu52	2.0125
R(97,52)	O97-Cu52	2.2964
R(101,52)	O101-Cu52	2.4205
Bond angles		
A(9,51,14)	O9-Cu51-C14	87.2145
A(9,51,42)	O9-Cu51-O42	81.1729
A(9,51,96)	O9-Cu51-O96	84.2023
A(9,51,103)	O9-Cu51-O103	92.5461
A(14,51,39)	O14-Cu51-N39	100.7306
A(14,51,96)	O14-Cu51-O96	83.6469
A(14,51,103)	O14-Cu51-O103	94.8526
A(39,51,42)	N39-Cu1-O42	90.5738
A(39,51,96)	N39-Cu51-O96	89.8896
A(39,51,103)	N39-Cu51-O103	93.5294
A(42,51,96)	O42-Cu51-O96	93.145
A(42,51,103)	O42-Cu51-O103	87.6915
A(9,52,12)	O9-Cu52-N12	91.3866
A(9,52,42)	O9-Cu52-O42	81.0437
A(9,52,97)	O9-Cu52-O97	86.4972
A(9,52,101)	O9-Cu52-O101	89.9426
A(12,52,37)	N12-Cu52-O37	100.9889
A(12,52,97)	N12-Cu52-O97	92.8985
A(12,52,101)	N12-Cu52-O101	93.4589
A(37,52,42)	O37-Cu52-O42	86.3536

A(37,52,97)	O37-Cu52-O97	96.4251
A(37,52,101)	O37-Cu52-O101	85.7045
A(42,52,97)	O42-Cu52-O97	90.4523
A(42,52,101)	O42-Cu52-O101	82.790
Torsional angles		
L(9,51,39,14,-1)	O9-Cu51-N39-O14 (-1)	187.9451
L(14,51,42,9,-1)	O14-Cu51-O42-O9(-1)	168.384
L(96,51,103,9,-1)	O96-Cu51-O103-O9 (-1)	176.7484
L(9,52,37,12,-1)	O9-Cu52-O37-O42-O9 (-1)	192.3755
L(12,52,42,9,-1)	N12-Cu52-O42-O9 (-1)	172.4304
L(97,52,101,9,-1)	O97-Cu52-O101-O9 (-1)	176.4398
L(9,51,39,14,-2)	O9-Cu51-N39-O14 (-2)	173.1492
L(14,51,42,9,-2)	O14-Cu51-O42-O9(-2)	182.0043
L(96,51,103,9,-2)	O96-Cu51-O103-O9 (-2)	178.6301
L(9,52,37,12,-2)	O9-Cu52-O37-O42-O9 (-2)	176.3166
L(12,52,42,9,-2)	N12-Cu52-O42-O9 (-2)	183.8313
L(97,52,101,9,-2)	O97-Cu52-O101-O9 (-2)	173.7217

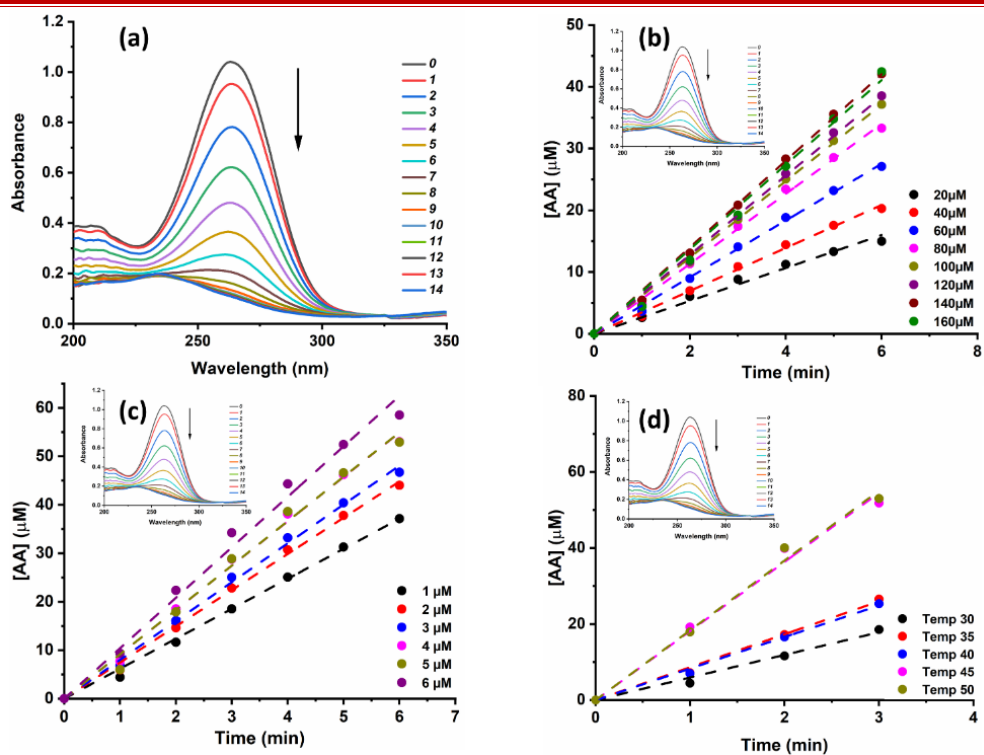


Fig. S3.15A Time dependent spectral changes in AA corresponding to (a) C5 catalyzed oxidation and Plot of [AA] as function of time with respect to (b) Substrate (c) Catalyst (d) temperature of C5 (Inset: Plot of absorbance vs wavelength at different time intervals) (Contd...)

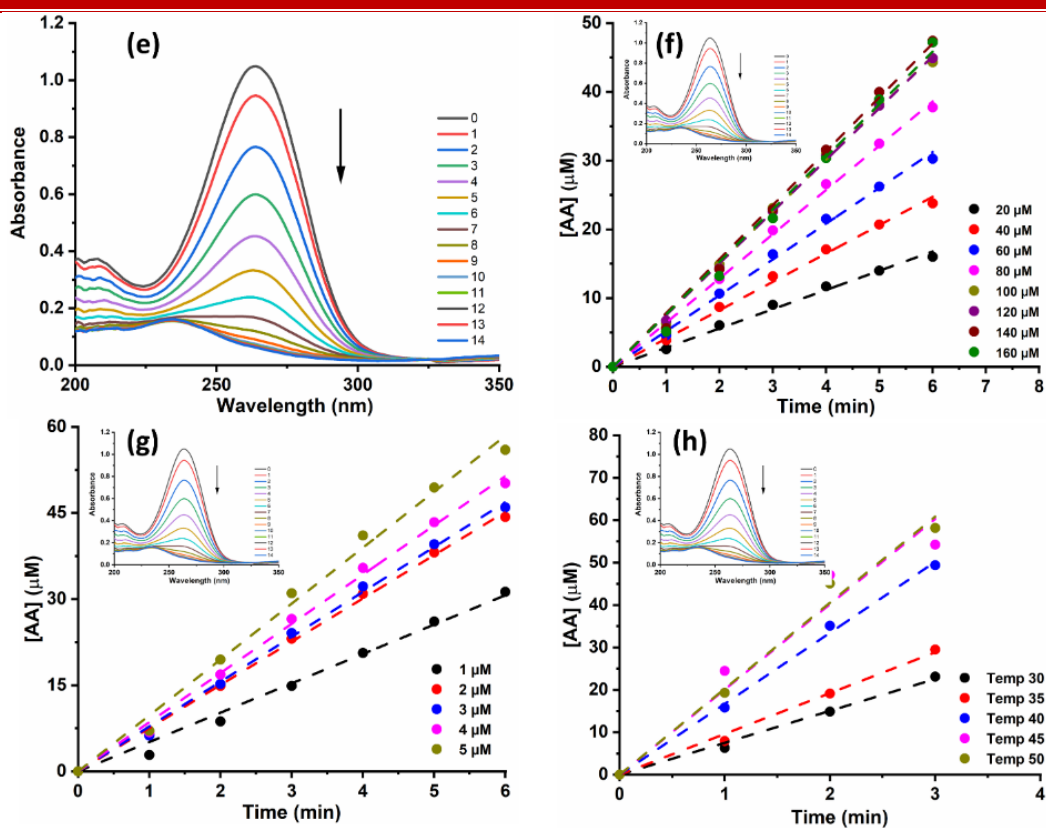


Fig. S3.15B (Contd...) Time dependent spectral changes inAA corresponding to (e) C6 and Plot of [AA] as function of time with respect to (f) Substrate (g) Catalyst (h) temperature of C6, (Inset: Plot of absorbance vs wavelength at different time intervals)

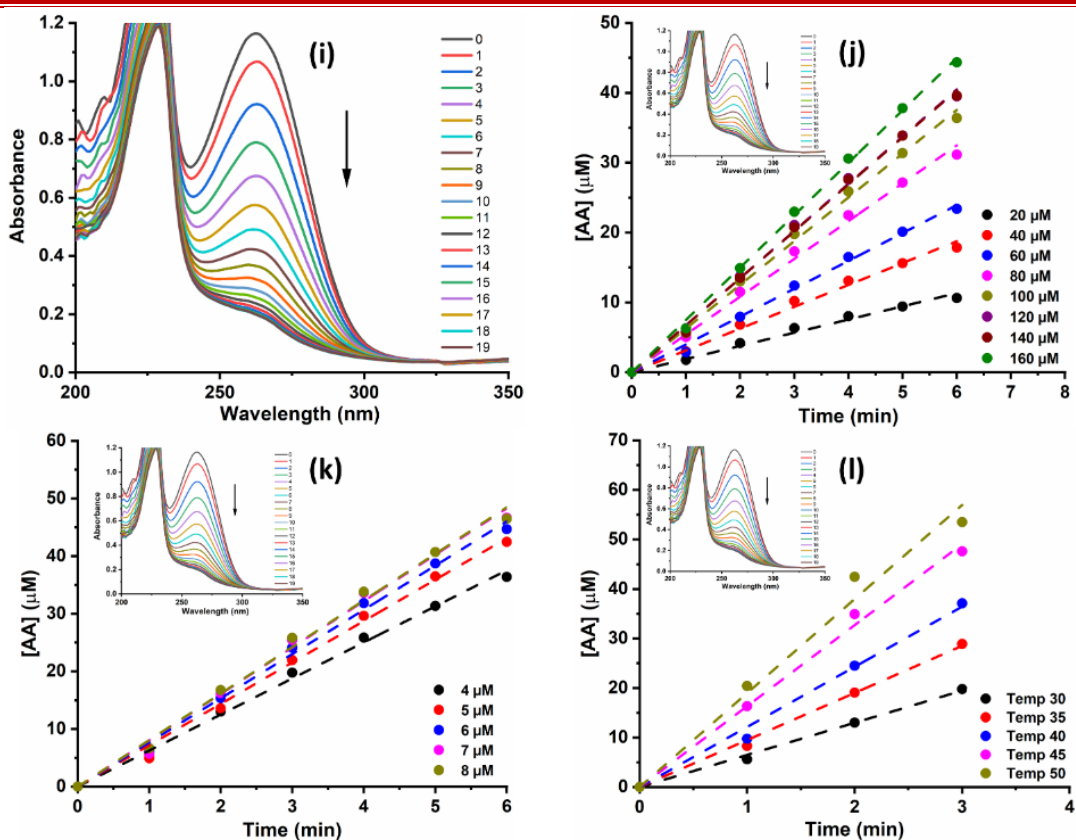


Fig. S3.15C (Contd...) Time dependent spectral changes in AA corresponding to (i) C7 catalyzed oxidation and Plot of [AA] as function of time with respect to (j) Substrate (k) Catalyst (l) temperature of C7, (Inset: Plot of absorbance vs wavelength at different time intervals)

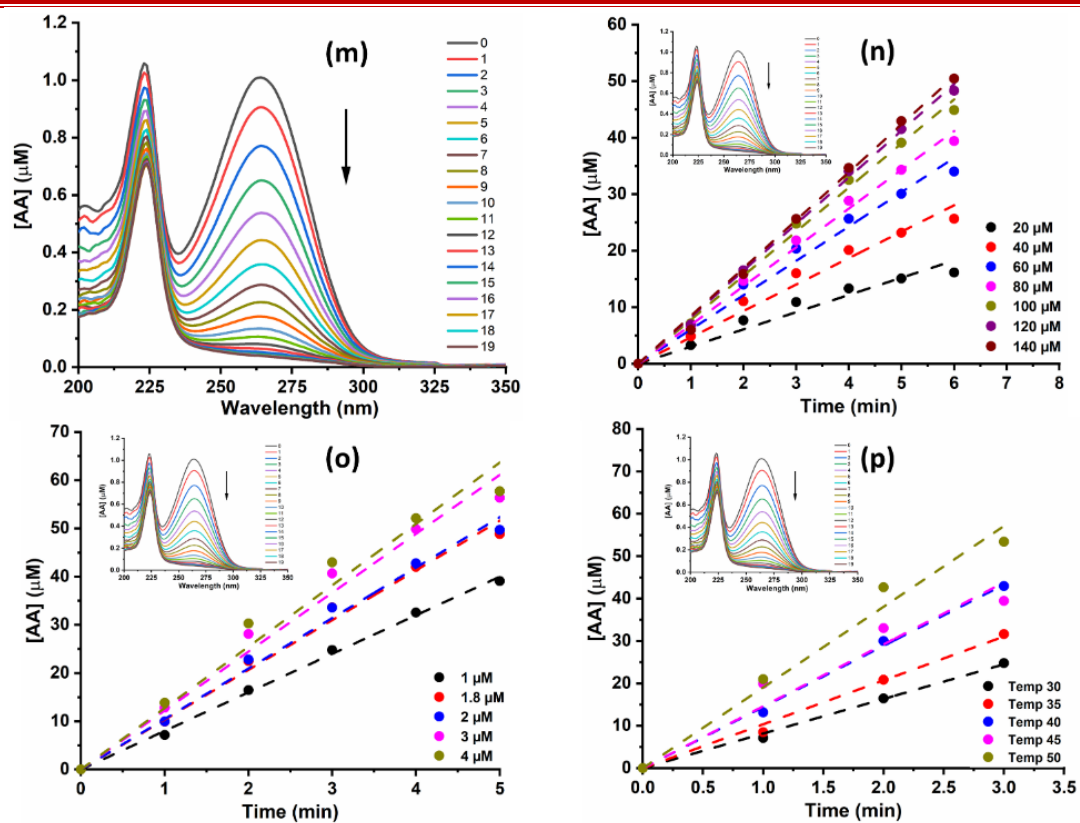


Fig. S3.15D (Contd...) Time dependent spectral changes of AA corresponding to (m) C8 catalyzed oxidation and Plot of [AA] as function of time with respect to (n) Substrate (o) Catalyst (p) temperature of C8 (Inset: Plot of absorbance vs wavelength at different time intervals)

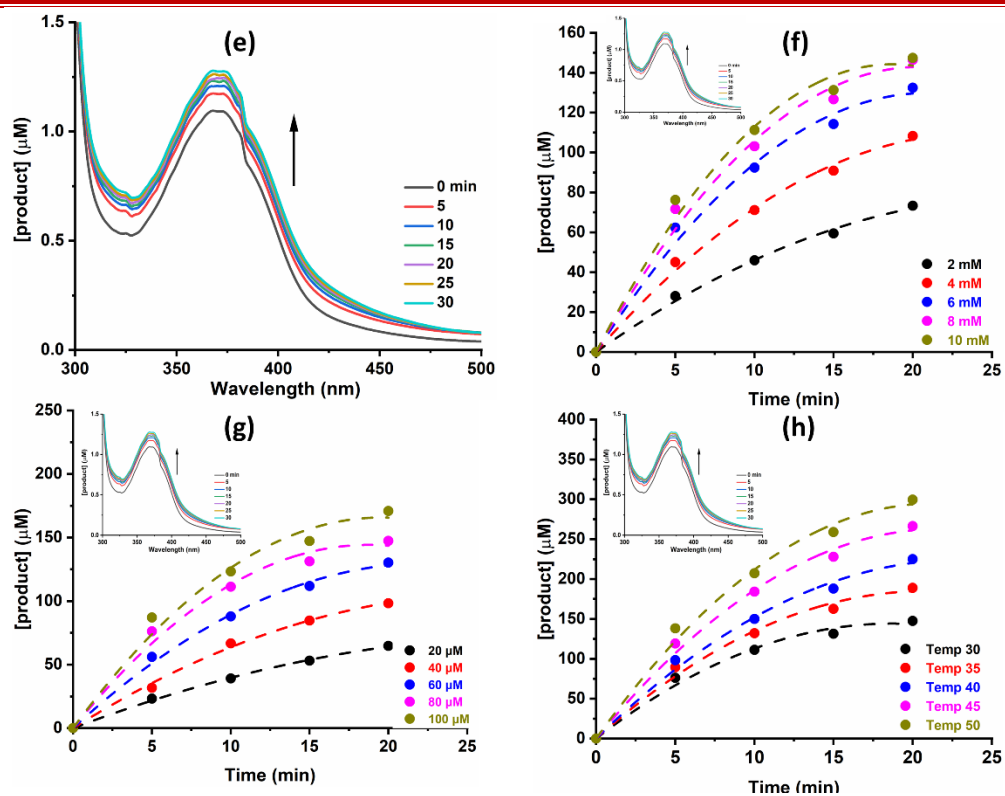


Fig S3.16 (e) Time dependent spectral changes over time period of 0-20 min in 4-MC corresponding to C5 catalyzed oxidation and (f-h) Plot of [product] as function of time with respect to substrate (f), catalyst (g) and temperature (h) (Inset: Plot of absorbance vs wavelength at different time interval) for complex C5 with 4-MC

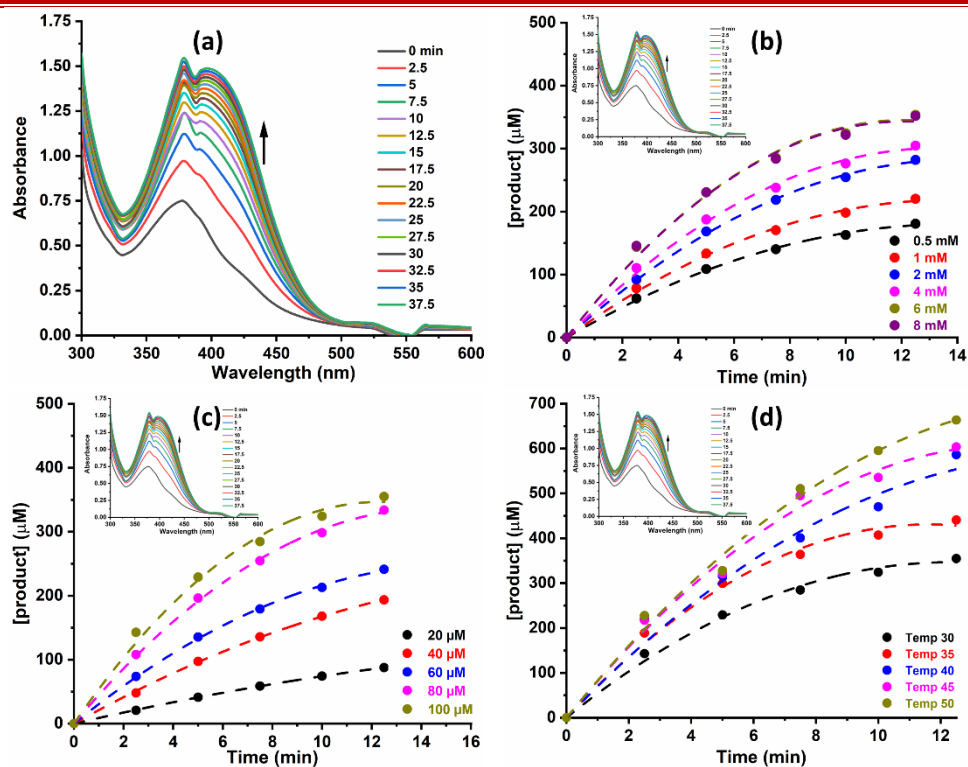


Fig S3.17A (a) Time dependent spectral changes over time period of 0-15min in 3,5-DTBC corresponding to C4 catalyzed oxidation and (b-d) Plot of [product] as function of time with respect to substrate (b), catalyst (c) and temperature (d) (Inset: Plot of absorbance vs wavelength at different time interval) for complex C4 with 3,5-DTBC

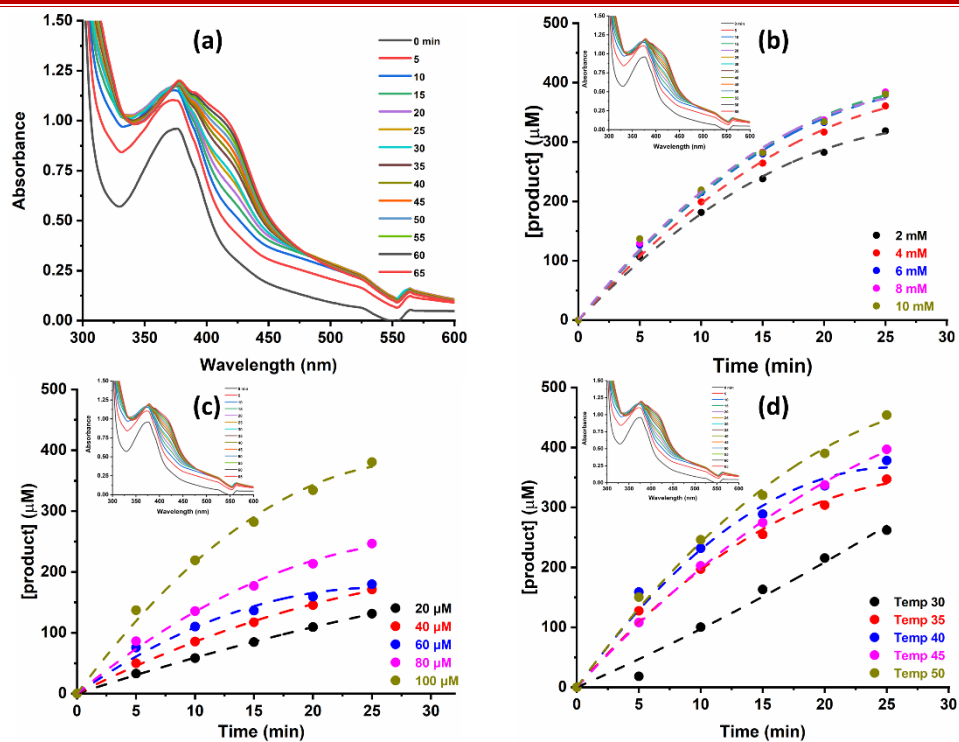


Fig S3.17B (a) Time dependent spectral changes over a time period of 0-25min in 4-MC corresponding to **C4** catalyzed oxidation and (b-d) Plot of [product] as function of time with respect to substrate (b), catalyst (c) and temperature (d) (Inset: Plot of absorbance vs wavelength at different time interval) for complex **C4** with 4-MC

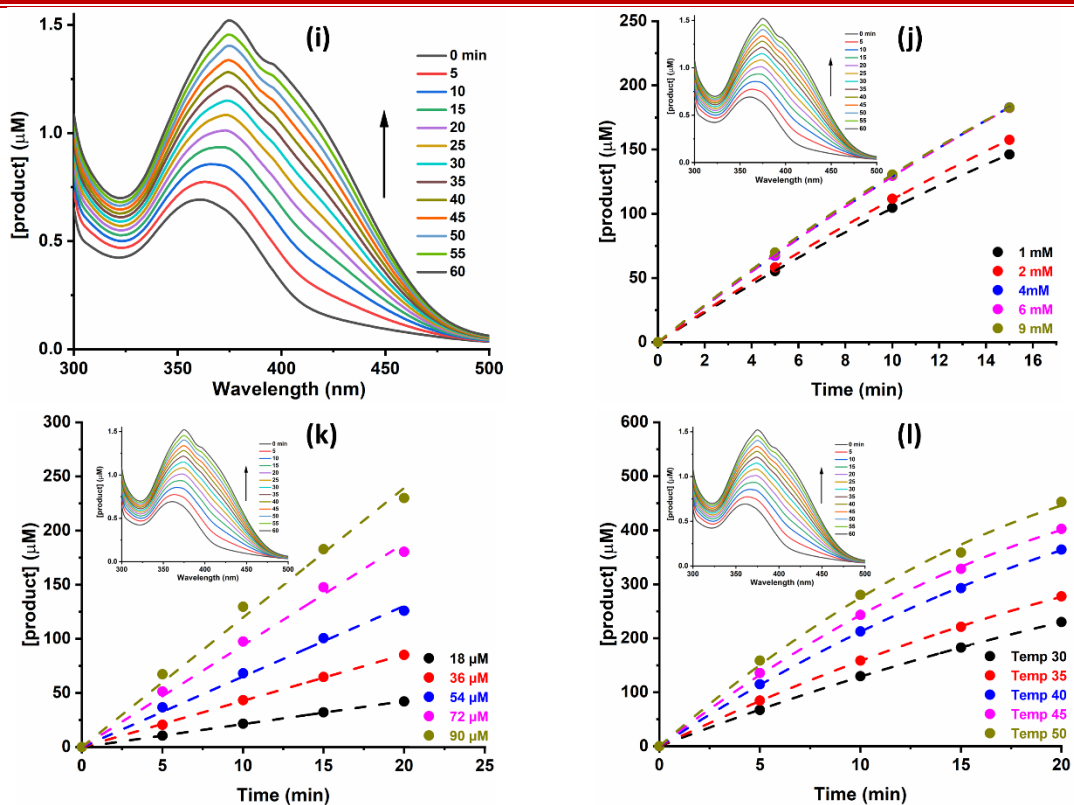


Fig S3.18A (i) Time dependent spectral changes over a time period of 0-20 min in 3,5-DTBC corresponding to C6 catalyzed oxidation and (j-l) Plot of [product] as function of time with respect to substrate (j), catalyst (k) and temperature (l) (Inset: Plot of absorbance vs wavelength at different time interval) for complex C6 with 3,5-DTBC

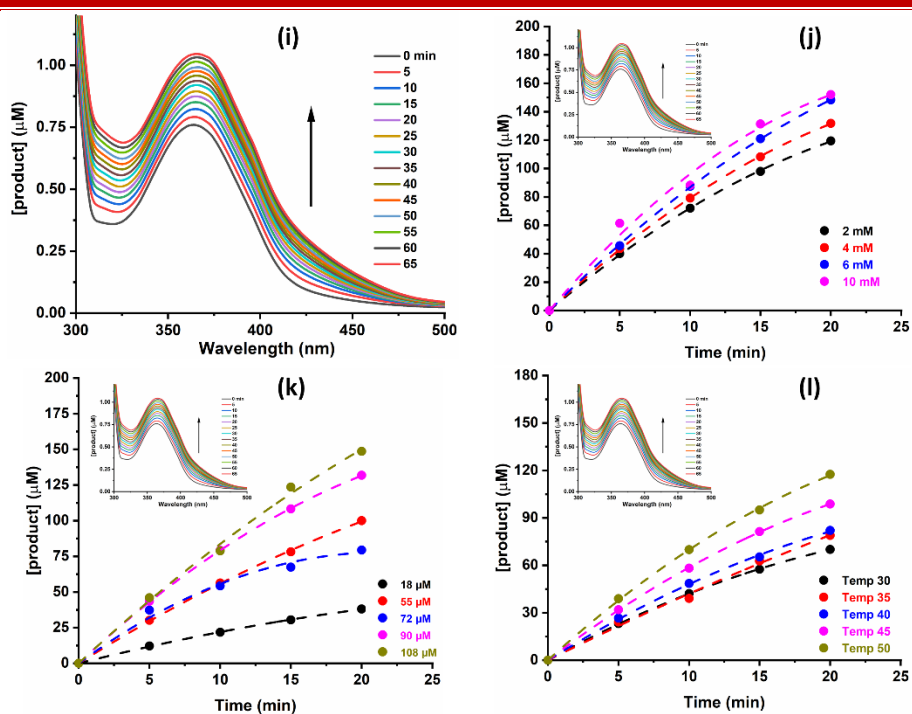


Fig S3.18B (i) Time dependent spectral changes over a time period of 0-20 min in 4-MC corresponding to **C6** catalyzed oxidation and (j-l) Plot of [product] as function of time with respect to substrate (j), catalyst (k) and temperature (l) (Inset: Plot of absorbance vs wavelength at different time interval) for complex **C6** with 4-MC

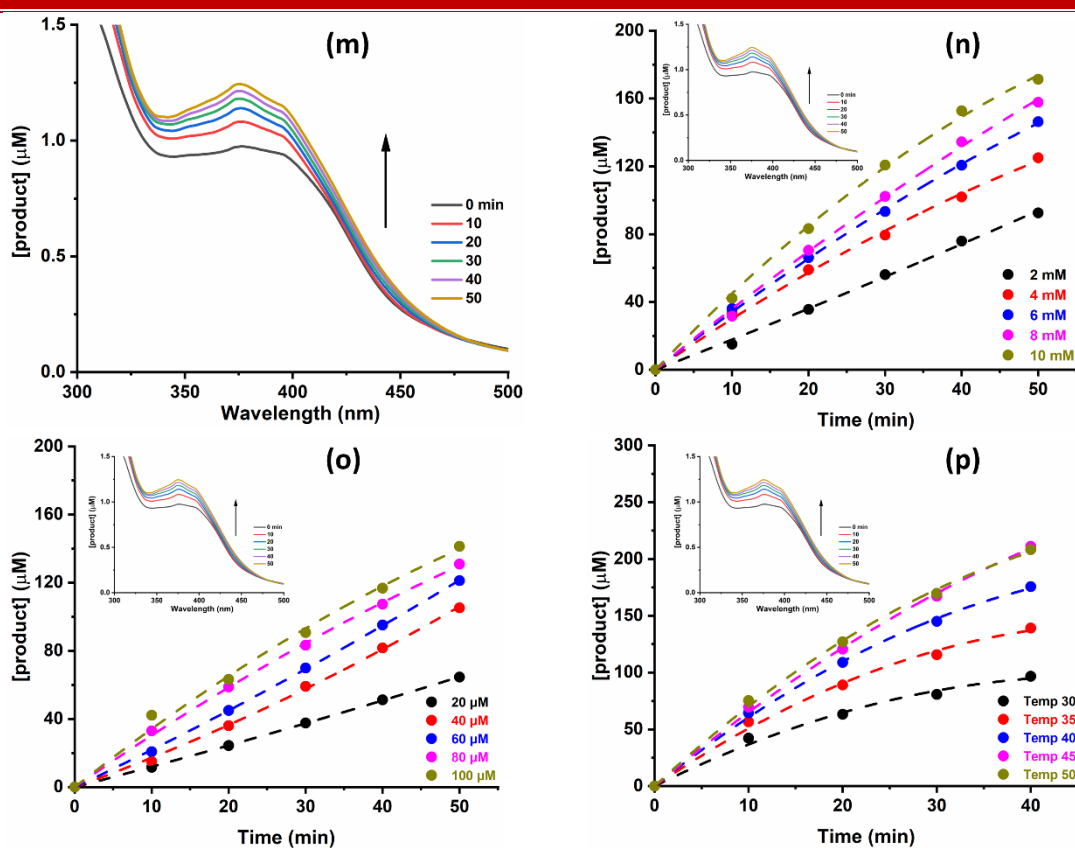


Fig S3.19A (m) Time dependent spectral changes over a time period of 0-40 min in 3,5-DTBC corresponding to C7 catalyzed oxidation and (n-p) Plot of [product] as function of time with respect to substrate (n), catalyst (o) and temperature (p) (Inset: Plot of absorbance vs wavelength at different time interval) for complex C7 with 3,5-DTBC

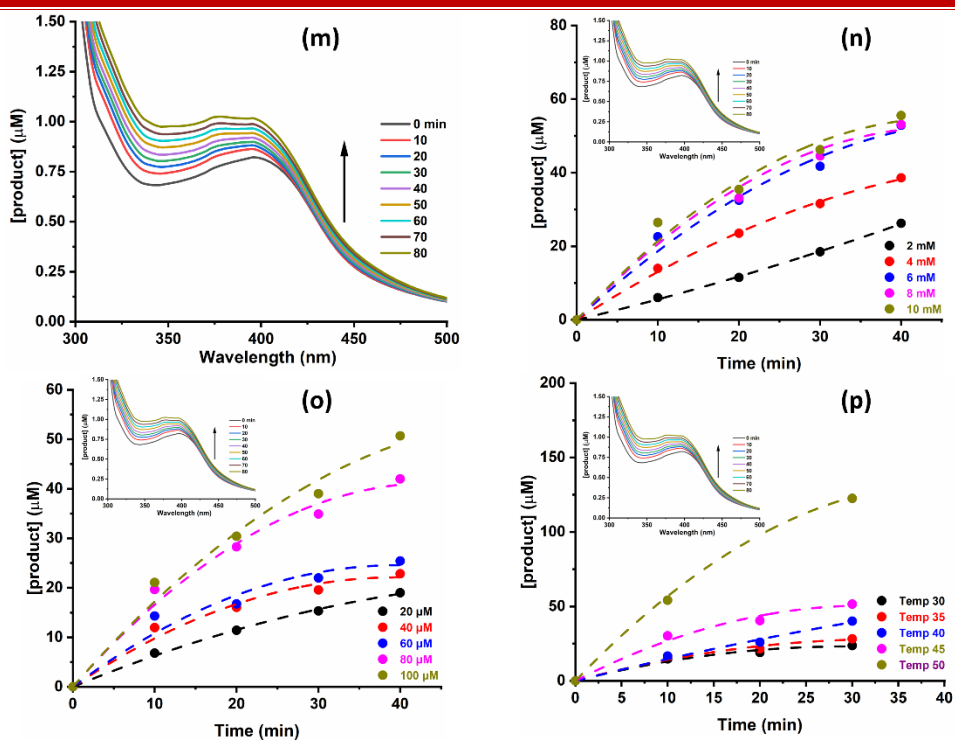


Fig S3.19B (m) Time dependent spectral changes over a time period of 0-30 min in 4-MC corresponding to C7 catalyzed oxidation and (n-p) Plot of [product] as function of time with respect to substrate (n), catalyst (o) and temperature (p) (Inset: Plot of absorbance vs wavelength at different time interval) for complex C7 with 4-MC

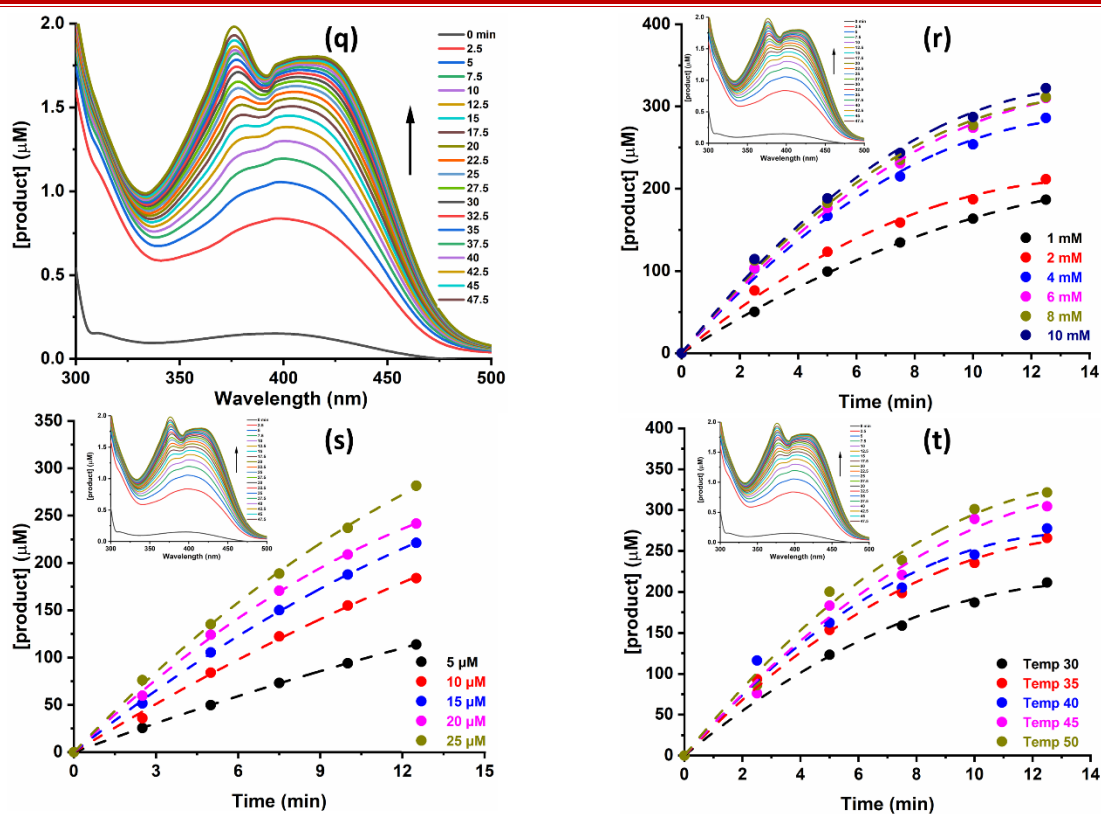


Fig S3.20A (a) Time dependent spectral changes over a time period of 0-15 min in 3,5-DTBC corresponding to C8 catalyzed oxidation and (b-d) Plot of [product] as function of time with respect to substrate (b), catalyst (c) and temperature (d) (Inset: Plot of absorbance vs wavelength at different time interval) for complex C8 with 3,5-DTBC

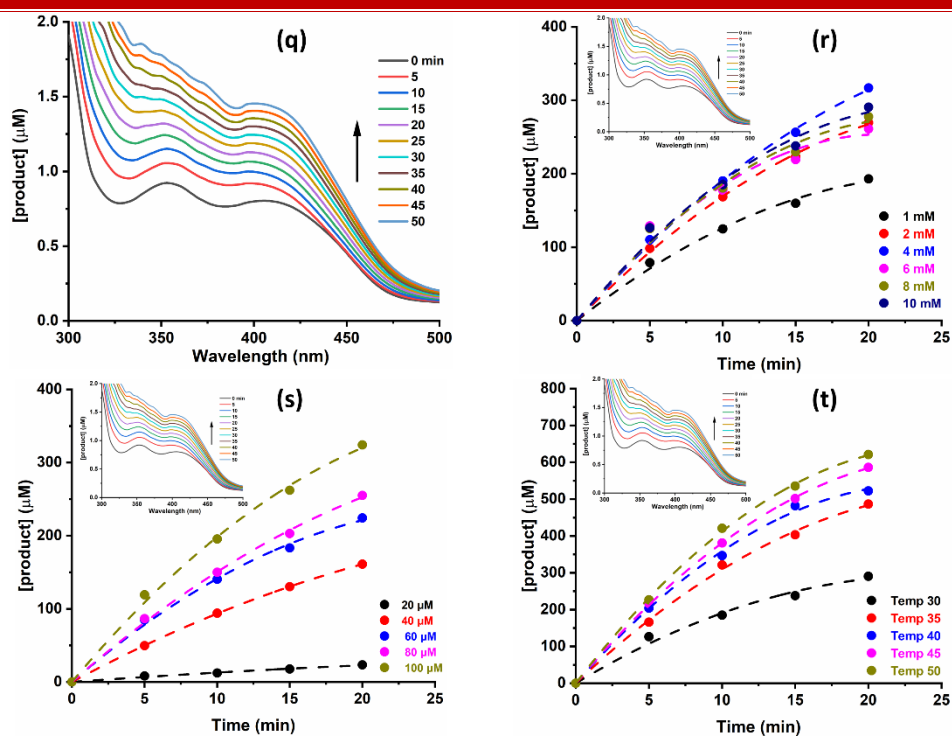


Fig S3.20B (a) Time dependent spectral changes over a time period of 0-20 min in 4-MC corresponding to C8 catalyzed oxidation and (b-d) Plot of [product] as function of time with respect to substrate (b), catalyst (c) and temperature (d) (Inset: Plot of absorbance vs wavelength at different time interval) for complex C8 with 4-MC

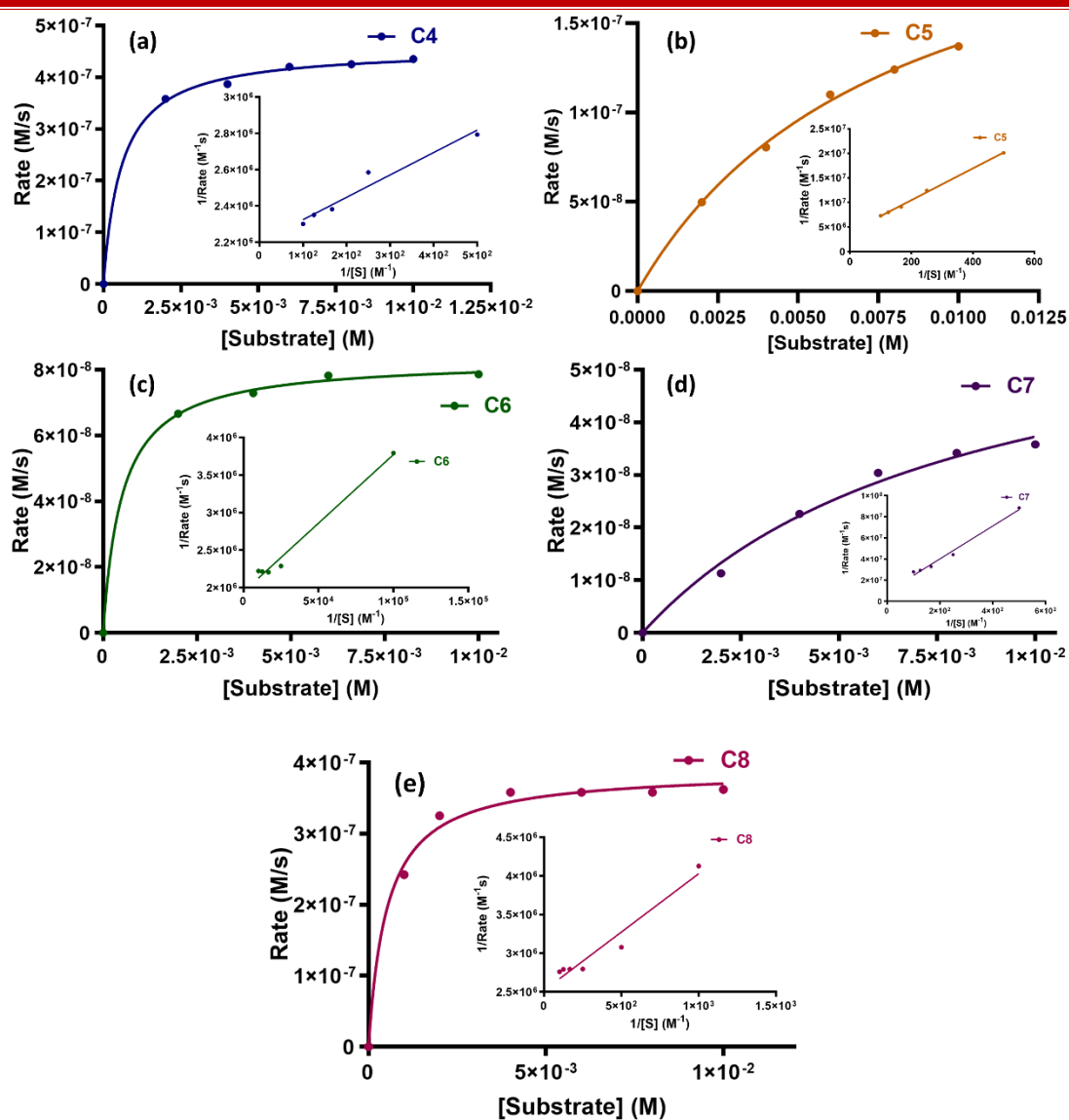


Fig. S3.21 Plot of Rate vs [Substrate] of Michaelis Menten model for complexes (a) C4 (b) C5 (c) C6 (d) C7 and (e) C8 (Inset: Lineweaver Burk plot) for 4-MC

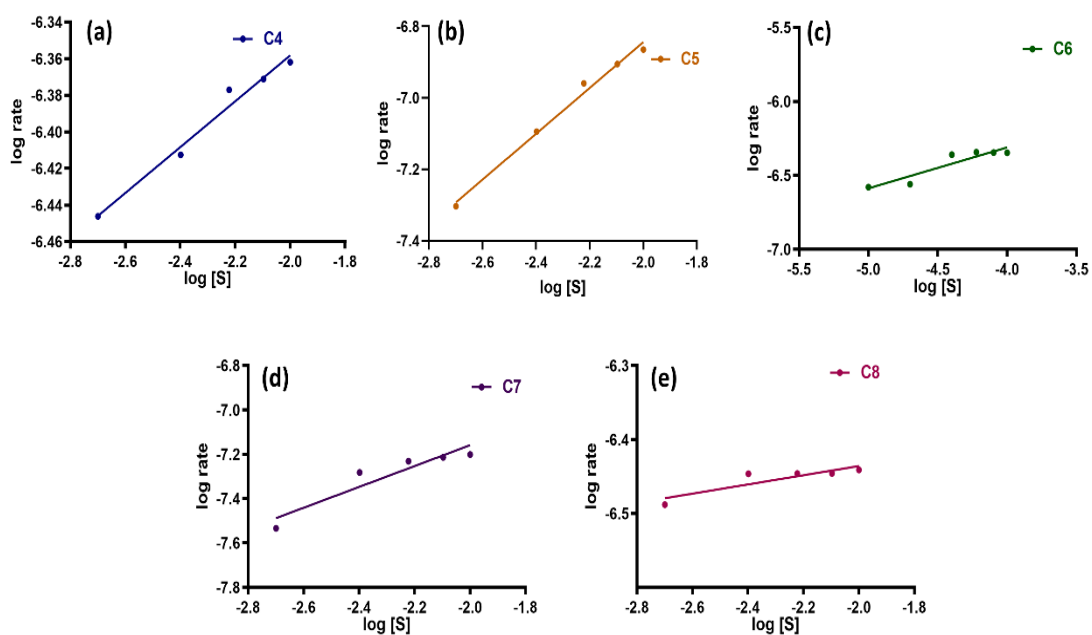


Fig. S3.22 Plot of log rate vs log [Sub] for complexes (a) C4 (b) C5 (c) C6 (d) C7 and (e) C8 for 4-MC

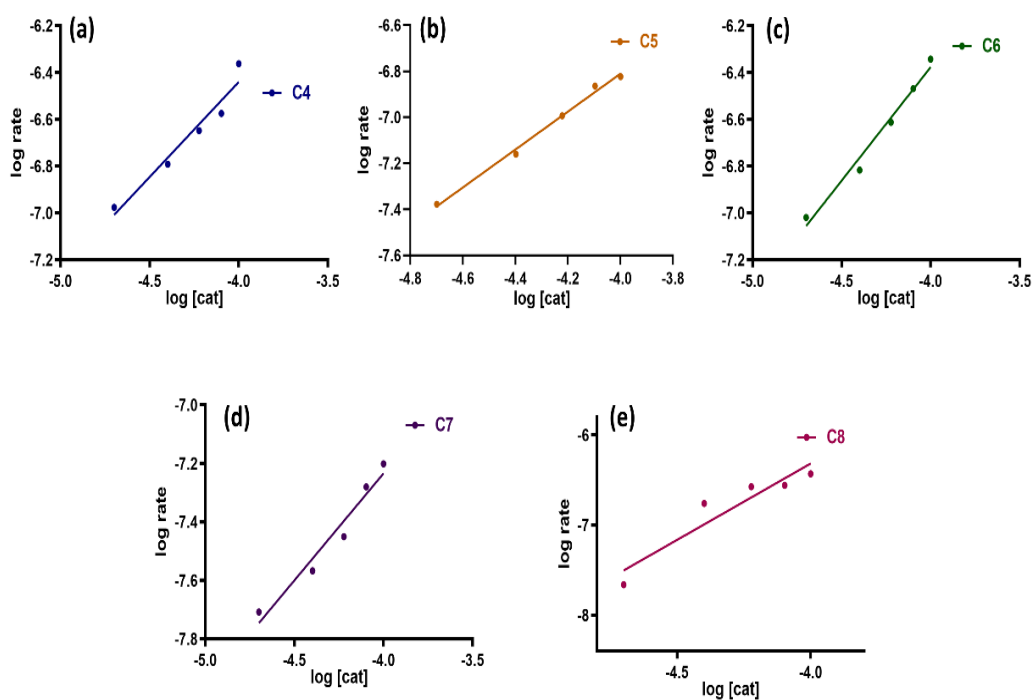


Fig. S3.23 Plot of log rate vs log [Cat] for complexes (a) C4 (b) C5 (c) C6 (d) C7 and (e) C8 for 4-MC

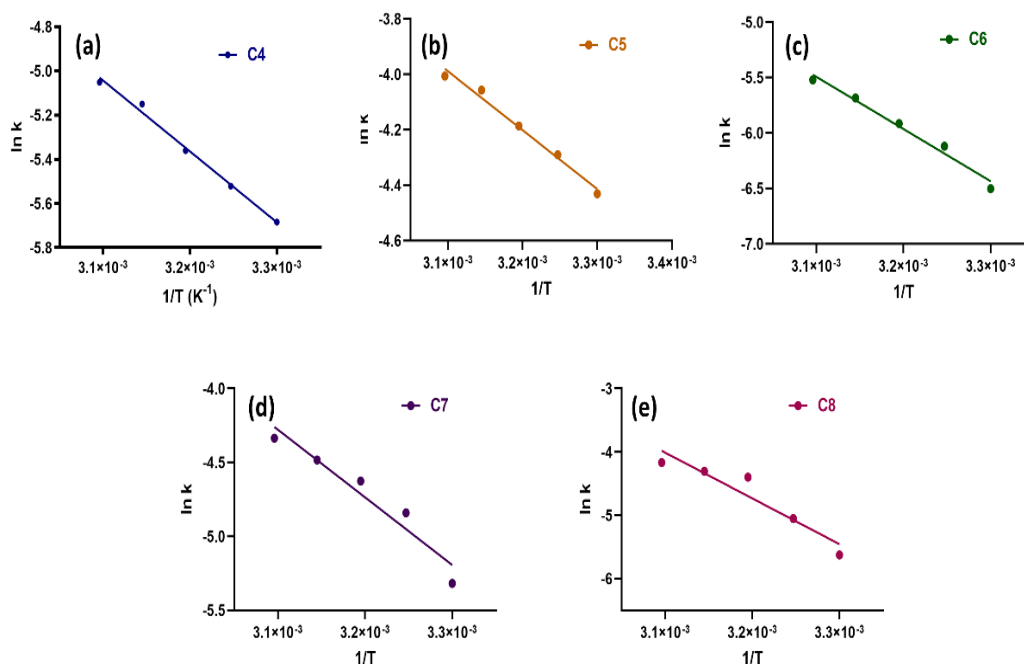


Fig. S3.24 Arrhenius plot of all complexes (a) C4 (b) C5 (c) C6 (d) C7 and (e) C8 for 4-MC

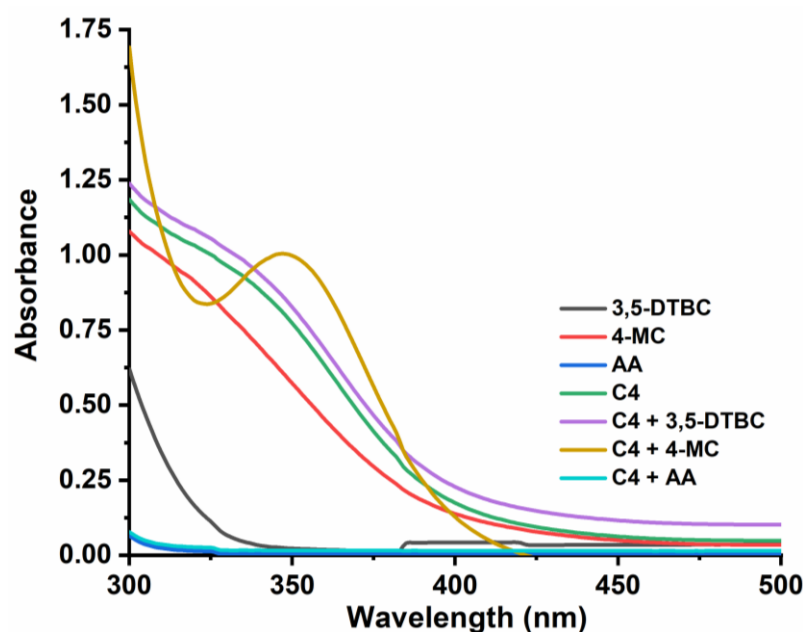


Fig. S3.25 Electronic spectra of the formation of I_3^- ion in the presence of H_2O_2 (detection was achieved as mentioned in the text).

Similarly, detection of hydrogen peroxide was spectroscopically monitored for complex C5, C6, C7, and C8 for 3,5-BTBC and 4-MC, there was no absorption band due to I_3^- was observed in 3,5-DTBC while there was absorption band at 353nm due to I_3^- in case of 4-MC. This confirms that hydrogen peroxide was formed during the catalytic reaction only 4-MC was used as substrate in the catalytic reactions.

References

1. Gerdemann, C., Eicken, C. & Krebs, B. The crystal structure of catechol oxidase: New insight into the function of type-3 copper proteins. *Acc. Chem. Res.* **35**, 183–191 (2002).
2. Majumder, I., Chakraborty, P., Adhikary, J., Kara, H., Zangrando, E., Bauza, A., Frontera, A. & Das, D. Auxiliary Part of Ligand Mediated Unique Coordination Chemistry of Copper (II). *ChemistrySelect* **1**, 615–625 (2016).
3. Braunstein, P. & Naud, F. Hemilability of Hybrid Ligands and the Coordination Chemistry of Oxazoline-Based Systems. *Angew. Chemie Int. Ed.* **40**, 680–699 (2001).
4. Mukherjee, R. Coordination chemistry with pyrazole-based chelating ligands: molecular structural aspects. *Coord. Chem. Rev.* **203**, 151–218 (2000).
5. Dorta, R., Stevens, E. D., Scott, N. M., Costabile, C., Cavallo, L., Hoff, C. D. & Nolan, S. P. Steric and Electronic Properties of N-Heterocyclic Carbenes (NHC): A Detailed Study on Their Interaction with Ni(CO)₄. *J. Am. Chem. Soc.* **127**, 2485–2495 (2005).
6. Benkstein, K. D., Hupp, J. T. & Stern, C. L. Molecular Rectangles Based on Rhenium(I) Coordination Chemistry. *J. Am. Chem. Soc.* **120**, 12982–12983 (1998).
7. Dey, S. K. & Mukherjee, A. Catechol oxidase and phenoxazinone synthase: Biomimetic functional models and mechanistic studies. *Coord. Chem. Rev.* **310**, 80–115 (2016).
8. Solomon, E. I., Sundaram, U. M. & Machonkin, T. E. Multicopper oxidases and oxygenases. *Chem. Rev.* **96**, 2563–2605 (1996).
9. Solomon, E. I., Sarangi, R., Woertink, J. S., Augustine, A. J., Yoon, J. & Ghosh, S. O₂ and M₂O activation by bi-, tri-, and tetranuclear Cu clusters in biology. *Acc. Chem. Res.* **40**, 581–591 (2007).
10. Gerdemann, C., Eicken, C., Galla, H.-J. & Krebs, B. Comparative modeling of the latent form of a plant catechol oxidase using a molluscan hemocyanin structure. *J. Inorg. Biochem.* **89**, 155–158 (2002).
11. Rompel, A., Fischer, H., Meiwes, D., Büldt-Karentzopoulos, K., Magrini, A., Eicken, C., Gerdemann, C. & Krebs, B. Substrate specificity of catechol oxidase from *Lycopus europaeus* and characterization of the bioproducts of enzymic caffeic acid oxidation. *FEBS Lett.* **445**, 103–110 (1999).
12. Rompel, A., Fischer, H., Büldt-karentzopoulos, K., Meiwes, D. & Zippel, F. Spectroscopic and EXAFS studies on Catechol Oxidases with dinuclear copper centers of type 3: Evidence for μ - η^2 : η^2 -peroxo-intermediates during the reaction with catechol. *J. Inorg. Biochem.* **59**, 715 (1995).
13. Anekwe, J., Hammerschmidt, A., Rompel, A. & Krebs, B. Altering the activity of catechol oxidase model compounds by electronic influence on the copper core. *Zeitschrift für Anorg. und Allg. Chemie* **632**, 1057–1066 (2006).
14. Gentshev, P., Lüken, M., Möller, N., Rompel, A. & Krebs, B. Synthesis of a novel μ -acetate bridged dinuclear Cu(II) complex as model compound for the active site of tyrosinase: Crystal structure, magnetic properties and catecholase activity. *Inorg. Chem. Commun.* **4**, 753–756 (2001).
15. Merkel, M., Möller, N., Piacenza, M., Grimme, S., Rompel, A. & Krebs, B. Less symmetrical dicopper(II) complexes as catechol oxidase models - An adjacent thioether group increases catecholase activity. *Chem. - A Eur. J.* **11**, 1201–1209 (2005).
16. Klabunde, T., Eicken, C., Sacchettini, J. C., Krebs, B., Henson, M. J. & Solomon, E. I. Crystal structure of a plant catechol oxidase containing a dicopper center. *Nat. Struct. Biol.* **5**, 1084–1090 (1998).
17. Than, R., Feldmann, A. A. & Krebs, B. Structural and functional studies on model compounds of purple acid phosphatases and catechol oxidases. *Coord. Chem. Rev.* **182**, 211–241 (1999).
18. Kovala-Demertzi, D., Galani, A., Demertzis, M. A., Skoulika, S. & Kotoglou, C. Binuclear copper(II) complexes of tolfenamic: Synthesis, crystal structure, spectroscopy and superoxide dismutase activity. *J. Inorg. Biochem.* **98**, 358–364 (2004).
19. Koval, I. A., Gamez, P., Belle, C., Selmeçzi, K. & Reedijk, J. Synthetic models of the

- active site of catechol oxidase: Mechanistic studies. *Chem. Soc. Rev.* **35**, 814–840 (2006).
20. Koval, I. A., Belle, C., Selmeçzi, K., Philouze, C., Saint-Aman, E., Schuitema, A. M., Gamez, P., Pierre, J.-L. & Reedijk, J. Catecholase activity of a μ -hydroxodicopper(II) macrocyclic complex: structures, intermediates and reaction mechanism. *JBIC J. Biol. Inorg. Chem.* **10**, 739–750 (2005).
 21. Yang, C. T., Vetrichelvan, M., Yang, X., Moubaraki, B., Murray, K. S. & Vittal, J. J. Syntheses, structural properties and catecholase activity of copper(II) complexes with reduced Schiff base N-(2-hydroxybenzyl)-amino acids. *J. Chem. Soc. Dalt. Trans.* **4**, 113–121 (2004).
 22. Chakraborty, P., Adhikary, J., Ghosh, B., Sanyal, R., Chattopadhyay, S. K., Bauzá, A., Frontera, A., Zangrando, E. & Das, D. Relation between the Catalytic Efficiency of the Synthetic Analogues of Catechol Oxidase with Their Electrochemical Property in the Free State and Substrate-Bound State. *Inorg. Chem.* **53**, 8257–8269 (2014).
 23. Belle, C., Beguin, C., Gautier-Luneau, I., Hamman, S., Philouze, C., Pierre, J. L., Thomas, F., Torelli, S., Saint-Aman, E. & Bonin, M. Dicopper(II) complexes of H-BPMP-type ligands: Ph-induced changes of redox, spectroscopic (^{19}F NMR studies of fluorinated complexes), structural properties, and catecholase activities. *Inorg. Chem.* **41**, 479–491 (2002).
 24. Sanyal, R., Ketkov, S., Purkait, S., Mautner, F. A., Zhigulin, G. & Das, D. Nuclearity dependent solvent contribution to the catechol oxidase activity of novel copper(II) complexes derived from Mannich-base ligand platforms: synthesis, crystal structure and mechanism. *New J. Chem.* **41**, 8586–8597 (2017).
 25. Anitha, N., Saravanan, N., Ajaykamil, T., Suresh, E. & Palaniandavar, M. Catecholase activity of mononuclear copper(II) complexes of tridentate 3N ligands in aqueous and aqueous micellar media: Influence of stereoelectronic factors on catalytic activity. *Inorganica Chim. Acta* **485**, 98–111 (2019).
 26. Adhikary, J., Majumdar, I., Kundu, P., Kornweitz, H., Kara, H. & Das, D. Role of Electronegative Atom Present on Ligand Backbone and Substrate Binding Mode on Catecholase- and Phosphatase-Like Activities of Dinuclear Ni(II) Complexes: A Theoretical Support. *ChemistrySelect* **3**, 1445–1454 (2018).
 27. Mondal, S., Chakraborty, M., Mondal, A., Pakhira, B., Blake, A. J., Sinn, E. & Chattopadhyay, S. K. Cu(II) complexes of a tridentate N,N,O-donor Schiff base of pyridoxal: synthesis, X-ray structures, DNA-binding properties and catecholase activity. *New J. Chem.* **42**, 9588–9597 (2018).
 28. Mandal, A., Dasgupta, S., Ganguly, S., Bauzá, A., Frontera, A. & Das, D. Cooperative influence of pseudohalides and ligand backbone of Schiff-bases on nuclearity and stereochemistry of cobalt(III) complexes: experimental and theoretical investigation. *Dalt. Trans.* **46**, 15257–15268 (2017).
 29. Sengupta, S., Naath Mongal, B., Das, S., Panda, T. K., Mandal, T. K., Fleck, M., Chattopadhyay, S. K. & Naskar, S. Mn(III) and Cu(II) complexes of 1-((3-(dimethylamino)propylimino)methyl) naphthalen-2-ol): Synthesis, characterization, catecholase and phenoxazinone synthase activity and DFT-TDDFT study. *J. Coord. Chem.* **71**, 1214–1233 (2018).
 30. Mandal, S., Mukherjee, J., Lloret, F. & Mukherjee, R. Modeling tyrosinase and catecholase activity using new m-xylyl-based ligands with bidentate alkylamine terminal coordination. *Inorg. Chem.* **51**, 13148–13161 (2012).
 31. Parua, S. P., Sinha, D. & Rajak, K. K. A Highly Selective “On-Off-On” Optical Switch for Sequential Detection of Cu^{2+} and S^{2-} Ions Based on 2, 6-Diformyl-4-methyl Phenol and Catecholase Activity by Its Copper Complex. *ChemistrySelect* **3**, 1120–1128 (2018).
 32. Majumder, I., Chakraborty, P., Álvarez, R., Gonzalez-Diaz, M., Peláez, R., Ellahioui, Y., Bauza, A., Frontera, A., Zangrando, E., Gómez-Ruiz, S. & Das, D. Bioactive Heterometallic Cu(II)–Zn(II) Complexes with Potential Biomedical Applications. *ACS Omega* **3**, 13343–13353 (2018).

33. Das, M., Kumar Kundu, B., Tiwari, R., Mandal, P., Nayak, D., Ganguly, R. & Mukhopadhyay, S. Investigation on chemical protease, nuclease and catecholase activity of two copper complexes with flexidentate Schiff base ligands. *Inorganica Chim. Acta* **469**, 111–122 (2018).
34. Mitra, M., Maji, A. K., Ghosh, B. K., Kaur, G., Choudhury, A. R., Lin, C. H., Ribas, J. & Ghosh, R. Synthesis, crystallographic characterization and catecholase activity of a monocopper(II) and a dimanganese(III) complex with an anionic Schiff base ligand. *Polyhedron* **61**, 15–19 (2013).
35. Dutta, S., Mayans, J. & Ghosh, A. Facile synthesis of a new Cu(II) complex with an unsymmetrical ligand and its use as an O₃ donor metalloligand in the synthesis of Cu(II)-Mn(II) complexes: Structures, magnetic properties, and catalytic oxidase activities. *Dalt. Trans.* **49**, 1276–1291 (2020).
36. Dutta, S., Mayans, J. & Ghosh, A. Facile synthesis of a new Cu(II) complex with an unsymmetrical ligand and its use as an O₃ donor metalloligand in the synthesis of Cu(II)-Mn(II) complexes: structures, magnetic properties, and catalytic o. *Dalt. Trans.* **49**, 1276–1291 (2020).
37. Biswas, A., Das, L. K., Drew, M. G. B., Diaz, C. & Ghosh, A. Insertion of a hydroxido bridge into a diphenoxido dinuclear copper(II) complex: Drastic change of the magnetic property from strong antiferromagnetic to ferromagnetic and enhancement in the catecholase activity. *Inorg. Chem.* **51**, 10111–10121 (2012).
38. Chatterjee, A., Yadav, H. R., Choudhury, A. R., Ali, A., Singh, Y. & Ghosh, R. Tyrosinase and catecholase-like activities of a dinuclear Cu(II) complex. *Polyhedron* **141**, 140–146 (2018).
39. Biswas, A., Das, L. K. & Ghosh, A. Solvomorphism and catecholase activities of bis(μ -phenoxido) dicopper(II) complexes. *Polyhedron* **61**, 253–261 (2013).
40. Ghosh, D., Lal, T. K. & Mukherjee, R. Dicopper complexes of relevance to tyrosinase modelling: An overview. *Proc. Indian Acad. Sci. Chem. Sci.* **108**, 251–256 (1996).
41. Kitajima, N. & Moro-oka, Y. Copper-Dioxygen Complexes. Inorganic and Bioinorganic Perspectives. *Chem. Rev.* **94**, 737–757 (1994).
42. Kitajima, N. Synthesis, Structure and Properties of μ - η^2 : η^2 Peroxo Dinuclear Copper Complexes Modeling the Active Site of Oxyhemocyanin and Oxytyrosinase. *Bioinorg. Chem. Copp.* **1**, 251–263 (1993).
43. Kitajima, N., Fujisawa, K., Hikichi, S. & Morooka, Y. Formation of (μ -hydroxo)(μ -azido) dinuclear copper complex from μ - η^2 : η^2 -peroxo complex. *J. Am. Chem. Soc.* **115**, 7874–7875 (1993).
44. Kitajima, N., Koda, T., Hashimoto, S., Kitagawa, T. & Morooka, Y. Synthesis and characterization of the dinuclear copper(II) complexes [Cu(HB(3,5-Me₂pz)₃]₂X (X = O₂⁻, (OH)₂²⁻, CO₂²⁻, O₂²⁻). *J. Am. Chem. Soc.* **113**, 5664–5671 (1991).
45. Patel, R. N. Synthesis, characterization and superoxide dismutase activity of some four coordinated copper(ii) complexes. *Indian J. Chem. - Sect. A Inorganic, Phys. Theor. Anal. Chem.* **48**, 1370–1377 (2009).
46. Patel, R. N., Singh, N., Shukla, K. K. & Gundla, V. L. N. E.S.R., magnetic, electronic and superoxide dismutase studies of imidazolate-bridged Cu(II)-Cu(II) complexes with ethylenediamine as capping ligand. *Spectrochim. Acta - Part A Mol. Biomol. Spectrosc.* **61**, 1893–1897 (2005).
47. Jakab, N. I., Jancsó, A., Gajda, T., Gyurcsik, B. & Rockenbauer, A. Copper(II), nickel(II) and zinc(II) complexes of N-acetyl-His-Pro-His-His-NH₂: Equilibria, solution structure and enzyme mimicking. *J. Inorg. Biochem.* **102**, 1438–1448 (2008).
48. Abuhijleh, A. L. Superoxide Dismutase and Oxidase Activities of Copper (II) Complexes of the Anti-inflammatory Drug Ibuprofen with Imidazoles and Pyrazole. 2–3 (2002).
49. Latif Abuhijleh, A. & Woods, C. Synthesis, crystal structure and superoxide dismutase mimetic activity of hexakis (N-methylimidazole) copper(II) salicylate. *Inorg. Chem. Commun.* **5**, 269–273 (2002).
50. Abuhijleh, A. L. Mononuclear copper (II) salicylate complexes with 1,2-

- dimethylimidazole and 2-methylimidazole: Synthesis, spectroscopic and crystal structure characterization and their superoxide scavenging activities. *J. Mol. Struct.* **980**, 201–207 (2010).
51. Pierre, J. L., Chautemps, P., Refaif, S., Beguin, C., Marzouki, A. El, Serratrice, G., Saint-Aman, E. & Rey, P. Imidazolate-Bridged Dicopper(II) and Copper–Zinc Complexes of a Macrobicyclic Ligand (Cryptand). A Possible Model for the Chemistry of Cu–Zn Superoxide Dismutase. *J. Am. Chem. Soc.* **117**, 1965–1973 (1995).
 52. Aston, K., Rath, N., Naik, A., Slomczynska, U., Schall, O. F. & Riley, D. P. Computer-aided design (CAD) of Mn(II) complexes: Superoxide dismutase mimetics with catalytic activity exceeding the native enzyme. *Inorg. Chem.* **40**, 1779–1789 (2001).
 53. Štarha, P., Trávníček, Z., Herchel, R., Popa, I., Suchý, P. & Vančo, J. Dinuclear copper(II) complexes containing 6-(benzylamino)purines as bridging ligands: Synthesis, characterization, and in vitro and in vivo antioxidant activities. *J. Inorg. Biochem.* **103**, 432–440 (2009).
 54. Balasubramanian, V., Ezhevskaya, M., Moons, H., Markus Neuburger, Carol Cristescu, S. V. D. & Cornelia, P. Structural characterization of a highly active superoxide-dismutase mimic. *Phys. Chem. Chem. Phys.* **11**, 6778–6787 (2009).
 55. Zhang, D. L., Busch, D. H., Lennon, P. L., Weiss, R. H., Neumann, W. L. & Riley, D. P. Iron(III) Complexes as Superoxide Dismutase Mimics: Synthesis, Characterization, Crystal Structure, and Superoxide Dismutase (SOD) Activity of Iron(III) Complexes Containing Pentaaza Macrocyclic Ligands. *Inorg. Chem.* **37**, 956–963 (1998).
 56. Banci, L., Bertini, I., Chiu, C. Y., Mullenbach, G. T. & Viezzoli, M. S. Synthesis and Characterization of a Monomeric Mutant Cu/Zn Superoxide Dismutase with Partially Reconstituted Enzymic Activity. *Eur. J. Biochem.* **234**, 855–860 (1995).
 57. Patel, R. N., Shukla, K. K., Singh, A., Choudhary, M., Patel, D. K., Niclos-Gutierrez, J. & Choquesillo-Lazarte, D. Spectral, structural, and superoxide dismutase activity of some octahedral nickel(II) complexes with tri-tetradentate ligands. *J. Coord. Chem.* **63**, 3648–3661 (2010).
 58. Ramadan, A. E. M. M., El-Mehasseb, I. M. & Issa, R. M. Synthesis, characterization and superoxide dismutase mimetic activity of ruthenium(III) oxime complexes. *Transit. Met. Chem.* **22**, 529–534 (1997).
 59. Ramadan, A. M. & El-Naggar, M. M. Synthesis, characterization and demonstration of superoxide dismutase-like activity of copper(II) chloride, bromide, nitrate, thiocyanate, sulphate, and perchlorate complexes with 2-methyl-amino pyridine. *J. Inorg. Biochem.* **63**, 143–153 (1996).
 60. Ramadan, A. M. Structural and biological aspects of copper (II) complexes with 2-methyl-3-amino-(3H)-quinazolin-4-one. *J. Inorg. Biochem.* **65**, 183–189 (1997).
 61. Biswas, P. P., Bhattacharyya, P. K. & Das, D. K. Synthesis, characterization, DFT / TDDFT calculation and superoxide dismutase activity of copper (II) complex with ligand derived from benzil and cysteine. *J. Chem. Pharm. Res.* **7**, 102–108 (2015).
 62. Patel, M. N., Gandhi, D. S. & Parmar, P. A. SOD mimic activity, DNA binding and in-vitro antibacterial studies of drug based copper(II) complexes. *Inorg. Chem. Commun.* **13**, 618–621 (2010).
 63. Patel, R. N., Singh, N., Gundla, V. L. N. & Chauhan, U. K. Copper(II) complexes of tridentate N,N,N',N'',N''-pentamethyldiethylenetriamine: Superoxide dismutase and inhibitory activity against bacteria and fungi. *Spectrochim. Acta - Part A Mol. Biomol. Spectrosc.* **66**, 726–731 (2007).
 64. Patel, R. N., Singh, A., Shukla, K. K., Patel, D. K. & Sondhiya, V. P. Synthesis, characterization, and superoxide dismutase activity of copper(II) complexes with bidentate ligands. *J. Coord. Chem.* **63**, 3483–3497 (2010).
 65. Patel, R. N., Shukla, K. K., Singh, A., Choudhary, M., Chauhan, U. K. & Dwivedi, S. Copper(II) complexes as superoxide dismutase mimics: Synthesis, characterization, crystal structure and bioactivity of copper(II) complexes. *Inorganica Chim. Acta* **362**, 4891–4898 (2009).
 66. Patel, R. N., Singh, A., Shukla, K. K., Patel, D. K. & Sondhiya, V. P. Copper(II)

- complexes with N-(2-hydroxyethyl)-2-iminodiacetic acid and imidazoles: Crystal structure, spectroscopic studies and superoxide dismutase activity. *Transit. Met. Chem.* **35**, 577–584 (2010).
67. Patel, R. N., Shukla, K. K., Singh, A., Choudhary, M. & Patel, D. K. Synthesis, characterization, crystal structures, and superoxide dismutase activity of copper(II) octahedral complexes containing tri- and monodentate ligands. *J. Coord. Chem.* **63**, 586–599 (2010).
68. Patel, M. N., Bhatt, B. S. & Dosi, P. A. Study of SOD mimic and nucleic acid interaction activity exerted by enrofloxacin-based copper(II) complexes. *Chem. Biodivers.* **9**, 2810–2824 (2012).
69. Patel, M. N., Patel, C. R. & Joshi, H. N. Metal-based biologically active compounds: Synthesis, characterization, DNA interaction, antibacterial, cytotoxic and SOD mimic activities. *Appl. Biochem. Biotechnol.* **169**, 1329–1345 (2013).
70. Devereux, M., O'Shea, D., O'Connor, M., Grehan, H., Connor, G., McCann, M., Rosair, G., Lyng, F., Kellett, A., Walsh, M., Egan, D. & Thati, B. Synthesis, catalase, superoxide dismutase and antitumour activities of copper(II) carboxylate complexes incorporating benzimidazole, 1,10-phenanthroline and bipyridine ligands: ... *Polyhedron* **26**, 4073–4084 (2007).
71. Devereux, M., O'Shea, D., Kellett, A., McCann, M., Walsh, M., Egan, D., Deegan, C., Kedziora, K., Rosair, G. & Müller-Bunz, H. Synthesis, X-ray crystal structures and biomimetic and anticancer activities of novel copper(II)benzoate complexes incorporating 2-(4'-thiazolyl)benzimidazole (thiabenzazole), 2-(2-pyridyl)benzimidazole and 1,10-phenanthroline as chelating nitrogen donor. *J. Inorg. Biochem.* **101**, 881–892 (2007).
72. O'Connor, M., Kellett, A., McCann, M., Rosair, G., McNamara, M., Howe, O., Creaven, B. S., McClean, S., Foltyn-Arfa Kia, A., O'Shea, D. & Devereux, M. Copper(II) complexes of salicylic acid combining superoxide dismutase mimetic properties with DNA binding and cleaving capabilities display promising chemotherapeutic potential with fast acting in vitro cytotoxicity against cisplatin sensitive and resistant. *J. Med. Chem.* **55**, 1957–1968 (2012).
73. Potapov, A. S., Nudnova, E. A., Domina, G. A., Kirpotina, L. N., Quinn, M. T., Khlebnikov, A. I. & Schepetkin, I. A. Synthesis, characterization and potent superoxide dismutase-like activity of novel bis(pyrazole)-2,2'-bipyridyl mixed ligand copper(II) complexes. *Dalt. Trans.* 4488–4498 (2009).
74. Mandal, S. K. & Nag, K. Dinuclear Metal Complexes. Part 2. Synthesis, Characterisation, and Electrochemical Studies. **3**, (1983).
75. Dolomanov, O. V., Bourhis, L. J., Gildea, R. J., Howard, J. A. K. & Puschmann, H. OLEX2: A complete structure solution, refinement and analysis program. *J. Appl. Crystallogr.* **42**, 339–341 (2009).
76. Sheldrick, G. M. A short history of SHELX. *Acta Crystallogr. Sect. A Found. Crystallogr.* **64**, 112–122 (2008).
77. Sheldrick, G. M. Crystal structure refinement with SHELXL. *Acta Crystallogr. Sect. C* **71**, 3–8 (2015).
78. Frisch, M. J., Trucks, G. W., Schlegel, H. B., Scuseria, G. E., Robb, M. A., Cheeseman, J. R., Scalmani, G., Barone, V., Petersson, G. A., Nakatsuji, H., Li, X., Caricato, M., Marenich, A. V., Bloino, J., Janesko, B. G., Gomperts, R., Mennucci, B., Hratchian, H. P., Ortiz, J. V. *et al.* Gaussian 16, Revision A.03. *Gaussian, Inc., Wallingford CT* (2016).
79. Stephens, P. J., Devlin, F. J., Chabalowski, C. F. & Frisch, M. J. Ab Initio Calculation of Vibrational Absorption and Circular Dichroism Spectra Using Density Functional Force Fields. *J. Phys. Chem.* **98**, 11623–11627 (1994).
80. Hay, P. J. & Wadt, W. R. Ab initio effective core potentials for molecular calculations. Potentials for K to Au including the outermost core orbitals. *J. Chem. Phys.* **82**, 299–310 (1985).
81. Wadt, W. R. & Hay, P. J. Ab initio effective core potentials for molecular calculations. Potentials for main group elements Na to Bi. *J. Chem. Phys.* **82**, 284–298 (1985).

82. Dennington, R., Keith, T. A. & Millam, J. M. GaussView, Version 6. at (2016).
83. Lever, A. B. P. (Alfred B. P. *Inorganic electronic spectroscopy*, Elsevier, New York. (Elsevier Pub. Co, 1968).
84. Shoba, D., Periandy, S., Karabacak, M. & Ramalingam, S. Vibrational spectroscopy (FT-IR and FT-Raman) investigation, and hybrid computational (HF and DFT) analysis on the structure of 2,3-naphthalenediol. *Spectrochim. Acta Part A Mol. Biomol. Spectrosc.* **83**, 540–552 (2011).
85. Fukui, K. Role of Frontier Orbitals in Chemical Reactions. *Science (80-.)*. **218**, 747–754 (1982).
86. Wang, Q., Chen, D., Liu, X. & Zhang, L. Theoretical mechanisms of the superoxide radical anion catalyzed by the nickel superoxide dismutase. *Comput. Theor. Chem.* **966**, 357–363 (2011).
87. Jawaria, R., Hussain, M., Khalid, M., Khan, M. U., Tahir, M. N., Naseer, M. M., Braga, A. A. C. & Shafiq, Z. Synthesis, crystal structure analysis, spectral characterization and nonlinear optical exploration of potent thiosemicarbazones based compounds: A DFT refine experimental study. *Inorganica Chim. Acta* **486**, 162–171 (2019).
88. Koopmans, T. Über die Zuordnung von Wellenfunktionen und Eigenwerten zu den Einzelnen Elektronen Eines Atoms. *Physica* **1**, 104–113 (1934).
89. Patel, R. N., Singh, N. & Gundla, V. L. N. Synthesis, characterization and superoxide dismutase activity of some octahedral nickel(II) complexes. *Polyhedron* **26**, 757–762 (2007).
90. He, S.-B., Hu, A.-L., Zhuang, Q.-Q., Peng, H.-P., Deng, H.-H., Chen, W. & Hong, G.-L. Ascorbate Oxidase Mimetic Activity of Copper(II) Oxide Nanoparticles. *ChemBioChem* **21**, 978–984 (2020).
91. Monzani, E., Battaini, G., Perotti, A., Casella, L., Gullotti, M., Santagostini, L., Nardin, G., Randaccio, L., Geremia, S., Zanello, P. & Opromolla, G. Mechanistic, structural, and spectroscopic studies on the catecholase activity of a dinuclear copper complex by dioxygen. *Inorg. Chem.* **38**, 5359–5369 (1999).
92. Monzani, E., Quinti, L., Perotti, A., Casella, L., Gullotti, M., Randaccio, L., Geremia, S., Nardin, G., Faleschini, P. & Tabbì, G. Tyrosinase models. Synthesis, structure, catechol oxidase activity, and phenol monooxygenase activity of a dinuclear copper complex derived from a triamino pentabenzimidazole ligand. *Inorg. Chem.* **37**, 553–562 (1998).
93. Ackermann, J., Meyer, F., Kaifer, E. & Pritzkow, H. Tuning the Activity of Catechol Oxidase Model Complexes by Geometric Changes of the Dicopper Core. *Chem. – A Eur. J.* **8**, 247–258 (2002).

